AGU PUBLICATIONS

JGR

Journal of Geophysical Research: Solid Earth

RESEARCH ARTICLE

10.1002/2015JB012628

Key Points:
- X-ray computed tomography was used to quantitatively describe 3-D spinel shape fabric
- Relationship between finite strain geometry and olivine texture is established for the first time in naturally deformed mantle rocks
- Axial-[010] and axial-[100] olivine crystallographic preferred orientations form by flattening and constrictional strain, respectively

Supporting Information:
- Supporting Information S1
- Table S4
- Movie S1

Correspondence to:
V. Chatzaras,
chatzaras@wisc.edu

Citation:
Chatzaras, V., S. C. Kruckenberg, S. M. Cohen, L. G. Medaris Jr., A. C. Withers, and B. Bagley (2016), Axial-type olivine crystallographic preferred orientations: The effect of strain geometry on mantle texture, *J. Geophys. Res. Solid Earth*, *121*, doi:10.1002/2015JB012628.

Received 31 OCT 2015
Accepted 16 JUN 2016
Accepted article online 19 JUN 2016

Axial-type olivine crystallographic preferred orientations: The effect of strain geometry on mantle texture

Vasileios Chatzaras[1,2,3], Seth C. Kruckenberg[1], Shaina M. Cohen[1], L. Gordon Medaris Jr.[4], Anthony C. Withers[5], and Brian Bagley[6]

[1]Department of Earth and Environmental Sciences, Boston College, Chestnut Hill, Massachusetts, USA, [2]Now at Department of Geoscience, University of Wisconsin-Madison, Madison, Wisconsin, USA, [3]Now at Department of Earth Sciences, Utrecht University, Utrecht, Netherlands, [4]Department of Geoscience, University of Wisconsin-Madison, Madison, Wisconsin, USA, [5]Department of Earth Sciences and Centre for Planetary Science and Exploration, University of Western Ontario, London, Ontario, Canada, [6]Department of Earth Sciences, University of Minnesota, Twin Cities, Minneapolis, Minnesota, USA

Abstract The effect of finite strain geometry on crystallographic preferred orientation (CPO) is poorly constrained in the upper mantle. Specifically, the relationship between shape preferred orientation (SPO) and CPO in mantle rocks remains unclear. We analyzed a suite of 40 spinel peridotite xenoliths from Marie Byrd Land, West Antarctica. X-ray computed tomography allows for quantification of spinel SPO, which ranges from prolate to oblate shape. Electron backscatter diffraction analysis reveals a range of olivine CPO patterns, including A-type, axial-[010], axial-[100], and B-type patterns. Until now, these CPO types were associated with different deformation conditions, deformation mechanisms, or strain magnitudes. Microstructures and deformation mechanism maps suggest that deformation in all studied xenoliths is dominated by dislocation-accommodated grain boundary sliding. For the range of temperatures (780–1200°C), extraction depths (39–72 km), differential stresses (2–60 MPa), and water content (up to 500 H/10^6Si) of the xenolith suite, variations in olivine CPO do not correlate with changes in deformation conditions. Here we establish for the first time in naturally deformed mantle rocks that finite strain geometry controls the development of axial-type olivine CPOs; axial-[010] and axial-[100] CPOs form in relation to oblate and prolate fabric ellipsoids, respectively. Girdling of olivine crystal axes results from intracrystalline slip with activation of multiple slip systems and grain boundary sliding. Our results demonstrate that mantle deformation may deviate from simple shear. Olivine texture in field studies and seismic anisotropy in geophysical investigations can provide critical constraints for the 3-D strain in the upper mantle.

1. Introduction

Mantle flow produces olivine crystallographic preferred orientation (CPO), which is the dominant cause of mechanical and seismic anisotropy [*Christensen*, 1984; *Tommasi et al*., 1999; *Karato et al*., 2008]. Deformation experiments have established that olivine CPO pattern depends on the degree of activation of different olivine slip systems [*Durham and Goetze*, 1977; *Bai et al*., 1991], which in turn depends on temperature, pressure, differential stress, and water content (Figure 1a) [*Carter and Avé Lallemant*, 1970; *Jung and Karato*, 2001; *Couvy et al*., 2004; *Katayama et al*., 2004; *Karato et al*., 2008; *Demouchy et al*., 2012; *Raterron et al*., 2012]. Studies of naturally deformed rocks support the results of deformation experiments [*Vauchez et al*., 2005; *Mizukami et al*., 2004; *Lee and Jung*, 2015] and in many cases extrapolate experimental results to nature using olivine CPO to infer deformation conditions [e.g., *Saruwatari et al*., 2001; *Katayama and Korenaga*, 2011].

To add complexity, the presence of melt, deformation history (e.g., existence of inherited CPO and strain partitioning), type of deformation (e.g., pure shear, simple shear, transpression, and transtension), and strain magnitude also affects olivine CPO development and evolution [*Avé Lallemant and Carter*, 1970; *Nicolas et al*., 1973; *McKenzie*, 1979; *Ribe and Yu*, 1991; *Wenk et al*., 1991; *Tommasi et al*., 1999; *Holtzman et al*., 2003; *Webber et al*., 2010; *Boneh and Skemer*, 2014; *Hansen et al*., 2014]. The role of strain on olivine CPO evolution is less well understood compared to the effects of melt or changing deformation conditions.

For crustal minerals (e.g., quartz, calcite, mica, and amphibole), it is well established that the shape of the finite strain ellipsoid (i.e., prolate, oblate, and plane strain) affects CPO [e.g., *Lister and Hobbs*, 1980; *Law et al*., 1984; *Schmid and Casey*, 1986; *Kruckenberg et al*., 2010; *Xypolias et al*., 2010, 2013; *Lloyd et al*., 2011; *Llana-Fúnez and Rutter*, 2014]. In these minerals, flattening strain produces girdles parallel to the foliation, constriction is associated with girdles at high angle to the lineation, and plane strain produces clustered distributions

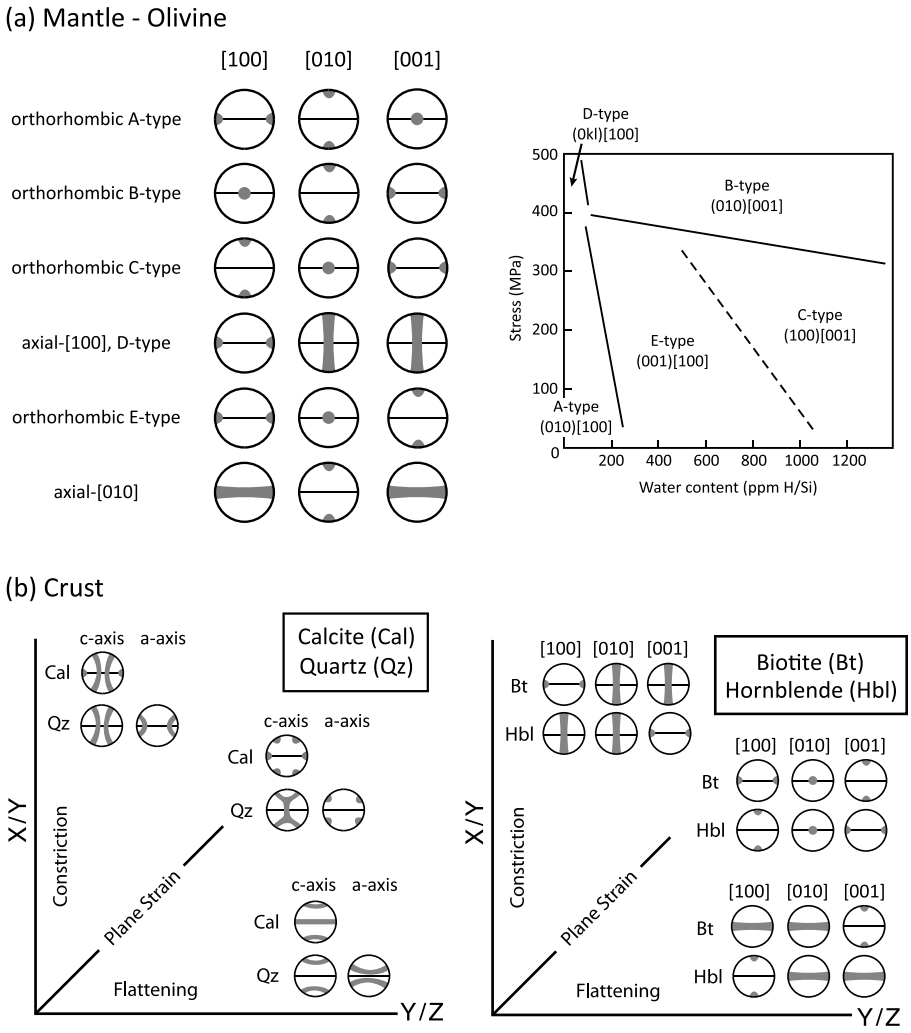

Figure 1. Common interpretation of CPO types in mantle and crust. (a) Schematic depiction of the typical olivine CPO types (left). Equal area, lower hemisphere projections are shown for each of the principal olivine crystallographic axes. Shaded regions denote the dominant crystal axis orientations for each textural type. Olivine CPO type as a function of stress and water content at high temperatures (1200–1300°C) (right). Modified after *Katayama et al*. [2004]. (b) Relationship between finite strain geometry and CPO symmetry for calcite, quartz, biotite, and hornblende. We note that CPO changes as a function of deformation conditions have also been described for crustal minerals (e.g., quartz CPO transitions with temperature). Crystallographic texture data based on calcite [*Llana-Fúnez and Rutter*, 2014], quartz [*Schmid and Casey*, 1986], and biotite and hornblende [*Lloyd et al*., 2011]. Data are shown on Flinn plots.

of crystallographic axes (Figure 1b); an exception is the girdled quartz *c* axis pattern formed in plane strain at low-temperature conditions. A relationship between finite strain geometry and CPO symmetry has also been observed in experimental and numerical simulation studies of olivine deformation [*Avé Lallemant and Carter*, 1970; *Nicolas et al*., 1973; *Wenk et al*., 1991; *Tommasi et al*., 1999; *Miyazaki et al*., 2013]. Yet to the best of our knowledge, such a relationship has not been described for naturally deformed mantle rocks.

Mantle xenoliths transported to the surface by erupted lavas are ideal materials for exploring the relationship between shape preferred orientation (SPO) and CPO under natural deformation conditions. Mantle xenoliths are commonly unaffected by exhumation-related processes (e.g., low-temperature recrystallization and CPO overprinting) that may affect peridotites in exhumed ultramafic massifs. One limitation inherent to xenolith studies is that samples are detached from their original deformation context. When combined with small sample sizes, the identification of mineral SPO (foliation and lineation) is often difficult. The lack of a SPO reference framework in xenolith studies further hampers distinction between olivine CPO patterns that share similar crystal axis symmetry but of variable orientation relative to the orientation of foliation and lineation

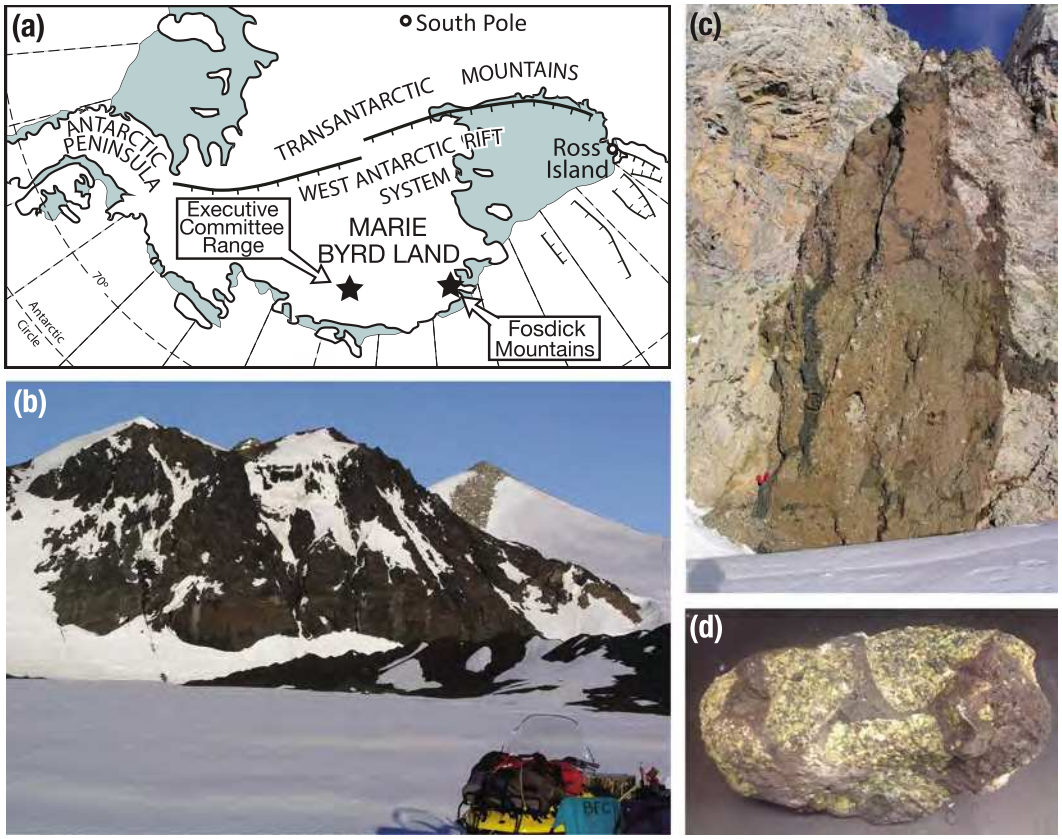

Figure 2. (a) Map of West Antarctica showing the location of the Fosdick Mountains and Executive Committee Range in Marie Byrd Land. (b and c) Field photos of volcanic centers from which the studied mantle xenoliths were sampled. Demas Bluff basalt flow (Figure 2b) and Marujupu diatreme (Figure 2c); note the two people in red parkas for scale in Figure 2c. (d) Example of mantle xenoliths from Demas Bluff basalt flow.

(e.g., orthorhombic A-, B-, C-, and E-type olivine CPO patterns) (Figure 1a). Therefore, our understanding of upper mantle deformation and seismic anisotropy—particularly below continents where exhumed xenoliths are the only source of direct information—is hindered without a methodology that incorporates a quantitative 3-D characterization of SPO, which in turn allows for an unbiased characterization and interpretation of CPO.

In this study, we develop a new approach that allows for evaluation of the relationship between spinel SPO and olivine CPO in mantle materials. Using a combination of X-ray computed tomography and electron backscatter diffraction analysis, we show how limitations inherent to the study of 3-D shape fabric in mantle materials can be overcome to gain new insights into mantle deformation processes and the development of axial-type CPOs in olivine.

2. Geological Setting

The samples analyzed in this study were collected from the Marie Byrd Land volcanic province in West Antarctica (Figure 2a). Marie Byrd Land has experienced a complex deformation history that includes Cretaceous transcurrent to oblique extensional deformation [*Siddoway et al*., 2005; *McFadden et al*., 2010] followed by mid-Cenozoic to present extension and widespread basaltic volcanism [e.g., *Finn et al*., 2005]. West Antarctica is also characterized by slow mantle seismic velocities [e.g., *Sieminski et al*., 2003; *Lloyd et al*., 2015], strong and consistent seismic anisotropy [*Accardo et al*., 2014], and thinned continental crust [*Winberry and Anandakrishnan*, 2004; *Chaput et al*., 2014]; crustal thickness in Marie Byrd Land is approximately 23 km [*Ferraccioli et al*., 2002].

The mantle xenoliths analyzed have been sampled from seven volcanic centers; five centers are located in the Fosdick Mountains (Marujupu Peak, Mount Avers, Demas Bluff, Bird Bluff, and Recess Nunatak), one in the Usas Escarpment (Mount Aldaz) and one in the Executive Committee Range (Mount Cumming) (Figure 2a

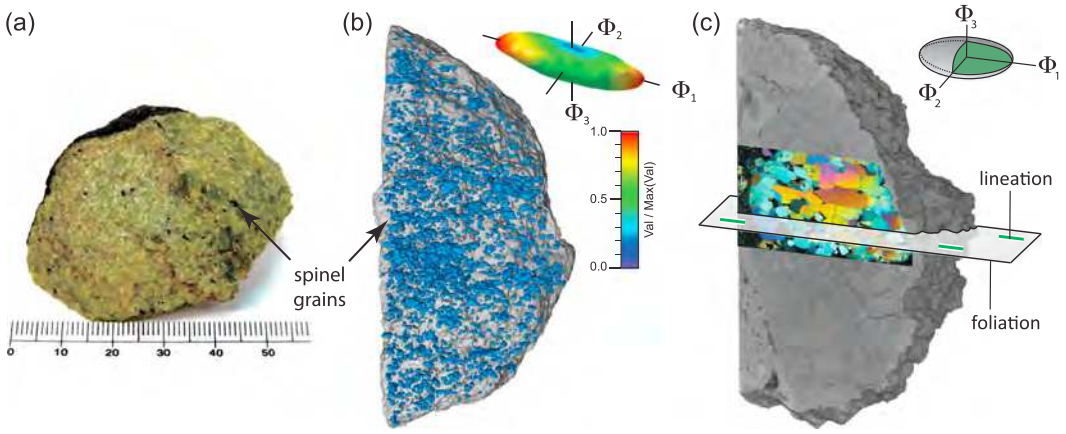

Figure 3. Determination of the spinel shape fabric using X-ray computed tomography. (a) Dunite from Mount Cumming. Black grains are spinel. (b) Reconstructed volume of the scanned xenolith in Figure 3a. Blue objects correspond to spinel grains that have been separated from the olivine mass (grey) on the basis of their density contrast. Three-dimensional rose diagram produced with QUANT3D software describes the fabric ellipsoid calculated from the SPO of the spinel grains. (c) Reconstructed volume of a spinel harzburgite from Demas Bluff. The slice through the volume is parallel to the $\Phi_1\Phi_3$ plane of the spinel fabric ellipsoid. The thin section that was produced from the specific slice of the xenolith is shown as an overlay. The thin section is normal to the foliation plane (contains Φ_1 and Φ_2) and parallel to the lineation (Φ_1).

and Table 1 in the supporting information). In the Fosdick Mountains, mantle xenoliths were entrained in circa 1.4 Ma basaltic to basanitic cinder cones and flows [*Gaffney and Siddoway*, 2007] (Figures 2b and 2c). Geochemical analyses show that the xenolith-bearing lavas are compositionally homogeneous within each volcanic center but heterogeneous among the centers [*Gaffney and Siddoway*, 2007]. We studied 40 spinel-bearing mantle xenoliths of variable composition, including 30 lherzolites, 6 harzburgites, 3 werhlites, and 1 dunite. Xenoliths range between 3 and 15 cm in diameter, are extremely fresh (i.e., lack of significant alteration), and have sharp contacts with the enclosing basalts (Figures 2d and 3a).

3. Methods

To understand what controls the development of olivine CPO in the Marie Byrd Land xenoliths, we compare how changes in deformation conditions and SPO relate to olivine CPO variations. We use X-ray computed tomography to quantitatively describe spinel SPO in terms of orientation (in the hand specimen reference framework), shape, and anisotropy. Electron backscatter diffraction is used to determine patterns of olivine CPO, misorientation axis distributions, olivine SPO, and grain size. Olivine CPO data are plotted relative to the spinel SPO reference framework (i.e., foliation and lineation), which allows for robust and unbiased identification of CPO symmetry and type. We determine mineral compositions and equilibration temperatures by means of electron probe microanalysis. Water content in olivine and orthopyroxene is estimated with Fourier transform infrared spectroscopy. Details for each of the applied methods are provided below.

3.1. X-Ray Computed Tomography

We used high-resolution X-ray computed tomography (XRCT) to visualize and quantify the mineral shape fabric defined by the three-dimensional SPO of spinel grains (Figures 3a and 3b and supporting information Movie S1). XRCT was carried out at the University of Minnesota, Twin Cities, which houses an X5000 high-resolution micro-CT system with a twin head 225 kV cone beam X-ray source and a Dexela area detector (3073 × 3889 pixels). Because the analyzed xenoliths cover a wide range of sizes, different scan parameters were tested and applied (Table S2) to maximize resolution and contrast. Samples were placed on a rotary stage, and 1080 radiographs were collected through 360° of rotation. To reduce noise, three to four radiographs were collected at each angle and averaged (frame averaging), resulting in scan times of 45 min to 2 h and voxel sizes of 10–50 μm. The individual radiographs were then reconstructed into a 3-D volume using the commercial software efX-CT. During the reconstruction a correction was applied to reduce the effects of beam hardening.

Voxels corresponding to spinel were segmented from the voxels corresponding to the remaining constituent phases (olivine, orthopyroxene, and clinopyroxene) following the procedure described in *Ketcham* [2005a]. In case of spinel aggregates, we separated spinel grains manually following an object-based analysis, implemented by the BLOB3D software [*Ketcham*, 2005b]. Spinel grain separation was shape—rather than CPO—based. Where spinel grain separation was not possible, the shape of spinel aggregates was analyzed. We used the 3-D shapes and orientations of the spinel grains and aggregates to determine rock fabric. The SPO of spinel grains was analyzed with QUANT3D software [*Ketcham and Ryan*, 2004]. To calculate the fabric tensor, we used the star length distribution method [*Odgaard et al*., 1997]. To obtain the fabric tensor, the method uses a moment of inertia calculation to define an orientation matrix [*Launeau and Robin*, 1996] from which a fabric tensor is derived by normalizing the eigenvalues to sum to 1. The fabric tensor eigenvectors and eigenvalues define orthogonal principal axes, with the maximum and minimum eigenvectors corresponding to the axes along which the moment of inertia is minimized and maximized, respectively. The eigenvalues are related to the moment of inertia about each axis. Thus, the fabric tensor takes into account both spinel grain shapes and orientations. We used the corrected degree of anisotropy (P') and the shape factor (T) to quantify the anisotropy and shape of fabric ellipsoid [*Jelínek*, 1981]. P' is given by

$$P' = exp\sqrt{2\left[(f_1 - f)^2 + (f_2 - f)^2 + (f_3 - f)^2\right]} \tag{1}$$

where f_1, f_2, and f_3 are the natural logs of the normalized magnitudes of the maximum (Φ_1), intermediate (Φ_2), and minimum (Φ_3) axes of the fabric ellipsoid, respectively, and $f = (f_1 + f_2 + f_3)/3$ [*Jelínek*, 1981]. P' varies from one (sphere—no anisotropy) to infinity (with increasing ellipticity toward a material line or material plane). P' is similar in mathematical formulation to the better known octahedral shear strain [*Nadai*, 1963] used in Hsu plots [*Hossack*, 1968], but P' magnitude may not coincide with the strain magnitude.

The shape factor (T) is mathematically similar to Lode's parameter [*Hossack*, 1968] used in Hsu plots and is defined as

$$\frac{T = 2f_2 - f_1 - f_3}{f_1 - f_3} \tag{2}$$

The values of the shape parameter have the range $-1 < T < 1$, where $T < 0$ corresponds to prolate, $T = 0$ to neutral (plane strain), and $T > 0$ to oblate ellipsoids.

From the fabric tensor we determined the orientations of the three principal fabric ellipsoid axes, which define the foliation plane (contains Φ_1 and Φ_2 axes) and the lineation (parallel to Φ_1) of each xenolith (Figures 3b and 3c). The commercial software Avizo®Fire was used to project the fabric ellipsoid axes on the reconstructed rock volume and subsequently on the rock sample. In 29 samples, thin sections were produced parallel to the $\Phi_1\Phi_3$ plane of the fabric ellipsoid with the long axis of each thin section parallel to Φ_1 (Figure 3c). Thin sections from 11 samples had to be produced at random orientations relative to the spinel fabric due to restrictions imposed by small xenolith size. In these samples, the spinel SPO was determined by means of XRCT analysis of the randomly oriented rock billets.

3.2. Electron Backscatter Diffraction

Crystallographic preferred orientations for all constituent mineral phases in the Marie Byrd Land xenoliths were collected by means of electron backscatter diffraction (EBSD) on polished thin sections. EBSD data were acquired on a Tescan Vega 3 LMU scanning electron microscope equipped with a LaB6 source and an Oxford Instruments Nordyls Max2 EBSD detector housed within the Department of Earth and Environmental Sciences at Boston College. Typical operating conditions for analyses were 20–100 nA for beam currents and an accelerating voltage of 30 kV. Crystallographic texture maps of full thin sections (26 × 46 mm) were acquired and indexed using the Oxford Instruments AZtecHKL acquisition and analysis software (version 2.3). The analytical method is described in detail by *Prior et al*. [1999].

To ensure a high density of crystallographic orientation data and multiple solutions within individual grains, a step size of 7.5 μm was used throughout map regions; EBSD data sets correspondingly comprise approximately 10 million individual solutions with indexing rates typically >90%. Microstructural maps were constructed from the unprocessed EBSD data sets using version 3.5 of the MTEX MATLAB toolbox for textural analysis (http://mtex-toolbox.github.io), from which one point per grain data (i.e., mean crystallographic

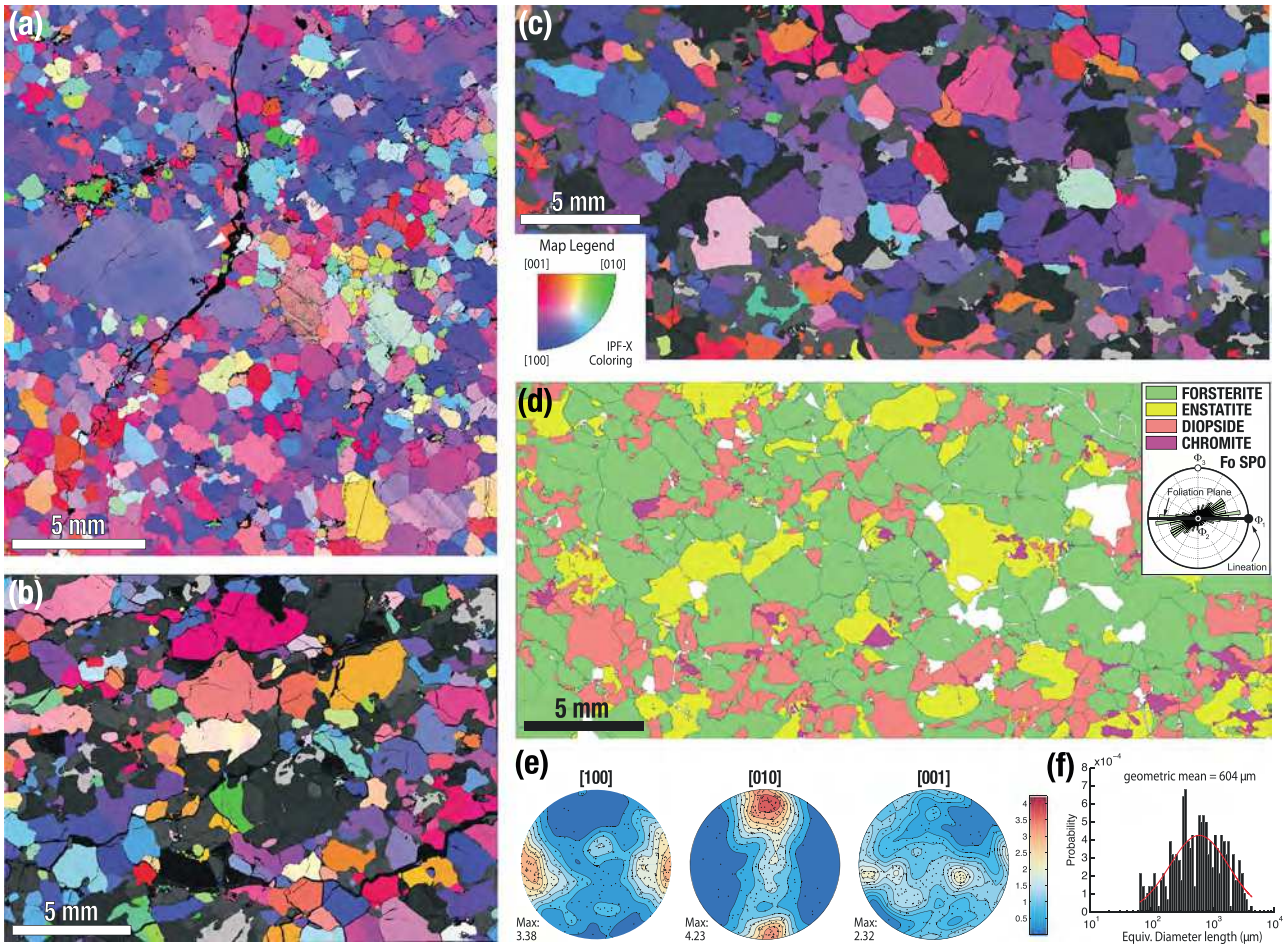

Figure 4. Examples of EBSD maps and representative CPO, SPO, and grain size data. (a) EBSD inverse pole figure map of olivine crystallographic axis orientations in the dunite KSP89-181-X01. Olivine crystal axes orientations are colored relative to Φ_1 axis of the spinel fabric ellipsoid (IPF-X coloring). All maps have upper edge parallel to the XRCT-determined Φ_1 spinel ellipsoid axis (lineation) with the foliation normal to the map. White arrows highlight subgrain boundaries in olivine grains. (b) Combined EBSD phase map and inverse pole figure map of olivine crystallographic axis orientations for the spinel lherzolite FDM-AV01-X01. Grains are as follows: white, spinel; light grey, clinopyroxene; and dark grey, orthopyroxene. Olivine grains are shown with IPF-X coloring. (c) Combined EBSD phase map and olivine IPF-X map for the spinel lherzolite FDM-RN02-X01. Map coloring as in Figure 4b. (d) EBSD phase map of Figure 4c. The inset rose diagram describes the orientation of the long axis of olivine grains plotted relative to the spinel fabric ellipsoid axes. Note the strong alignment of olivine long axes subparallel to long Φ_1 axis of the spinel fabric ellipsoid. (e) Lower hemisphere equal area projections of olivine crystallographic axis orientations. Data from the EBSD map in Figure 4c, plotted as one point per grain. Pole figures are plotted in the reference frame of the spinel fabric ellipsoid as determined by XRCT. Note the strong concentration of [100] axes near Φ_1, which agrees with the IPF-X map in Figure 4c. (f) Frequency distribution of olivine grain size calculated as equivalent circular diameter. The histogram has a logarithmic scale. The red curve represents the lognormal distribution fit to the measured distribution. Olivine grain size data are from the map in Figure 4c, calculated as one point per grain.

orientation of each grain) were calculated for grains separated by misorientation boundaries of ≥10° [*Bachmann et al.*, 2011] (Figures 4a–4d). Pole figures were produced from the one point per grain data sets for comparison of olivine CPO patterns (Figure 4e). In all samples, the olivine CPO data are plotted in the 3-D spinel SPO reference frame (i.e., relative to the spinel-defined foliation and lineation). Misorientation axes were calculated for correlated misorientation angles between 2° and 10°, and their distributions are plotted relative to the olivine crystal reference framework.

To quantify the strength of olivine CPO, we use the *J* index [*Bunge*, 1982] and *M* index [*Skemer et al.*, 2005]. The *J* index is calculated from the orientation distribution functions using MTEX [*Bachmann et al.*, 2010] and has a value of 1 (random) to infinity (single crystal). The *M* index is calculated from the distribution of uncorrelated misorientation axes and has a value of 0 (random) to 1 (single crystal). We use the BA index [*Mainprice et al.*, 2014] to quantify the tendency of the olivine CPO toward end-member axial-[010] (BA = 0) or axial-[100] (BA = 1) symmetries. The BA index is defined as

$$\text{BA index} = \frac{1}{2}\left(2 - \left(\frac{P_{010}}{G_{010} + P_{010}}\right) - \left(\frac{G_{100}}{G_{100} + P_{100}}\right)\right) \quad (3)$$

where P and G are the Point and Girdle pattern symmetry characteristics of *Vollmer* [1990] for olivine [100] and [010]. The P and G indices were calculated from the eigenvalues of the normalized orientation matrix using MTEX [*Mainprice et al*., 2011].

Two-dimensional olivine SPO (Figure 4d, inset) was determined from grain set properties of the EBSD maps analyzed in MTEX. No olivine SPO data were acquired from thin sections produced at random orientation relative to the spinel shape fabric. The olivine grain size was determined with the equivalent circular diameter method on grains defined by a grain boundary misorientation angle of 10°, constructed from the EBSD data in MTEX. To convert between the mean equivalent circular diameter on a two-dimensional section and the mean grain size in three dimensions, a scaling factor of 1.2 was used [*Underwood*, 1970; *Van der Wal et al*., 1993].

3.3. Electron Probe Microanalysis

The major and minor element compositions of olivine, spinel, orthopyroxene, and clinopyroxene were analyzed by wavelength-dispersion spectrometry with a Cameca SX50 instrument at the Department of Geoscience, University of Wisconsin-Madison. Operating conditions were 15 kV accelerating voltage, 20 nA beam current (Faraday cup), and beam diameter of 1 μm. Combinations of natural minerals and synthetic materials were used as standards for each mineral species, and data reduction was performed by Probe for Windows software, utilizing the $\varphi(\rho z)$ matrix correction of *Armstrong* [1988].

Mineral compositions were analyzed in each sample in several domains, situated at different structural positions relative to the determined foliation. Constituent phases of interest were analyzed in each domain, and compositions were determined for cores and rims in each phase. Where possible, adjacent grains of olivine, spinel, orthopyroxene, and clinopyroxene were analyzed. No significant compositional differences were found on the intergranular or intragranular scales, except that enstatite and Cr-diopside grains in a few samples contain exsolution lamellae of the complementary pyroxene and spinel. Such lamellae were too thin to allow for accurate analyses, and consequently, the host compositions of coexisting orthopyroxene and clinopyroxene were used to calculate temperature. Representative analyses of constituent minerals are summarized in Table S3.

Equilibration temperatures for the Marie Byrd Land xenoliths were determined by application of three different calibrations of the two-pyroxene geothermometer (Table S4), namely, those by *Bertrand and Mercier* [1985] (BM85), *Brey and Köhler* [1990] (BK90), and *Taylor* [1998] (T98). For the dunite sample we used the olivine-spinel Fe-Mg exchange geothermometer of *Ballhaus et al*. [1991] (BBG91). Temperatures were calculated at an assumed pressure of 15 kbar, because of the uncertainty in estimating pressures for spinel peridotites (see section 4.3). The effect of pressure on calculated two-pyroxene temperatures is 2°C/kbar.

3.4. Fourier Transform Infrared Spectroscopy

Fourier transform infrared (FTIR) spectroscopic measurements were made to determine the H content of olivine and orthopyroxene from seven peridotite xenoliths (FDM-AV01-X01, FDM-BB01-X01, FDM-DB03-X01, FDM-RN03-X01, FDM-RN04-X01, FDM-AVBB02, and AD6021-X02) and olivine from a dunite xenolith (KSP89-181-X01). Polarized spectra were collected in transmission mode using a Bruker Tensor 37 FTIR spectrometer and Hyperion 2000 microscope with 15X objective and condenser. An infrared globar source and Mercury Cadmium Telluride (MCT) detector were used, and 128 scans were taken over spectral range of 1000–5000 cm^{-1} with a sampling interval of 1 cm^{-1}. The aperture was adjusted so that the analyzed area formed a square with edge length between 50 and 100 μm. After they had been disaggregated from the xenoliths, orthopyroxene and olivine grains that exhibited the best developed crystal faces were selected for FTIR analysis. We prepared polished sections perpendicular to the α axes of the infrared indicatrices by polishing parallel to the (100) faces of orthopyroxene and (010) faces of olivine. Sample orientation was confirmed, and β and γ directions were identified, by comparing spectra in the region from 1400 to 2300 cm^{-1}, where diagnostic Si-O overtone bands occur, with reference spectra for olivine from *Asimow et al*. [2006] and for orthopyroxene from *Mosenfelder and Rossman* [2013]. Well-oriented samples were selected and

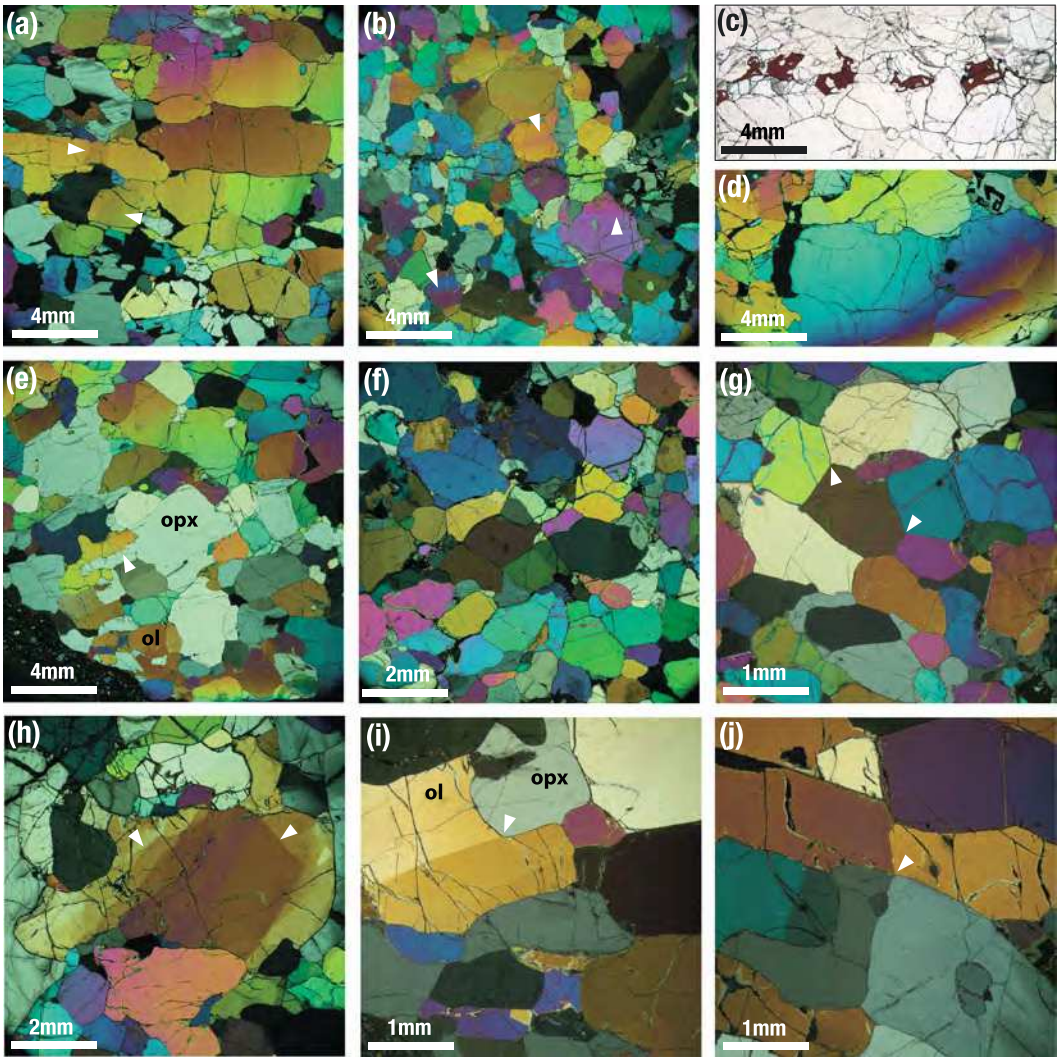

Figure 5. Typical microstructures in the Marie Byrd Land spinel peridotite xenoliths. In all photomicrographs lineation is parallel to the top edge and foliation is normal to the photomicrograph. (a) Coarse-grained harzburgite characterized by alignment of tabular olivine crystals with straight grain boundaries parallel to the foliation; widely spaced subgrain boundaries (white arrows) are oriented perpendicular to the foliation (FDM-DB02-X08). (b) Coarse-grained lherzolite with granular microstructure. Olivine subgrain boundaries are predominantly oriented at low angle to the foliation, but subgrain boundaries oblique to the foliation are also present (AD6021-X02). (c) Lherzolite with spinel trail formed by discrete, subhedral spinel grains (FDM-DB03-X04). (d) Olivine crystal with undulose extinction in a coarse-grained granular harzburgite (FDM-DB02-X02). (e) Aligned olivine-orthopyroxene grain boundaries in a spinel harzburgite. Arrow points to one of the aligned boundaries. Olivine subgrain boundaries are oriented both perpendicular and at low angle to the foliation. In the latter case, the subgrain boundaries are parallel to the olivine-orthopyroxene grain boundaries. Note the diamond grain structure of the orthopyroxene grain in the center, which is indicative of grain boundary sliding (FDM-DB04-X03). (f) Granular lherzolite with alignment of olivine grain boundaries oblique (lower left to upper right) to the spinel foliation (FDM-AV01-X01). (g) Granular lherzolite with 120° triple junctions (white arrows) between olivine grains (FDM-AVBB02). (h) Olivine grain with two sets of subgrain boundaries, at high angle to each other. Both subgrain boundary sets are oriented oblique to the foliation (FDM-DB02-X10). (i) Detail of the aligned olivine-orthopyroxene grain boundaries shown in Figure 5e. Olivine subgrain boundary aligned to the olivine-orthopyroxene grain boundary. This microstructure may suggest phase boundary sliding (FDM-DB04-X03). (j) Olivine and orthopyroxene grains forming a four-grain junction, characteristic of grain boundary sliding (FDM-DB03-X01). All photomicrographs are under crossed-polarized light, except 5c, which is taken in plane-polarized light.

repolished to prepare sections orthogonal to those containing the β and γ directions, so that principal spectra with the electric vector of the infrared light polarized parallel to the α axis of the infrared indicatrix (the "α spectra") could be measured. The spectra for orthopyroxene are a close match to the respective principal polarized spectra for sample KBH-1 of *Bell et al*. [1995] (Figure S1), so we calculated H_2O concentration for

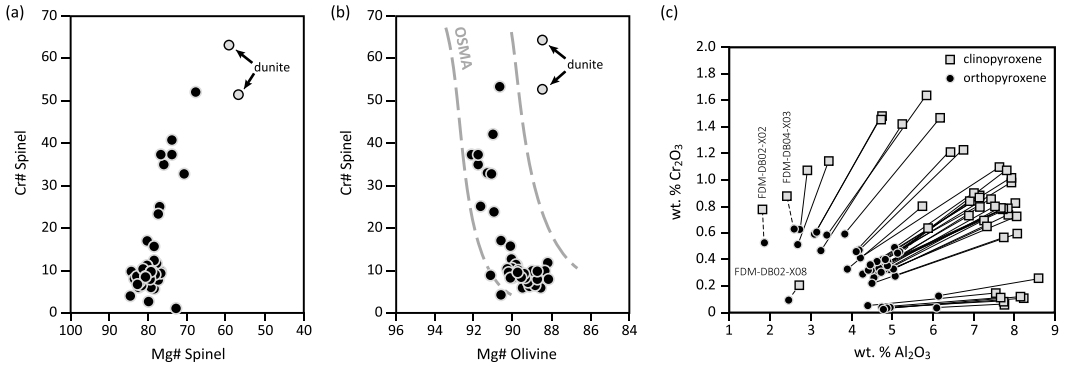

Figure 6. Graphical representation of geochemical data. (a) Variation in spinel composition in terms of Cr# and Mg#. (b) Correlation of Cr# in spinel with Mg# in olivine in the Marie Byrd Land peridotite xenoliths. The field for subcontinental spinel xenoliths is shown for comparison [*Arai*, 1994]. OSMA: olivine-spinel mantle array. (c) Contents of Cr_2O_3 and Al_2O_3 in coexisting orthopyroxene and clinopyroxene in the studied peridotite xenoliths. The subparallel tie lines between orthopyroxene and clinopyroxene indicate chemical equilibration among the pairs of pyroxenes.

the orthopyroxene using the molar absorption coefficient of *Bell et al*. [1995], while for olivine we used the molar absorption coefficient of *Withers et al*. [2012].

4. Results

4.1. Microstructures

Microstructures in the Marie Byrd Land xenoliths were studied by combined optical (Figure 5) and electron microscopy (e.g., EBSD maps; Figure 4) techniques. The xenoliths are coarse grained and have a granular or tabular microstructure (Figures 4b, 4c, 5a, and 5b). Spinel occurs as discrete, euhedral to subhedral grains and commonly forms characteristic spinel trails (Figure 5c). Interstitial, symplectic, or complexly shaped irregular intergrowths of spinel with pyroxene are also present but less common. Olivine grains show undulose extinction (Figure 5d) and well-developed subgrain boundaries (Figures 4a, 5a, 5b, 5e, 5f, 5h, and 5i). The subgrain boundaries are usually oriented perpendicular or oblique (at high angle) to the foliation (Figures 4a, 5a, 5e, and 5f); however, subgrain boundaries subparallel or at low angle to the foliation are also present (Figures 5b, 5e, and 5i). Gently curved to straight olivine-olivine grain boundaries, which lead to polygonal crystal shapes with 120° triple junctions, are indicative of an equilibrium microstructure (Figure 5g). Recrystallization, accommodated by grain boundary migration, is inferred from interpenetrating olivine grain boundaries [*Drury and Urai*, 1990].

Several microstructures identified in the xenoliths are indicative of grain boundary sliding: (1) olivine tabular grains with straight grain boundaries oriented subparallel to the foliation (Figure 5a); (2) presence of diamond-shaped grains with grain boundaries forming conjugate sets trending at 20–50° to the foliation (Figures 5e and 5f); (3) along-strike continuity between subgrain and grain boundaries, the subgrain boundaries forming in zones of sliding accommodation strain at triple points (Figure 5i); and (4) presence of four-grain junctions (Figure 5j) [*Ashby and Verrall*, 1973; *Drury and Humphreys*, 1988; *Ree*, 1994; *Newman et al*., 1999; *Sundberg and Cooper*, 2008]

4.2. Mineral Compositions

Minerals in the Marie Byrd Land mantle xenoliths are highly magnesian and have compositional characteristics typical for those in subcontinental peridotite xenoliths [e.g., *Arai*, 1994]. Spinel shows significant variation in both Mg# ($100 \times [Mg/(Mg + Fe)]$) and Cr# ($100 \times [Cr/(Cr + Al)]$), which range from 56.7 to 84.6 and 1.3 to 63.1, respectively (Figure 6a). The majority of the xenoliths (77%) contain spinel with Mg-rich and Cr-poor (Cr# < 20) compositions, which are typical for relatively undepleted mantle peridotites. Olivine is Mg rich, with Mg# values ranging between 88.2 and 92.1, and the Mg# in olivine tends to increase with an increase in Cr# in coexisting spinel (Figure 6b). With the exception of the dunite sample (KSP89-181-X01), all xenoliths plot within or at the border of the olivine-spinel mantle array (OSMA), as established by *Arai* [1994] (Figure 6b).

Orthopyroxene and clinopyroxene are Mg rich, with Mg# ranging between 83.7–92.5 and 82.4–94.8, respectively. Pyroxenes show large sample-to-sample variation in Al_2O_3 and Cr_2O_3 contents, where the range in Al_2O_3 for

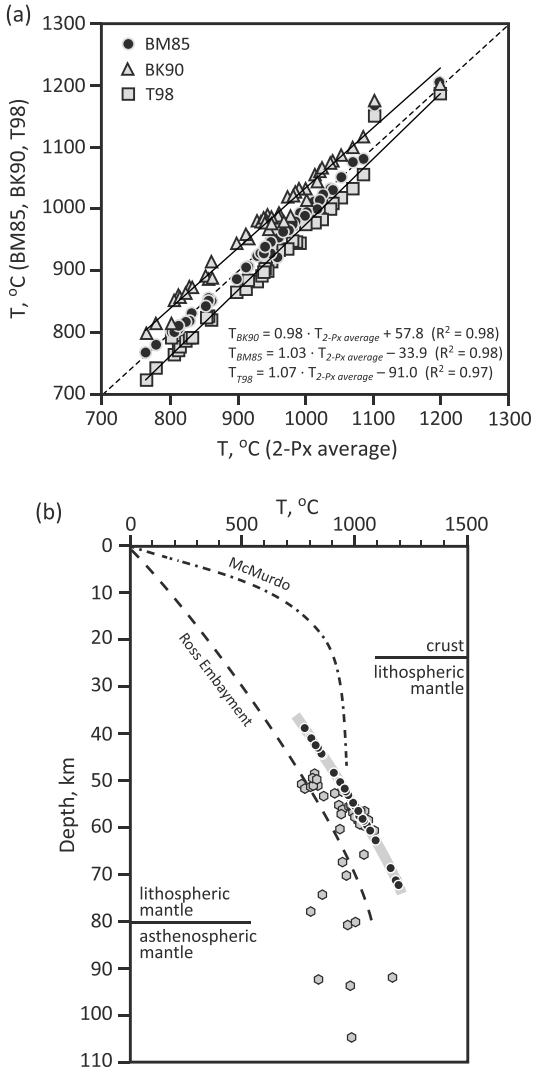

Figure 7. Equilibration temperatures and extraction depths estimated for the Marie Byrd Land xenoliths. (a) Comparison of temperature estimates (calculated at 15 kbar) from the three two-pyroxene geothermometers (BM85 [*Bertrand and Mercier*, 1985], BK90 [*Brey and Köhler*, 1990], and T98 [*Taylor*, 1998]) with their average. (b) Estimated equilibration temperatures and extraction depths for the spinel peridotite xenoliths. Black symbols indicate temperature-depth values obtained by combining the averages of the three, two-pyroxene geothermometers with a hypothetical geotherm at 1.5 Ma. Grey symbols represent the maximum depths for spinel stability in each sample, and the thick grey line indicates an inferred geotherm at 1.5 Ma that is consistent with the stability of spinel in all samples of the xenolith suite. The McMurdo petrologic geotherm [*Berg et al*., 1989] and the present-day Ross Embayment geotherm [*ten Brink et al*., 1997] are shown for comparison.

orthopyroxene is 1.86–6.14 wt %, and for clinopyroxene is 1.82–8.61 wt %, as illustrated for coexisting pyroxenes in Figure 6c. The configuration of the data points reflects equilibration temperatures (higher Al_2O_3 generally representing higher temperatures) and whole-rock Cr_2O_3/Al_2O_3 ratios. Tie lines are subparallel for most xenoliths, which implies chemical equilibrium for Al_2O_3 and Cr_2O_3 in the coexisting pyroxenes. Two samples (FDM-DB02-X02 and FDM-DB04-X03) display discordant tie lines relative to the other samples, reflecting disequilibrium with respect to Al_2O_3 and Cr_2O_3. Pyroxenes in sample FDM-DB02-X08 contain relatively small amounts of Al_2O_3 and Cr_2O_3 and equilibrated at a lower temperature than did other xenoliths from the same volcanic center.

4.3. Equilibration Temperatures and Extraction Depths

Temperatures from the three two-pyroxene geothermometers are in very good agreement (Figure 7a), and the average temperature estimates range from 780 to 1200°C, calculated at a pressure of 15 kbar (Table 1). These temperatures are thought to represent the xenolith temperatures at the time of extraction from the mantle, but note that samples that contain pyroxene exsolution lamellae must have cooled from some unknown higher temperature prior to extraction.

The average of the three two-pyroxene geothermometers is used to estimate temperatures for the Marie Byrd Land xenoliths at the time of extraction. The regular distribution of subparallel Al_2O_3 and Cr_2O_3 tie lines in pyroxenes (Figure 6c) and the excellent agreement between the results of the three two-pyroxene geothermometers (Figure 7a) together indicate the attainment and preservation of equilibrium in pyroxenes with respect to Ca, Mg, Fe, Al, and Cr.

Currently, there is no reliable geobarometer for direct calculation of pressure, and therefore depth, for spinel peridotites. However, we can predict the maximum extraction depth for each xenolith by calculating the maximum pressure at which spinel, rather than garnet, would be stable in each peridotite xenolith [*O'Neill*, 1981]. This approach is valid for the Marie Byrd Land xenoliths, which are devoid of garnet. The compositionally controlled stability limit for spinel ranges from 49 to 105 km and corresponds to the predicted maximum possible extraction depth of the studied peridotite xenoliths (Figure 7b and Table S4). The wide range in the predicted maximum depths is due to the large variation in Cr# of spinel in the xenolith suite, i.e., higher Cr contents stabilize spinel to higher pressures.

Table 1. Equilibration Temperature, Grain Size, Differential Stress, Olivine CPO Type, CPO Strength, and Spinel Fabric[a]

Volcanic Center	Xenolith	Temperature (°C)	D (μm)	σ (MPa)	Olivine CPO Type	J	M	BA	P'	T
Bird Bluff	FDM-BB03-X01	856	1180	06	Axial-[010]	4.07	0.21	0.12	1.16	−0.19
Mount Avers-Bird Bluff	FDM-AVBB01	937	214	25	Axial-[010]	2.19	0.12	0.13	1.11	0.01
Demas Bluff	FDM-DB02-X12	1036	599	10	Axial-[010]	3.32	0.16	0.17	1.22	0.67
Mount Avers-Bird Bluff	FDM-AVBB02	779	133	35	Axial-[010]	1.97	0.11	0.22	1.29	0.65
Mount Avers-Bird Bluff	FDM-AVBB04	822	587	10	Axial-[010]	1.88	0.09	0.22	1.10	0.02
Demas Bluff	FDM-DB04-X01	991	1450	06	Axial-[010]	4.03	0.20	0.23	1.09	0.15
Mount Avers-Bird Bluff	FDM-AVBB06	940	192	25	Axial-[010]	1.90	0.08	0.25	1.14	0.13
Mount Avers-Bird Bluff	FDM-AVBB07	805	644	10	Axial-[010]	1.87	0.08	0.26	1.28	0.35
Mount Avers-Bird Bluff	FDM-AVBB08	832	285	19	Axial-[010]	3.27	0.12	0.26	1.12	0.84
Mount Aldaz	AD6021-X02	1084	815	09	Axial-[010]	3.54	0.20	0.27	1.14	−0.06
Demas Bluff	FDM-DB03-X02	861	545	10	Axial-[010]	2.77	0.20	0.28	1.24	−0.11
Demas Bluff	FDM-DB04-X02	984	647	10	Axial-[010]	3.37	0.16	0.29	1.25	−0.23
Mount Avers-Bird Bluff	FDM-AVBB05	814	61	60	Axial-[010]	1.73	0.14	0.31	1.23	−0.08
Marujupu	FDM-MJ01-X05	1014	90	46	Axial-[010]	3.80	0.16	0.33	1.24	0.25
Demas Bluff	FDM-DB02-X04	933	1230	07	na	–	–	0.35	1.32	0.53
Demas Bluff	FDM-DB02-X03	999	210	25	Axial-[010]	4.50	0.31	0.37	1.15	0.36
Demas Bluff	FDM-DB02-X11	1039	1610	06	A	3.54	0.20	0.38	1.25	−0.22
Marujupu	FDM-MJ01-X06	1070	133	35	A	1.46	0.13	0.41	1.23	0.60
Bird Bluff	FDM-BB02-X01	1053	322	20	Random	1.40	0.02	0.42	1.23	−0.34
Mount Avers	FDM-AV01-X01	939	111	40	A	2.92	0.18	0.43	1.15	0.02
Recess Nunatak	FDM-RN03-X01	943	346	15	B	3.30	0.15	0.43	1.13	0.68
Recess Nunatak	FDM-RN01-X01	961	1290	07	A	14.34	0.24	0.44	1.30	−0.32
Bird Bluff	FDM-BB01-X01	945	122	35	A	1.39	0.07	0.48	1.15	0.22
Demas Bluff	FDM-DB02-X08	803	1310	05	A	7.07	0.37	0.48	1.18	−0.56
Marujupu	FDM-MJ01-X02	974	513	10	A	4.00	0.20	0.50	1.40	−0.08
Demas Bluff	FDM-DB02-X02	978	2000	05	A	8.95	0.36	0.51	1.34	0.11
Marujupu	FDM-MJ01-X03	929	100	42	A	2.70	0.09	0.51	1.32	0.16
Demas Bluff	FDM-DB04-X04	968	1310	06	A	4.40	0.28	0.56	1.21	−0.43
Recess Nunatak	FDM-RN02-X01	828	604	10	A	2.75	0.16	0.57	1.32	0.20
Demas Bluff	FDM-DB02-X10	1020	736	10	A	4.30	0.26	0.58	1.15	−0.94
Demas Bluff	FDM-DB01-X01	1024	885	08	Axial-[100]	2.82	0.14	0.60	1.29	0.28
Recess Nunatak	FDM-RN04-X01	812	528	10	Axial-[100]	2.71	0.20	0.62	1.27	−0.24
Demas Bluff	FDM-DB02-X13	911	933	08	Axial-[100]	2.33	0.08	0.67	1.23	−0.09
Demas Bluff	FDM-DB03-X01	856	1460	06	Axial-[100]	5.55	0.25	0.68	1.29	−0.85
Demas Bluff	FDM-DB02-X01	1183	494	13	Axial-[100]	3.05	0.20	0.74	1.27	−0.35
Demas Bluff	FDM-DB03-X03	982	898	08	Axial-[100]	2.72	0.09	0.77	1.19	−0.08
Mount Cumming	KSP89-181-X01	862/955	455	15	Axial-[100]	4.34	0.34	0.81	1.61	0.44
Demas Bluff	FDM-DB04-X03	1165	1360	06	Axial-[100]	4.88	0.17	0.86	1.23	−0.67
Demas Bluff	FDM-DB02-X06	1198	314	20	na	–	–	0.45	1.13	−0.36
Demas Bluff	FDM-DB03-X04	1002	900	08	na	–	–	0.38	1.15	−0.66

[a]Temperature, 2-Px average; D, equivalent circular diameter grain size; σ, differential stress; P', fabric anisotropy; and T, shape parameter. na: not assigned.

Further constraints on the depths of xenolith extraction can be placed by combining the results of geothermometry with a geotherm at the time of eruption [e.g., *Medaris et al.*, 2015]. Such an approach can be applied to the Marie Byrd Land spinel peridotite xenoliths by combining the average results of the two-pyroxene geothermometers with an appropriate geotherm. Two geotherms have been established in the region: the McMurdo petrologic geotherm [*Berg et al.*, 1989] and the present-day Ross Embayment geotherm [*ten Brink et al.*, 1997] (Figure 7b). However, neither geotherm is appropriate for the Marie Byrd Land xenolith suite, because the use of the McMurdo geotherm would place 50% of the xenoliths above the Moho, and application of the Ross Embayment geotherm would require that 73% of the samples contain garnet, rather than spinel (Figure 7b). Alternatively, a geotherm has been constructed that is consistent with the stability of spinel in all xenoliths (the thick gray line in Figure 7b, whose width corresponds to the ±25°C precision of the two-pyroxene geothermometers). Depths for the Marie Byrd Land xenoliths are then estimated by intersecting their pressure-dependent two-pyroxene temperatures with the hypothetical geotherm (Figure 7b and Table S4). The range of xenolith temperatures represents depths between 39 and 72 km, indicating that the Marie Byrd Land xenoliths have been extracted from moderate to relatively deep levels of the lithospheric mantle.

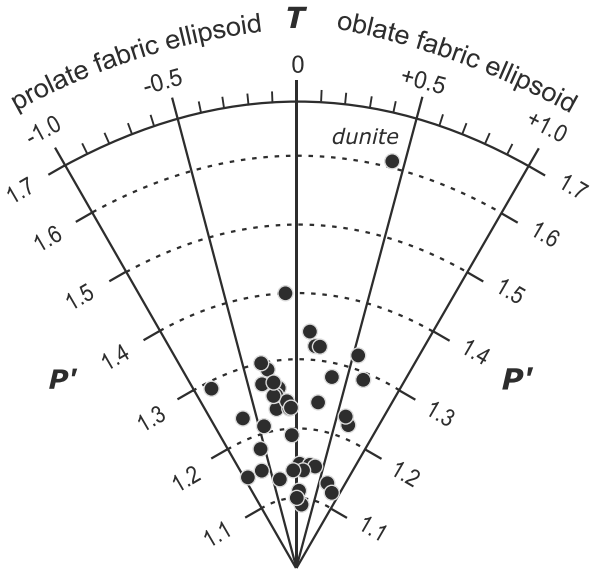

Figure 8. Hsu plot showing the relationship between the degree of anisotropy (*P'*, radial component) and the shape factor (*T*, tangential component) as determined by means of XRCT for the Marie Byrd Land xenoliths.

4.4. Three-Dimensional Spinel Shape Preferred Orientation

The Marie Byrd Land xenoliths are characterized by low values of the degree of anisotropy (*P'*) of the spinel fabric ellipsoid, which range from 1.09 to 1.61 (Figure 8 and Table 1). Low anisotropy suggests small deviation of the shape of the mean spinel fabric ellipsoid from a sphere. Nonetheless, the low *P'* values are comparable to the orthopyroxene fabric ellipsoid anisotropy (*P'* = 1.08–1.15) reported from spinel peridotites from the Bogota Peninsula shear zone in New Caledonia [*Titus et al.*, 2011]. The shape parameter (*T*) ranges from −0.94 to 0.84, showing large variation in the geometry of the spinel fabric ellipsoid (Table 1 and Figure 8). The Marie Byrd Land xenoliths are mainly characterized by either oblate or prolate fabric ellipsoids, and only eight samples have neutral ellipsoid shapes (*T* close to 0). Our data show no obvious correlation between the degree of anisotropy and the geometry of the spinel fabric ellipsoid (Figure 8).

Visual comparison of the orientation of the XRCT-derived 3-D spinel shape fabric and the microstructures observed in the xenoliths suggests correlation between the two. The determined $\Phi_1\Phi_2$ plane (foliation) of the fabric ellipsoid is oriented parallel to the 3-D spatial distribution of spinel grains in layers. Further, the Φ_1 axis (lineation) of the fabric ellipsoid, which corresponds to the trend of spinel grains' long axis alignment (Figures 3b and 3c), coincides with the trend of observed spinel trails (Figure 5c).

To explore the relationship between the spinel and olivine shape fabric, we analyze the 2-D olivine SPO in thin sections cut parallel to the $\Phi_1\Phi_3$ plane of the spinel fabric ellipsoid. In 80% of the xenoliths for which olivine SPO was determined, olivine grains show a clear tendency to align with their long axes parallel or at a small angle (<10°) to the spinel lineation (Figure 9). The long axes of olivine grains are oriented at intermediate or high angle to the spinel lineation in six samples (AD6021-X02, FDM-AV01-X01, FDM-RN03-X01, FDM-BB01-X01, FDM-DB02-X01, and KSP89-181-X01). Our data indicate that the 2-D olivine SPO is consistent with the orientation of the spinel fabric ellipsoid. However, the 2-D treatment of the olivine SPO imposes restrictions on further exploring the relationship between the spinel and olivine fabric ellipsoids in 3-D.

4.5. Crystallographic Preferred Orientations

Olivine CPOs from the analyzed xenoliths are presented in Figure 9; samples are organized based on their BA index value. Olivine CPOs are plotted with respect to the spinel foliation and lineation as determined with XRCT for all samples, which allows for the accurate identification of the CPO symmetry and type. The Marie Byrd Land xenoliths exhibit a variety of olivine CPO types; four out of six CPO types observed in nature and reproduced by deformation experiments (Figure 1a) are recognized. The observed CPO types include the A type and B type with orthorhombic symmetry, as well as the axial-[010] and axial-[100] symmetries (Figure 9 and Table 1). The variation in olivine CPO is also expressed by the BA index, which ranges from 0.12 to 0.86 (Figure 9 and Table 1).

Olivine A-type CPO with orthorhombic symmetry is recognized in 12 xenoliths (Figure 9 and Table 1). The A type is characterized by point concentrations of the three olivine crystal axes, with the [100] axes aligned parallel or at small angle to the spinel lineation (Φ_1), the [010] axes parallel or at small angle to the pole to the foliation (Φ_3), and the [001] axes oriented normal to the lineation within the foliation plane (parallel to Φ_2) (Figure 9). The agreement in the orientation of the olivine crystal axes and the spinel fabric ellipsoid axes

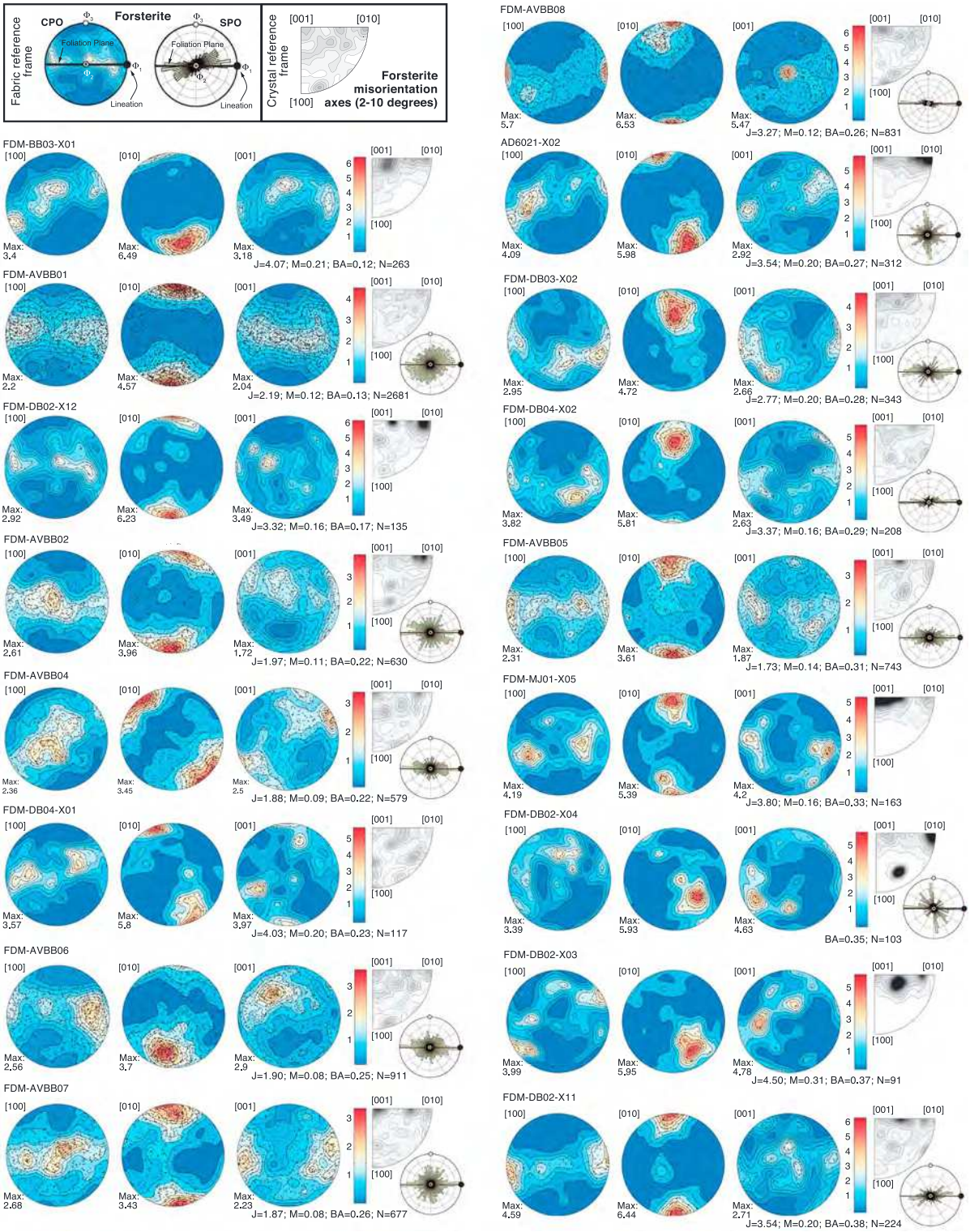

Figure 9. Crystallographic orientations, low-angle misorientations, and shape-preferred orientations of olivine grains. Samples are organized with increasing BA index value. Crystallographic orientations are plotted as one point per grain data sets in lower hemisphere equal area projections, relative to the spinel fabric ellipsoid axes. Color scales are for multiples of uniform distribution. For each sample, the BA, *J*, and *M* indices, as well as the number of grains analyzed, are given. Misorientation axes are from correlated misorientation angles between 2° and 10°. Inverse pole figures are in the crystallographic reference frame. Orientations of the long axes of olivine grains relative to the spinel fabric ellipsoid axes are shown in rose diagrams.

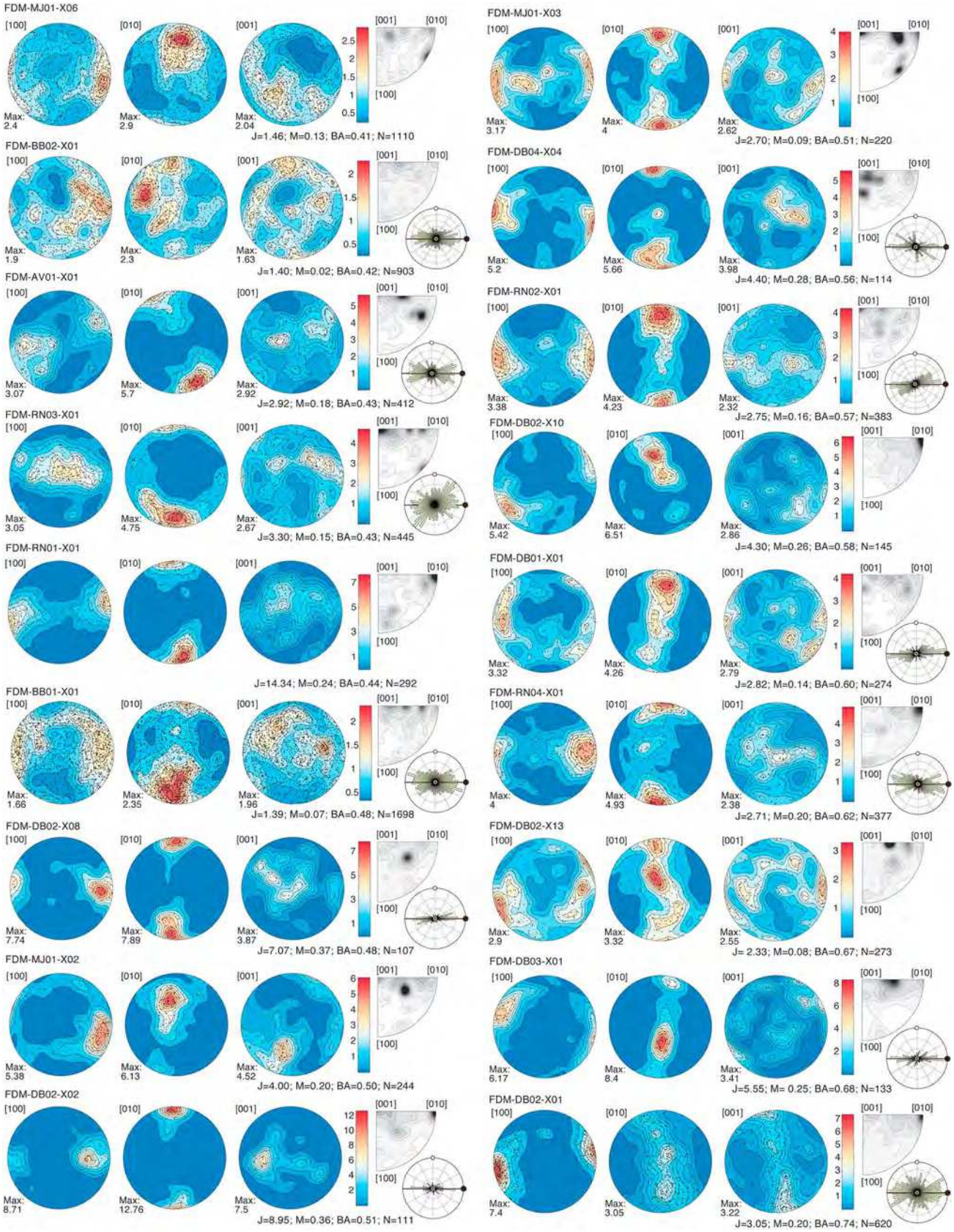

Figure 9. (continued)

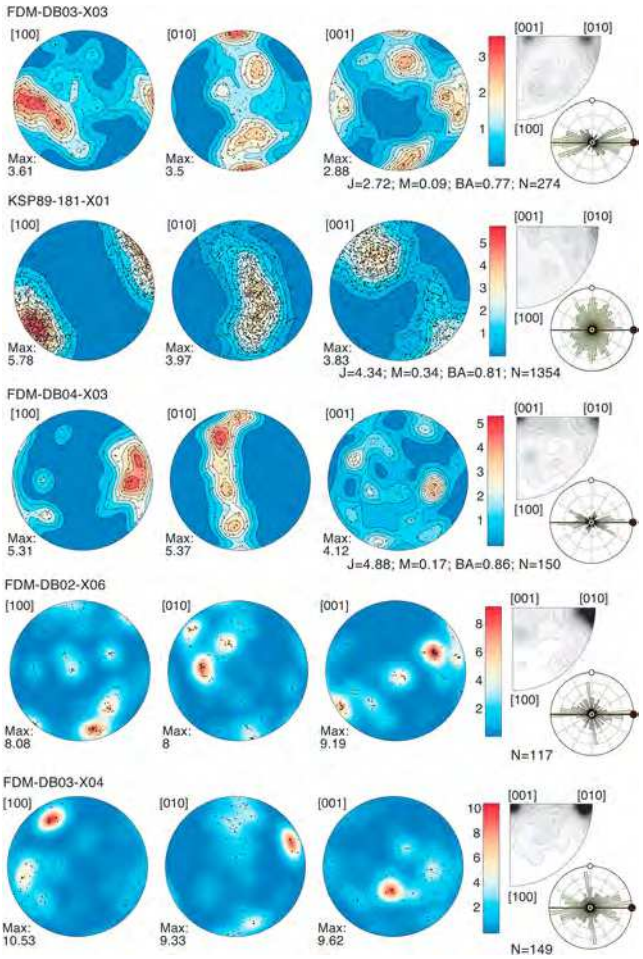

Figure 9. (continued)

observed for the A-type pattern provides further evidence for the robustness of the determined spinel fabric ellipsoid, used to plot and interpret the olivine CPO data.

Olivine axial-[010] symmetry is recognized in 15 xenoliths (Figure 9 and Table 1). The CPOs are characterized by [010] point concentrations normal or at high angle to the foliation plane, while [100] and [001] axes form girdles within or close to the foliation plane. Within the [100] and [001] girdles, the maxima of the crystal axis distributions trend either parallel or oblique to Φ_1 and Φ_2 fabric ellipsoid axes.

Olivine CPO in eight samples is characterized by point concentrations of [100] near Φ_1 axis, while [010] are typically distributed along girdles at high angle to the lineation (Figure 9). Within the [010] girdles, the maximum concentration of axes is near either Φ_2 or Φ_3. In sample FDM-DB02-X01, the [001] axes show girdle distribution normal to the spinel lineation. However, in the rest of the xenoliths, the orientation of [001] axes is commonly dispersed leading to more complex or random distributions, which can be a common characteristic of deformed, polyphase rocks [*Ben Ismail and Mainprice*, 1998; *Bystricky et al*., 2006]. The olivine CPO in these eight xenoliths may therefore be classified as having an axial-[100] symmetry (Figure 9 and Table 1). Such classification is also supported by the high BA index values (typically $>$0.6) in these samples.

The B-type olivine CPO pattern is recognized in sample FDM-RN03-X01 (Figure 9). The CPO is characterized by Φ_2-parallel [100] axes that lie within the foliation plane, [010] axes normal to the foliation (parallel to Φ_3), and [001] axes oblique to Φ_1.

One xenolith (FDM-BB02-X01), with equigranular microstructure and abundant 120° triple junctions of olivine grains, has a random texture (Figure 9). Insufficient number of analyzed olivine grains in two xenoliths (FDM-DB02-X04 and FDM-DB03-X04) prevents us from ascribing the poorly developed crystallographic texture to a specific CPO symmetry (Figure 9).

Most xenoliths have moderate to low olivine CPO strength. The *J* index varies from 1.39 to 14.34 with an arithmetic mean of 3.67 (Figure 9 and Table 1). This mean *J* index value is smaller than the value of 8–10 characterizing most natural peridotites [*Ben Ismail and Mainprice*, 1998; *Tommasi et al*., 2000]. In agreement with *J* index, the calculated *M* index is moderate to low, ranging between 0.07 and 0.37 (arithmetic mean of 0.18).

4.6. Crystallographic Misorientations and Active Slip Systems

Low-angle (2–10°) boundaries in deformed grains develop as a result of dislocation creep and organization of dislocations into planes of lower energy due to recovery. Organization of edge dislocations produces tilt

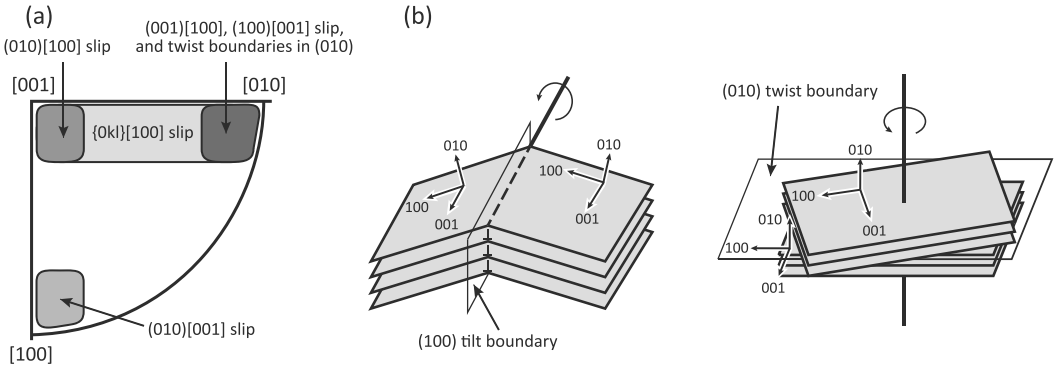

Figure 10. (a) Inverse pole figure showing the misorientation axis distributions expected for different slip systems in olivine. Modified after *De Kloe* [2001]. (b) Schematic diagram showing lattice rotations across subgrain tilt and twist boundaries. Modified after *Lloyd et al*. [1997].

boundaries, while organization of screw dislocations forms twist boundaries (Figure 10b). The combined analysis of CPO and low-angle misorientation axes allows the determination of the slip systems that may be active for the formation of the low-angle boundaries [*Lloyd et al*., 1997]. Using EBSD mapping, we analyzed low-angle (2–10°) misorientation axes to investigate (1) the olivine slip systems that produce the subgrain boundaries for the different CPO types and (2) intracrystalline deformation of spinel grains.

4.6.1. Olivine

The majority of the xenoliths with A-type CPO pattern are characterized by low-angle misorientation axes distributed along girdles between [001] and [010] (Figure 9; FDM-DB02-X11, FDM-BB02-X01, FDM-AV01-X01, FDM-BB01-X01, FDM-DB02-X08, FDM-MJ01-X02, and FDM-MJ01-X03). Such distribution of misorientation axes is characteristic of {0kl}[100] slip system (Figure 10a). In the remaining xenoliths with A-type CPO pattern, the misorientation axes are clustered near either [001] (FDM-DB04-X04 and FDM-RN02-X01) or [010] (FDM-RN01-X01 and FDM-DB02-X10) or both (FDM-MJ01-X06 and FDM-DB02-X02). Concentration of misorientation axes near [001] is indicative of the presence of tilt boundaries in (100) and therefore for the activity of (010)[100] slip system (Figure 10a). Clustering of misorientation axes near [010] is possibly related to the existence of twist boundaries in (010) (Figure 10a). Due to the A-type CPO, formation of either tilt boundaries in (001) associated with (100)[001] slip or tilt boundaries in (100) associated with (001)[100] slip is a less plausible explanation because most grains would have low shear stress on these slip systems.

The xenoliths with olivine CPO of axial-[010] symmetry are predominantly characterized by low-angle misorientation axes that show girdle distributions between [001] and [010] (Figure 9). Within the girdles, the misorientation axis distributions exhibit maxima oblique to both [001] and [010] (FDM-BB03-X01, FDM-DB04-X02, FDM-AVBB05, and FDM-DB02-X03), which suggests activity of the {0kl}[100] slip system (Figure 10a). Maxima of the misorientation axis distributions near [001] in four xenoliths (FDM-AVBB07, FDM-AVBB08, FDM-DB03-X02, and FDM-MJ01-X05) indicate arrangement of dislocations along [100] tilt boundaries via (010)[100] slip. Clustering of misorientation axes near [010] (FDM-DB02-X12, FDM-AVBB02, and AD6021-X02) can be the result of (1) tilt boundaries in (001) built of (100)[001] dislocations, (2) tilt boundaries in (100) associated with (001)[100] dislocations, or (3) twist boundaries in (010) (Figure 10a). Concentration of olivine [010] axes at high angle to the foliation (Figure 9) suggests the existence of (010) twist boundaries. The (100)[001] and (001)[100] slips seem less favorable for the formation of the subgrain boundaries, because of the low shear stress applied on these slip systems for the axial-[010] symmetry. Thus, we attribute the clustering of misorientation axes near [010] to the existence of twist boundaries in (010). In support to the existence of (010) twist boundaries is the presence of subgrain boundaries subparallel to the foliation plane (Figure 5b). The coexistence of misorientation axes near [001] and [100] (FDM-AVBB01, FDM-AVBB06, FDM-AVBB07, and FDM-AVBB08) implies activity of both (010)[100] and (010)[001] slip systems.

Olivine low-angle misorientation axis distributions in the xenoliths with CPO of axial-[100] symmetry are characterized by maxima either oblique (FDM-DB01-X01, FDM-DB02-X13, and FDM-DB03-X01) or parallel (FDM-RN04-X01, FDM-DB02-X01, FDM-DB03-X03, KSP89-181-X01, and FDM-DB04-X03) to [001] and [010] (Figure 9). These misorientation axis distributions suggest operation of a variety of dislocations in the {0kl}

[100] family of slip systems. The existence of [001] misorientations fits with subgrains characterized by tilt boundaries built of (010)[100] dislocations, while [010] misorientations most easily fit with tilt boundaries built of (001)[100] dislocations (Figure 10a). The xenoliths with [010] misorientations are characterized by lack of olivine [100] crystal axes trending parallel to Φ_3, which would indicate (100)[001] slip, as well as lack of [100] crystal axes parallel to Φ_2 that could suggest occurrence of (010) twist boundaries built from [100] and [001] screw dislocations.

The xenolith with the B-type CPO pattern contains misorientation axes that are distributed along a girdle between [001] and [010], with the maximum concentration of axes being parallel to [001]. This distribution of misorientations suggests that subgrain boundaries are built of {0kl}[100] dislocations, with predominant occurrence of tilt boundaries in (100) associated with (010)[100] dislocations.

4.6.2. Spinel

Spinel is characterized by random distribution of crystallographic axes orientations irrespective of fabric anisotropy and geometry. Misorientation analysis of spinel reveals that only few grains have internal misorientation of maximum 6°, which indicates limited intragrain deformation (Figure S2).

4.7. Grain Size and Differential Stress

For viscously deforming rocks, the piezometric relationship that relates the recrystallized grain size to the differential stress follows a power law:

$$D_g = A\sigma^{-n} \tag{4}$$

where D_g is the recrystallized grain size, σ is the differential stress, and A and n are empirically derived constants. We use the calibrations of *Karato et al*. [1980] and *Van der Wal et al*. [1993] to estimate differential stress. Olivine grain sizes generally show continuous, lognormal distributions (Figure 4f). In coarse-grained peridotites with continuous grain size distributions, such as those in the Marie Byrd Land xenoliths, it is difficult to discriminate between recrystallized and relict grains. We determined the geometric mean of the grain size distribution, which can be related to the applied tectonic stress [*Ranalli*, 1984]. We note that this approach may lead to overestimation of the recrystallized grain size and, therefore, underestimation of differential stress. The geometric means of the grain size distributions range from 61 to 2000 μm (Table 1); the average of the geometric means for the whole xenolith suite is 665 μm. The estimated grain sizes correspond to differential stresses of 2–60 MPa (Table 1 and Figure 11).

4.8. Water Content

Xenoliths chosen for FTIR measurement included examples with each of the four different olivine CPO types (Table 2). Olivine H contents vary from below the detection limit (sub-ppm) to 5 ppm H_2O, and coexisting orthopyroxenes have from 34 to 153 ppm H_2O. Olivine in mantle xenoliths is susceptible to diffusive loss of H during emplacement [e.g., *Demouchy et al*., 2006; *Warren and Hauri*, 2014]. Orthopyroxene, on the other hand, has been shown to preserve its pre-emplacement H content with greater fidelity [*Warren and Hauri*, 2014]. We therefore use the equilibrium partition coefficient for H between orthopyroxene and olivine, $D^{opx/ol}$, to determine the pre-emplacement H content of olivine. Experiments show that $D^{opx/ol}$ is strongly dependent upon the Al_2O_3 content of the orthopyroxene [*Hirschmann et al*., 2009]. The analyzed orthopyroxenes have between 3.1 and 4.8 wt % Al_2O_3, from which we estimate that $D^{opx/ol}$ is between 5 and 15 [e.g., *Ardia et al*., 2012], which suggests equilibrium H concentration in olivine of up to 31 ppm H_2O (500 H/10^6 Si) (Table 2).

4.9. Deformation Mechanisms

To assess the dominant deformation mechanism(s) in the Marie Byrd Land xenoliths, we constructed deformation mechanism maps using experimentally derived olivine flow laws. For each xenolith, we constructed the deformation mechanism map based on the estimated deformation conditions (temperature, pressure, and differential stress), assuming a dry lithospheric mantle. In Figure 11, we present deformation mechanism maps constructed for temperature intervals (and corresponding pressures) of 850, 950, and 1050°C. Data from individual samples are plotted on the deformation mechanism map that most closely matches calculated equilibration temperatures. Extrapolation of laboratory flow laws from *Hansen et al*. [2011] to the deformation conditions estimated for the Marie Byrd Land xenoliths indicates that deformation was primarily achieved by dislocation-accommodated grain boundary sliding (Figure 11). Deformation by dislocation-

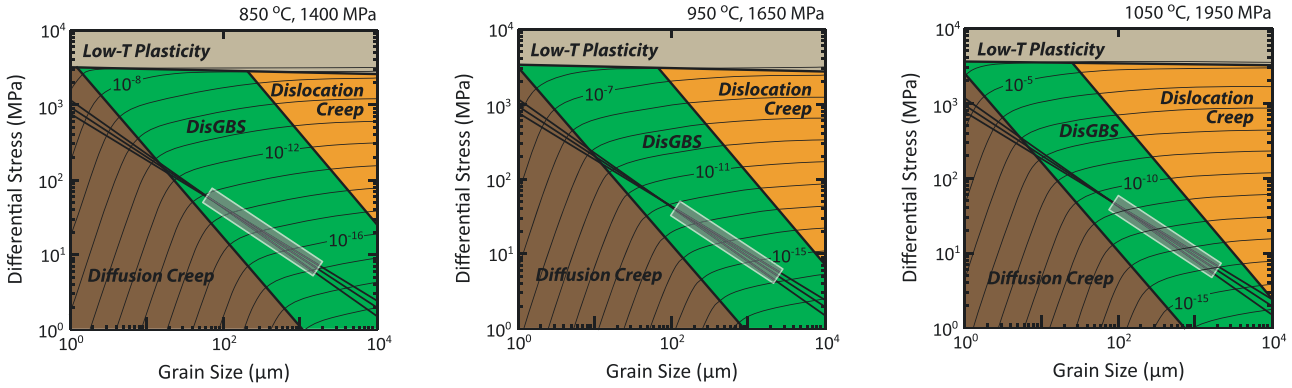

Figure 11. Olivine deformation mechanism maps calculated using four deformation mechanisms, as described in *Warren and Hirth* [2006]: dislocation creep, dislocation-accommodated grain boundary sliding (DisGBS), diffusion creep, and low-temperature plasticity. The deformation mechanism maps have been constructed using the flow laws of *Goetze* [1978], *Evans and Goetze* [1979], *Hirth and Kohlstedt* [2003], and *Hansen et al.* [2011]. The temperature and pressure are chosen based on the estimated deformation conditions in the Marie Byrd Land xenoliths (this study). The maps are constructed at 850, 950, and 1050°C, and data are plotted on the map that most closely matches the calculated equilibration temperature. We use a piezometric line that corresponds to the linear least squares fit to data of *Karato et al.* [1980] and *Van der Wal et al.* [1993], based on *Warren and Hirth* [2006]. Extrapolations of the Hansen et al. flow law predict deformation by dominantly dislocation-accommodated grain boundary sliding. The grey boxes in the maps correspond to the range of geometric means of the grain sizes in the xenoliths for the deformation conditions for which each map has been constructed.

accommodated grain boundary sliding is also consistent with the observed microstructures in the xenolith suite, which are indicative of intragrain deformation and grain boundary sliding (see section 4.1).

5. Discussion

5.1. Significance of Spinel Shape Fabric

The lack of spinel CPO and the limited presence of low-angle misorientations in the spinel grains suggest limited intracrystalline deformation of spinel. We can therefore infer that spinel must have undergone rigid rotation, relative to adjacent olivine and pyroxene grains.

In each xenolith, the spinel shape fabric ellipsoid describes the distribution of orientations of spinel grains. We emphasize that the estimated degree of anisotropy of the spinel shape fabric does not represent the finite strain magnitude quantitatively [*Giorgis and Tikoff*, 2004; *Arbaret et al.*, 2007]. In several xenoliths we observe subparallelism of (1) the Φ_1 axis of the spinel fabric ellipsoid, (2) the long axes of olivine grains measured on the $\Phi_1\Phi_3$ plane of the fabric ellipsoid, and (3) the maxima of [100] or [001] olivine crystal axis distributions (Figure 9; e.g., FDM-AVBB06, FDM-AVBB07, FDM-AVBB08, FDM-DB03-X02, FDM-AVBB05, FDM-DB02-X11, FDM-DB02-X08 FDM-RN02-X01, FDM-DB01-X01, FDM-DB03-X03, and FDM-DB04-X03). We interpret the alignment between these three deformation features as an indication that the 3-D spinel shape fabric may have reached a steady state orientation. The parallelism between 3-D spinel SPO, 2-D olivine SPO, and olivine CPO does not depend on the deformation mechanism; spinel SPO formed by rotation of rigid grains, while olivine SPO and CPO formed by dislocation-accommodated grain boundary sliding.

At high strain, dynamic recrystallization may affect SPO; the long axes of the recrystallized grains acquire a steady state orientation at high angle (40–70°) to the shear plane [e.g., *Herwegh and Handy*, 1998; *Tasaka et al.*, 2016]. Due to limited modification of spinel grain shape by dynamic recrystallization, we can rule out this hypothesis. Experimental and numerical studies demonstrate that in simple shear, a viscous material containing a population of rigid particles (e.g., nonrecrystallized porphyroclasts) develops a steady shape fabric at large strains [*Ildefonse et al.*, 1997]. This shape fabric can be subparallel to the shear plane and shear direction [*Mancktelow et al.*, 2002; *Arbaret et al.*, 2007], as well as to the finite strain ellipsoid [*Bhattacharyya and Hudleston*, 2001; *Bystricky et al.*, 2006]. We can therefore assume that the XRCT-derived spinel SPO can provide a robust reference framework relative to which we can plot and interpret the olivine CPO data.

The geometries of the fabric ellipsoid and finite strain ellipsoid are likely to be similar. In places where finite strain can be studied in detail, it typically conforms well to shape fabric [e.g., *Cloos*, 1947; *Bhattacharyya and Hudleston*, 2001]. Consequently, while the magnitudes of the axes may vary, the overall shape of the fabric ellipsoid should

Table 2. OH Concentrations in Olivine and Orthopyroxene

Xenolith	Olivine CPO Type	Olivine[a] OH Concentrations (wt ppm H_2O)	Orthopyroxene[b] OH Concentrations (wt ppm H_2O)	Pre-Emplacement Olivine OH Concentrations (ppm wt H_2O)	Pre-Emplacement Olivine OH Concentrations (wt $H/10^6$ Si)
FDM-AV01-X01	A	1.31	88	06–18	96–288
FDM-BB01-X01	A	0.00	37	02–07	40–120
FDM-DB03-X01	Axial-[100]	0.29	111	07–22	120–360
FDM-RN03-X01	B	3.27	68	05–14	73–219
FDM-RN04-X01	Axial-[100]	3.40	153	10–31	167–501
FDM-AVBB02	Axial-[010]	2.95	38	03–08	42–125
AD6021-X02	Axial-[010]	0.18	34	02–07	37–111
KSP89-181-X01	Axial-[100]	4.86	–	–	–

[a]Olivine OH concentrations from this study calculated using the calibration of *Withers et al.* [2012].
[b]Orthopyroxene OH concentrations from this study calculated using the calibration of *Bell et al.* [1995].

parallel the finite strain ellipsoid. Deviations from this pattern are expected only in the cases of highly planar markers, highly linear markers, or deformations with large vorticity components [*Giorgis and Tikoff*, 2004]. In the following discussion we assume that spinel shape fabric geometry adequately describes the finite strain geometry.

5.2. Effect of Deformation Conditions

The Marie Byrd Land xenoliths have equilibrated at temperatures ranging from 780 to 1200°C, and assuming a geotherm which satisfies the stability of spinel in all the xenoliths, the corresponding ranges in pressures and depths are 13–23 kbar and 39–72 km, respectively (Figure 7b). The estimated deformation conditions suggest a lithospheric rather than asthenospheric origin for all the xenoliths; the asthenospheric mantle beneath Marie Byrd Land is marked by a seismic low-velocity zone imaged below 80 km depth [*Ritzwoller et al.*, 2001]. Water content and paleopiezometry analysis suggest that the Marie Byrd Land lithospheric mantle is variably hydrated (with olivine H content of up to 500 $H/10^6$Si) and has been deformed under low flow stress (2–60 MPa).

Combining the estimated deformation conditions with the observed olivine CPOs in the Marie Byrd Land xenoliths, we can explore how variations in temperature, pressure, differential stress, and water content are associated with the type of olivine CPO. Plotting our data in differential stress versus temperature/pressure space, we do not observe systematic variation in CPO type relative to temperature and pressure (Figure 12a). There is, however, a tendency of axial-[100] patterns to develop at lower flow stress. To further provide an unbiased discriminator of the relationship between deformation conditions and olivine CPO, we use the BA index. The BA index shows no correlation with equilibration temperature and pressure (Figure 12b). Higher BA index values ($>$0.5), though, are associated with low differential stress (Figure 12c).

We observe a correlation between the BA index and the estimated pre-emplacement OH concentration in olivine; water content increases with the BA index (Figure 12d and Table 2). Olivine in xenoliths with the axial-[010] symmetry is only slightly hydrated ($<$150 $H/10^6$Si), and it becomes moderately hydrated (100–500 $H/10^6$Si) toward the axial-[100] symmetry. In the orthorhombic symmetry, the xenolith with the B-type CPO is characterized by minor water content (73–219 $H/10^6$Si), while the two xenoliths with A-type CPO have minor to modest water content (40–288 $H/10^6$Si).

The development of the A-type olivine CPO in the range of deformation conditions estimated for the Marie Byrd Land xenoliths is in agreement with the results of experimental studies, which show that the A-type CPO typically forms at low stress and low water content [*Carter and Avé Lallemant*, 1970; *Jung and Karato*, 2001; *Katayama et al.*, 2004; *Karato et al.*, 2008]. Particularly, in the low stress levels estimated for the studied xenoliths, the range of water content at which the formation of the A-type CPO is observed can increase up to 300 $H/10^6$Si (Figure 1a) [*Katayama et al.*, 2004], which is in agreement with our observations.

The transition from A-type to axial-[100]-type CPO pattern is predominantly considered to be stress controlled, and the axial-[100] CPO is typically related to high stress and dry conditions (Figure 1a) [*Carter and Avé Lallemant*, 1970; *Katayama et al.*, 2004]. However, decrease of temperature decreases the stress threshold above which the axial-[100] CPO type forms. Xenoliths with the axial-[100] CPO are characterized by low stresses ($<$20 MPa) but span the whole range of the estimated deformation conditions (Figures 12a–12c). This implies that the formation of the axial-[100] CPO at low flow stress is not the result of decreasing deformation temperature.

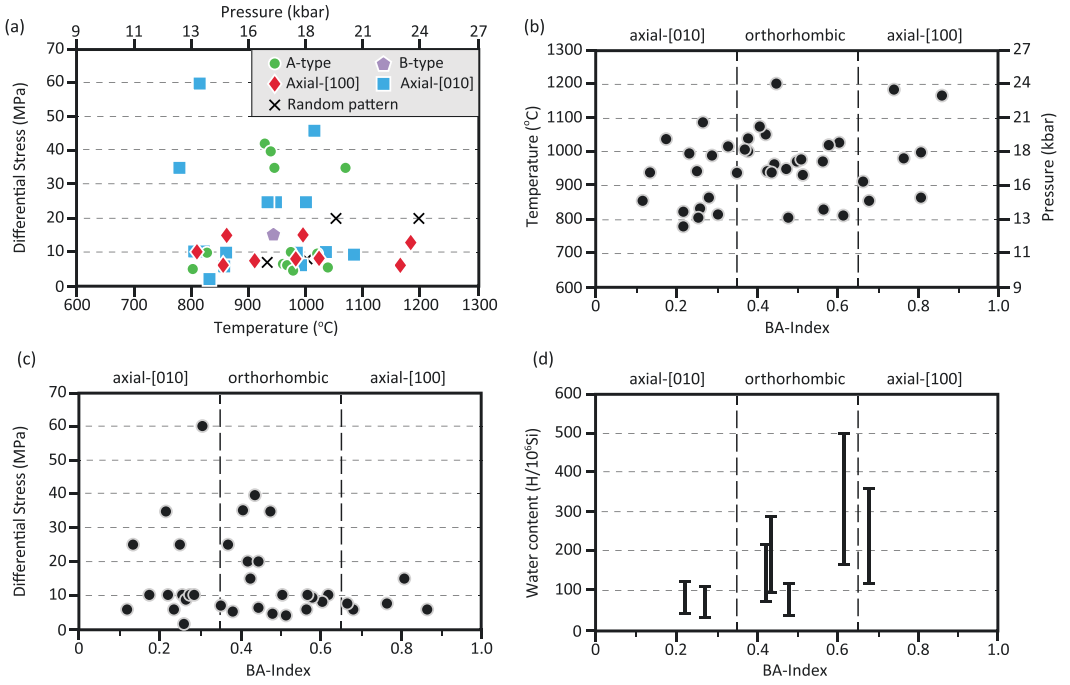

Figure 12. Relationship between deformation conditions and olivine CPO type. (a) Olivine CPO type as a function of differential stress, temperature, and pressure. (b) Olivine CPO type expressed by the BA index, as a function of temperature and pressure. (c) BA index as a function of differential stress. (d) Relationship between BA index and water content. Water content is the estimated range of pre-emplacement OH concentrations in olivine.

High-temperature experiments show development of the axial-[100] CPO type at relatively low stresses and under dry [*Bystricky et al.*, 2000; *Hansen et al.*, 2014] or hydrous [*Demouchy et al.*, 2012] conditions. In the latter study, however, quantification of the intragranular water content of deformed olivine was not possible. Our results support that the axial-[100] CPO may form in low flow stress and moderate water content. Combining the experimental results with observations from naturally deformed rocks [e.g., *Saruwatari et al.*, 2001; *Warren et al.*, 2008; *Webber et al.*, 2010, this study], it becomes evident that the axial-[100] CPO can form in a wide range of deformation conditions, which makes it difficult to assign this CPO type to a specific set of conditions.

Increased activity of the (010)[001] slip system with increased pressure (>30 kbar) [*Couvy et al.*, 2004; *Raterron et al.*, 2012; *Jung et al.*, 2009; *Lee and Jung*, 2015] or water content (>200 H/10^6Si) [*Jung and Karato*, 2001; *Mizukami et al.*, 2004; *Karato et al.*, 2008] may lead to the development of the B-type and the axial-[010] CPOs. Despite the uncertainty included in the determination of the geotherm for the Marie Byrd Land lithospheric mantle, the xenoliths with axial-[010] and B-type CPOs are characterized by equilibration pressures of less than 21 kbar and contain relatively dry olivine. Development of the axial-[010] and B-type CPO patterns at pressures lower than 30 kbar and/or dry conditions has been described both in nature [*Newman et al.*, 1999; *Dijkstra et al.*, 2002; *Hidas et al.*, 2007; *Drury et al.*, 2011; *Précigout and Hirth*, 2014] and experiments [*Avé Lallemant and Carter*, 1970; *Nicolas et al.*, 1973].

Experimental, theoretical, and natural studies have substantiated that changes in deformation conditions induce variations in olivine CPO [e.g., *Carter and Avé Lallemant*, 1970; *Tommasi et al.*, 2000; *Karato et al.*, 2008]. Our data set confirms the development of the A-type CPO under low flow stress, low to moderate water content, and intermediate pressure. However, our results emphasize that the development of the axial-type and B-type CPOs in the Marie Byrd Land xenoliths cannot be solely explained on the basis of variations in deformation conditions.

5.3. Effect of Finite Strain

5.3.1. Strain Magnitude

Strain markers are rare in the mantle, and as a result, the relationship between strain magnitude and olivine CPO is difficult to evaluate in naturally deformed mantle rocks. Strain can affect the CPO asymmetry [*Zhang et*

al., 2000; *Kaminski and Ribe*, 2001; *Warren et al*., 2008; *Webber et al*., 2010], the CPO type [*Boneh and Skemer*, 2014; *Hansen et al*., 2014], as well as the CPO strength [*Tommasi et al*., 2000; *Kaminski and Ribe*, 2001; *Hansen et al*., 2014]. Experimental and numerical simulation studies suggest that CPO strength increases as a function of shear strain [*Bystricky et al*., 2000; *Kaminski and Ribe*, 2001; *Hansen et al*., 2014], in which case it may be possible to use olivine CPO strength to qualitatively describe strain magnitude.

An increase in strain may cause transient development of the axial-[100] type in olivine during CPO evolution from random to A type [*Hansen et al*., 2014]. To explore potential effect of strain magnitude on olivine CPO development for the Marie Byrd Land xenoliths, we plot the BA index against the *J* and *M* indices. Our data show no correlation between CPO symmetry and strength (Figures 13a and 13b). Furthermore, the mean *J* and *M* index values for the A-type ($J = 3.49$, $M = 0.15$) and axial-[100] ($J = 3.48$, $M = 0.18$) CPOs are similar.

To further explore the relationship between strain magnitude and CPO type, we use the spinel shape fabric. The degree of spinel fabric anisotropy does not describe strain magnitude in a quantitative way but can provide qualitative constraints [*Giorgis and Tikoff*, 2004]. We observe no correlation between the BA index and the fabric anisotropy (Figure 13c). Thus, our data provide indirect evidence that the variation in olivine CPO symmetry observed in the Marie Byrd Land xenoliths may not be the result of strain magnitude changes.

5.3.2. Strain Geometry

In addition to fabric anisotropy, we explore the relationship between fabric geometry and CPO symmetry (Figure 14a). The xenoliths with A-type CPO spread over the whole range of fabric ellipsoid geometries; five xenoliths plot in the prolate field, two in the oblate field, and five plot near the neutral ellipsoid shape line. The majority (10 out of 15) of the xenoliths with an axial-[010] symmetry are characterized by fabric ellipsoids with neutral shape to oblate geometries. On the other hand, the majority (six out of eight) of the xenoliths with axial-[100] CPO are associated with prolate spinel fabric ellipsoid geometries. The sample with the B-type CPO pattern has a highly oblate fabric ($T = 0.68$) (Figure 14a). To explore the relationship between fabric geometry and olivine CPO further, we compare the BA index with the shape parameter of the spinel fabric (Figure 14b). The BA index increases with decreasing *T*; there is a transition from axial-[010], to orthorhombic symmetry, and finally to axial-[100] CPO, with an associated change from oblate to prolate fabric geometry (Figure 14b). Assuming correlation between the shape of the fabric and finite strain ellipsoid, our data provide evidence that olivine CPO type depends on finite strain geometry.

In support of this result, laboratory-based studies and numerical simulations demonstrate that different deformation boundary conditions will produce different olivine CPOs. The axial-[010] CPO has largely been produced in axial compression experiments [*Avé Lallemant and Carter*, 1970; *Nicolas et al*., 1973; *Hansen et al*., 2011; *Miyazaki et al*., 2013], which involve flattening strain [*Avé Lallemant and Carter*, 1970; *Nicolas et al*., 1973; *Llana-Fúnez and Rutter*, 2014]. Axial compression of olivine aggregates results in clusters of [010] axes and girdles of [100] axes; girdling of [100] axes comprises the primary distinction between the axial-[010] and A-type CPOs. Olivine CPOs with [100] girdles have also been produced in direct shear experiments [*Zhang et al*., 2000; *Holtzman et al*., 2003; *Hansen et al*., 2014]. Deformation in direct shear experiments is simply shear dominated, but it also includes a component of compression, with the overall deformation being transpressional [*Zhang et al*., 2000; *Holtzman et al*., 2003; *Karato et al*., 2008; *Hansen et al*., 2014]. Transpression generally produces oblate ellipsoids due to flattening strain [e.g., *Fossen and Tikoff*, 1998]. Numerical simulations suggest that axial shortening and transpression result in axial-[010] CPOs, similar to those observed in the Marie Byrd Land xenoliths with oblate fabric geometries [*Wenk et al*., 1991; *Tommasi et al*., 1999].

Numerical simulations also suggest that transtension (constrictional strain) will produce axial-[100] CPOs, similar to those identified in the Marie Byrd Land xenoliths with prolate fabric geometries [*Tommasi et al*., 1999]. Girdling versus clustering of [010] axes comprises the primary distinction between the axial-[100] and A-type CPOs, respectively. In contrast to the results of the numerical models and this work, laboratory-based studies show that the axial-[100] CPO is primarily produced in torsion experiments [*Bystricky et al*., 2000, 2006; *Demouchy et al*., 2012; *Hansen et al*., 2014]. Deformation in torsion experiments approaches simple shear and therefore plane strain.

The A-type CPO has been produced in direct shear and high shear strain torsion experiments under dominant simple shear deformation [*Zhang et al*., 2000; *Hansen et al*., 2014]. Development of the A-type CPO in simple shear is also supported by olivine CPO simulation studies [*Wenk et al*., 1991; *Tommasi et al*., 1999; *Kaminski and Ribe*, 2001]. Our results, however, only partly (5 out of 12 xenoliths) support the correlation between A-type CPO and neutral shape of the fabric ellipsoid.

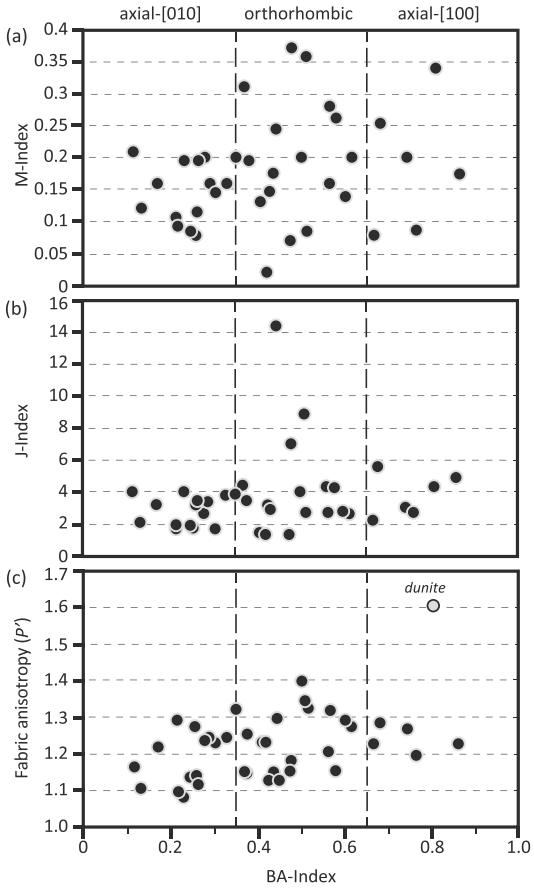

Figure 13. (a and b) Relationship between olivine CPO symmetry (BA index) and strength described by the *M* index (Figure 13a) and *J* index (Figure 13b). (c) Degree of spinel fabric anisotropy versus olivine CPO symmetry.

The presence of only one sample with B-type olivine CPO pattern in the analyzed suite of xenoliths does not allow for definitive predictions concerning the relationship between this CPO and strain geometry. We note, however, that our observations are in agreement with the results of *Lee and Jung* [2015], which also show correlation between the olivine B-type CPO and flattening strain. Furthermore, the B-type CPO is predominantly formed in direct shear experiments [*Jung and Karato*, 2001; *Holtzman et al*., 2003]; samples are subjected to transpressional deformation, which predominantly produces oblate strain ellipsoids.

To summarize, our results emphasize that in the Marie Byrd Land xenoliths, strain geometry controls the development of axial-type olivine CPO patterns (Figure 15). The axial-[010] CPO forms in flattening strain and the axial-[100] CPO in constriction. This relationship is also supported by deformation experiments and numerical simulation studies of CPO evolution.

5.4. Mechanism of Olivine Axial-Type CPO Development

We propose that development of olivine axial-type CPOs in the Marie Byrd Land xenoliths results from the combination of (1) 3-D strain, (2) deformation by dislocation-accommodated grain boundary sliding, and (3) activation of multiple slip systems. The kinematic boundary conditions of deformation control the orientation and shape of the finite strain ellipsoid [*Fossen and Tikoff*, 1998]. The 3-D strain induces changes in the shape of grains. Movement of dislocations along slip planes and sliding along grain boundaries induce shape changes at the grain scale. Concurrent slip along multiple glide planes allows for accommodation of more complex types of noncoaxial deformation [*Tommasi et al*., 1999], while grain boundary sliding relaxes strain compatibility constraints and may facilitate grain rotations [*Tommasi et al*., 2000; *Warren et al*., 2008; *Drury et al*., 2011; *Hansen et al*., 2014; *Précigout and Hirth*, 2014].

Correlation of [100], [001], and [010] olivine crystallographic axes with ε_1, ε_2, and ε_3 strain ellipsoid axes, respectively, has been proposed [*Avé Lallemant and Carter*, 1970; *Nicolas et al*., 1973; *McKenzie*, 1979; *Ribe and Yu*, 1991; *Miyazaki et al*., 2013]. In addition, a fundamental relationship exists between the distributions of the orientations of olivine crystallographic axes in axial-type CPOs and the orientations of axes in the corresponding fabric ellipsoids, i.e., between crystal lattice and grain shape. The [100], [001], and [010] axes show similar distributions in their orientations with Φ_1, Φ_2, and Φ_3 fabric ellipsoid axes, respectively (Figure 15). In flattening strain, the Φ_1 and Φ_2 axes of grains have similar magnitudes and tend to disperse along the foliation plane due to multidirectional stretching occurring on that plane. Similarly, the [100] and [001] olivine crystallographic axes of the axial-[010] CPO, which forms with oblate strain geometries, tend to make girdles along the foliation (Figure 15). Both Φ_3 and [010] cluster parallel to the shortening orientation. In constrictional strain, the Φ_2 and Φ_3 axes of grains have similar magnitudes and tend to disperse on a plane normal to the lineation (Figure 15). Both Φ_1 and [100] cluster parallel to the stretching orientation. The described

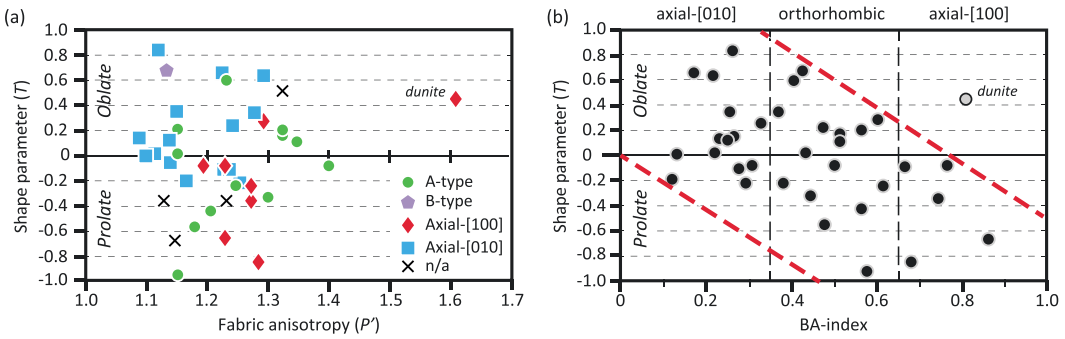

Figure 14. Relationship between fabric geometry and CPO symmetry. (a) Spinel fabric anisotropy versus geometry. Data are coded based on their olivine CPO type. (b) Spinel fabric geometry versus olivine CPO symmetry, expressed by the BA index. Red lines describe the existing trend between fabric geometry and BA index data; the value of the BA index increases with transition from oblate to prolate fabric geometries.

relationship between the crystallographic and grain shape axes implies that their orientation is controlled by the strain geometry and, therefore, by the kinematic boundary conditions imposed by the deformation.

The grain-scale processes that produce the girdled patterns in axial-type CPOs in the Marie Byrd Land xenoliths are as follows. Flattening strain involves multidirectional stretching along the foliation plane. This stretching can be accommodated by dislocation glide toward a range of directions within the foliation plane [*Tommasi et al.*, 1999]. In the xenoliths with axial-[010] CPO, intracrystalline deformation exhibited by subgrain boundary formation is accommodated by {0kl}[100] and (010)[001] slips. Numerical simulations of *Tommasi et al.* [2000] show that in axial shortening, relaxation of strain compatibility constraints (e.g., due to grain boundary sliding) may increase the activity of the otherwise "hard" (010)[001] slip system. The combination of microstructures, misorientation axes analysis, and CPO data suggests the existence of twist boundaries in (010), which involve rotation along (010) planes (Figure 10b) [*Lloyd et al.*, 1997]. Such rotation may induce spreading of [100] and [001] axes within the foliation plane and produce more girdled patterns. Development of the axial-[010] CPO in dislocation-accommodated grain boundary sliding with dominant activity of (010)[100] is also reported by *Précigout and Hirth* [2014]; the axial-[010] CPO is considered transitional between the A- and B-type CPOs, with the alignment of [001] axes parallel to Φ_1 being the result of rigid grain rotations guided by the olivine crystal habit.

In the xenoliths with axial-[100] CPO, olivine grains contain subgrain boundaries composed of dislocations in the {0kl}[100] family of slip systems and (001)[100] dislocations. In agreement with the results of previous studies, development of [010] and [001] girdles in the Marie Byrd Land xenoliths seems to result from the activation of multiple glide systems [*Tommasi et al.*, 1999, 2000; *Warren et al.*, 2008; *Demouchy et al.*, 2012]. Grain boundary sliding promotes multislip on {0kl}[100] systems and/or combined operation of (010)[100] and (001)[100] slip systems, which may lead to the formation of [010] and [001] girdles at high angle to the lineation [*Warren et al.*, 2008].

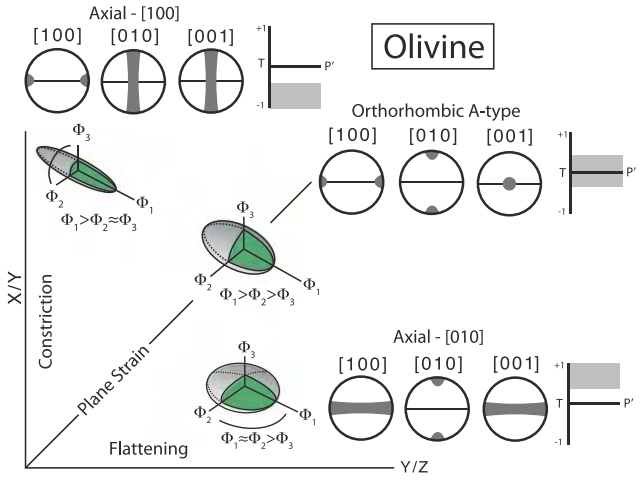

Figure 15. Relationship between finite strain geometry and olivine CPO symmetry.

5.5. Implications for the Interpretation of Olivine CPO

Several experimental and numerical simulation studies have substantiated the role of deformation

conditions, melt, and strain magnitude on the development and evolution of olivine CPO [*Avé Lallemant and Carter*, 1970; *Carter and Avé Lallemant*, 1970; *Wenk et al*., 1991; *Tommasi et al*., 1999, 2000; *Jung and Karato*, 2001; *Holtzman et al*., 2003; *Couvy et al*., 2004; *Katayama et al*., 2004; *Karato et al*., 2008; *Demouchy et al*., 2012; *Raterron et al*., 2012; *Hansen et al*., 2014]. In the present study, we demonstrate the role of finite strain geometry as a fundamental parameter affecting olivine CPO and particularly controlling the development of the axial-type CPOs. We should note that the relationship between strain geometry and olivine CPO was initially described in early compression experiments [*Avé Lallemant and Carter*, 1970; *Nicolas et al*., 1973] and later numerical studies [*McKenzie*, 1979; *Ribe and Yu*, 1991; *Wenk et al*., 1991; *Tommasi et al*., 1999, 2000]; however, little attention has been given to this relationship since then. Additionally, correlation between finite strain geometry and clinopyroxene CPO has been described in mantle xenolith studies [*Helmstaedt et al*., 1972; *Ulrich and Mainprice*, 2005]. Thus, our results emphasize that both deformation conditions and finite strain geometry may affect mantle texture, which makes it difficult to deduce the effect of each parameter separately.

Despite the complexities inherent in the interpretation of CPO patterns, particularly in naturally deformed rocks that may have followed complex deformation histories, three lines of evidence suggest that our results from the Marie Byrd Land xenoliths can be of broad significance for upper mantle studies. First, the importance of dislocation-accommodated grain boundary sliding, which contributes to the development of the axial-type CPOs [*Tommasi et al*., 2000; *Warren et al*., 2008; *Hansen et al*., 2014; *Précigout and Hirth*, 2014], is increasingly recognized. Extrapolation of experimental flow laws shows that dislocation-accommodated grain boundary sliding may contribute to the deformation over a wide range of conditions in a dry upper mantle [*Hansen et al*., 2011]. Second, polyphase materials such as the Marie Byrd Land xenoliths (predominantly lherzolites and harzburgites) are the norm rather than the exception in nature. Grain and phase boundary sliding is facilitated by the coexistence of olivine and pyroxene [*Sundberg and Cooper*, 2008; *Newman et al*., 1999]. Third, there are a large number of studies reporting axial-type CPOs in naturally deformed rocks from a range of tectonic settings [e.g., *Saruwatari et al*., 2001; *Dijkstra et al*., 2002; *Vauchez et al*., 2005; *Hidas et al*., 2007; *Warren et al*., 2008; *Webber et al*., 2010; *Précigout and Hirth*, 2014]. We note that the presence of melt along grain boundaries relaxes strain compatibility constraints and may promote diffusion creep and grain boundary sliding, facilitating the development of axial-type CPOs [e.g., *Holtzman et al*., 2003; *Higgie and Tommasi*, 2012]. Assuming that olivine CPO contains information about strain geometry, the occurrence of axial-type CPO patterns implies that deviation of upper mantle deformation from simple shear may not be an uncommon phenomenon. Furthermore, since olivine CPO is the major contributor to lithospheric seismic anisotropy [*Christensen*, 1984; *Ben Ismail and Mainprice*, 1998; *Tommasi et al*., 1999; *Karato et al*., 2008; *Précigout and Almqvist*, 2014], there is great potential for using seismic anisotropy to map variations in finite strain geometry in the lithosphere and to interrogate new geodynamic interpretations with a revised view of the development of olivine CPO.

6. Conclusions

Using X-ray computed tomography, we determine the spinel fabric ellipsoid in a suite of spinel peridotite xenoliths from Marie Byrd Land, West Antarctica. The xenoliths show a range of fabric ellipsoid geometries (oblate, neutral shape, and prolate) and are characterized by a variety of olivine CPO types (A type, axial-[010], axial-[100], and B type). For the range of temperature, pressure, differential stress, and water content conditions estimated in the xenoliths, the development of girdled olivine CPO patterns is predominantly controlled by the geometry of the finite strain ellipsoid rather than the deformation conditions. We therefore establish for the first time in naturally deformed peridotites a relationship between finite strain geometry and olivine CPO symmetry. The axial-[010] and axial-[100] patterns form by flattening and constrictional strain, respectively. Importantly, our observations suggest that mantle deformation may deviate from simple shear. Our results emphasize that future studies of laboratory and naturally deformed rocks should incorporate the role of finite strain geometry as a possible cause of textural transitions in the mantle. Olivine texture and seismic anisotropy could potentially be used to map 3-D strain variations in the upper mantle.

Acknowledgments

We thank the United States Polar Rock Repository, Christine Siddoway, and Kurt Panter for providing us with xenolith samples. We thank John Fournelle (UW-Madison) for his advice and assistance with the microprobe analyses, Brian Hess (UW-Madison) for the production of high-quality thin sections used in EBSD analysis, and Zach Michels for his assistance with MTEX. Marc Hirschmann and Jed Mosenfelder (University Minnesota) kindly provided access to FTIR facilities. The quality of this work benefited greatly from constructive comments from reviewers Lars Hansen and Jacques Précigout, as well as from the comments of Editors Michael Walter and Stephen Parman. Finally, we thank Basil Tikoff, Julie Newman, Martyn Drury, and members of the structure and tectonics groups at Boston College and UW-Madison for their insightful discussions. The EPMA data used are listed in Table S3. Requests for XRCT and EBSD data sets can be made by contacting the corresponding author. This research was supported by NSF-ANT 1246320 grant to S.C. Kruckenberg and NSERC discovery grant to A.C. Withers.

References

Accardo, N. J., D. A. Wiens, S. Hernandez, R. C. Aster, A. Nyblade, A. Huerta, S. Anandakrishnan, T. Wilson, D. S. Heeszel, and I. W. D. Dalziel (2014), Upper mantle seismic anisotropy beneath the West Antarctic Rift System and surrounding region from shear wave splitting analysis, *Geophys. J. Int.*, *198*, 414–429, doi:10.1093/gji/ggu117.

Arai, S. (1994), Characterization of spinel peridotites by olivine-spinel compositional relationships: Review and interpretation, *Chem. Geol.*, *113*, 191–204, doi:10.1016/0009-2541(94)90066-3.

Arbaret, L., M. Bystricky, and R. Champallier (2007), Microstructures and rheology of hydrous synthetic magmatic suspensions deformed in torsion at high pressure, *J. Geophys. Res.*, *112*, B10208, doi:10.1029/2006JB004856.

Ardia, P., M. M. Hirschmann, A. C. Withers, and T. J. Tenner (2012), H_2O storage capacity of olivine at 5–8 GPa and consequences for dehydration partial melting of the upper mantle, *Earth Planet. Sci. Lett.*, *345–348*, 104–116, doi:10.1016/j.epsl.2012.05.038.

Armstrong, J. T. (1988), Quantitative analysis of silicate and oxide materials: Comparison of Monte Carlo, ZaF, an φ(pz) procedures, in *Proceedings of the 23rd Annual Conference of the Microbeam Analysis Society*, edited by D. E. Newbury, pp. 239–246, San Francisco Press, San Francisco, Calif.

Ashby, M. F., and R. A. Verrall (1973), Diffusion accommodated flow and superplasticity, *Acta Metall.*, *21*, 149–163, doi:10.1016/0001-6160(73)90057-6.

Asimow, P. D., L. C. Stein, J. L. Mosenfelder, and G. R. Rossman (2006), Quantitative polarized FTIR analysis of trace OH in populations of randomly oriented mineral grains, *Am. Mineral.*, *91*, 278–284, doi:10.2138/am.2006.1937.

Avé Lallemant, H. G., and N. L. Carter (1970), Syntectonic recrystallization of olivine and modes of flow in the upper mantle, *Geol. Soc. Am. Bull.*, *81*, 2203–2220, doi:10.1130/0016-7606(1970)81[2203:SROOAM]2.0.CO;2.

Bachmann, F., R. Hielscher, and H. Schaeben (2010), Texture analysis with MTEX-free and open source software toolbox, *Diffus. Defect Data, Part B*, *160*, 63–68.

Bachmann, F., R. Hielscher, and H. Schaeben (2011), Grain detection from 2d and 3d EBSD data—Specification of the MTEX algorithm, *Ultramicroscopy*, *111*, 1720–1733.

Bai, Q., S. J. Mackwell, and D. L. Kohlstedt (1991), High-temperature creep of olivine single crystals: 1. Mechanical results for buffered samples, *J. Geophys. Res.*, *96*, 2441–2463, doi:10.1029/90JB01723.

Ballhaus, C., R. F. Berry, and D. H. Green (1991), High pressure experimental calibration of olivine-orthopyroxene-spinel oxygen geobarometer: Implications for the oxidation state of the upper mantle, *Contrib. Mineral. Petrol.*, *107*, 27–40, doi:10.1007/BF00311183.

Bell, D. R., P. D. Ihinger, and G. R. Rossman (1995), Quantitative analysis of trace OH in garnet and pyroxenes, *Am. Mineral.*, *80*, 465–474.

Ben Ismail, W., and D. Mainprice (1998), An olivine fabric database: An overview of upper mantle fabrics and seismic anisotropy, *Tectonophysics*, *296*, 145–158, doi:10.1016/S0040-1951(98)00141-3.

Berg, J. H., R. J. Moscati, and D. L. Herz (1989), A petrologic geotherm from a continental rift in Antarctica, *Earth Planet. Sci. Lett.*, *93*, 98–108, doi:10.1016/0012-821X(89)90187-8.

Bertrand, P., and J.-C. C. Mercier (1985), The mutual solubility of coexisting ortho- and clinopyroxene: Toward an absolute geothermometer for the natural system?, *Earth Planet. Sci. Lett.*, *76*, 109–122, doi:10.1016/0012-821X(85)90152-9.

Bhattacharyya, P., and P. J. Hudleston (2001), Strain in ductile shear zones in the Caledonides of northern Sweden: A three-dimensional puzzle, *J. Struct. Geol.*, *23*, 1549–1565, doi:10.1016/S0191-8141(01)00020-7.

Boneh, Y., and P. Skemer (2014), The effect of deformation history on the evolution of olivine CPO, *Earth Planet. Sci. Lett.*, *406*, 213–222, doi:10.1016/j.epsl.2014.09.018.

Brey, G. P., and T. Köhler (1990), Geothermobarometry in four-phase lherzolites: II. New thermobarometers and practical assessment of existing thermobarometry, *J. Petrol.*, *31*, 1352–1378, doi:10.1093/petrology/31.6.1353.

Bunge, H. J. (1982), *Texture Analysis in Materials Science*, Butterworths, Boston, Mass.

Bystricky, M., K. Kunze, L. Burlini, and J.-P. Burg (2000), High shear strain of olivine aggregates: Rheological and seismic consequences, *Science*, *290*, 1564–1567, doi:10.1126/science.290.5496.1564.

Bystricky, M., F. Heidelbach, and S. Mackwell (2006), Large-strain deformation and strain partitioning in polyphase rocks: Dislocation creep of olivine-magnesiowüstite aggregates, *Tectonophysics*, *427*, 115–132, doi:10.1016/j.tecto.2006.05.025.

Carter, N. L., and H. G. Avé Lallemant (1970), High temperature deformation of dunite and peridotite, *Geol. Soc. Am. Bull.*, *81*, 2181–2202, doi:10.1130/0016-7606(1970)81[2181:HTFODA]2.0.CO;2.

Chaput, J., R. C. Aster, A. Huerta, X. Sun, A. Lloyd, D. Wiens, A. Nyblade, S. Anandakrishnan, J. P. Winberry, and T. Wilson (2014), The crustal thickness of West Antarctica, *J. Geophys. Res. Solid Earth*, *119*, 378–395, doi:10.1002/2013JB010642.

Christensen, N. I. (1984), The magnitude, symmetry and origin of upper mantle anisotropy based on fabric analyses of ultramafic tectonites, *Geophys. J. R. Astron. Soc.*, *76*, 89–111, doi:10.1111/j.1365-246X.1984.tb05025.x.

Cloos, E. (1947), Oolite deformation in the South Mountain fold, Maryland, *Geol. Soc. Bull.*, *58*, 843–918.

Couvy, H., D. J. Frost, F. Heidelbach, K. Nyilas, T. Ungar, S. Mackwell, and P. Cordier (2004), Shear deformation experiments of forsterite at 11 GPa-1400°C in the multianvil apparatus, *Eur. J. Mineral.*, *16*, 877–889, doi:10.1127/0935-1221/2004/0016-0877.

De Kloe, R. (2001), Deformation mechanisms and melt nano-structures in experimentally deformed olivine-orthopyroxene rocks with low melt fractions: An electron microscopy study, PhD thesis, 173 pp., Utrecht Univ.

Demouchy, S., S. D. Jacobsen, F. Gaillard, and C. R. Stern (2006), Rapid magma ascent recorded by water diffusion profiles in mantle olivine, *Geology*, *34*, 429–432, doi:10.1130/G22386.1.

Demouchy, S., A. Tommasi, F. Barou, D. Mainprice, and P. Cordier (2012), Deformation of olivine in torsion under hydrous conditions, *Phys. Earth Planet. Inter.*, *202–203*, 57–70, doi:10.1016/j.pepi.2012.05.001.

Dijkstra, A. H., M. R. Drury, and R. M. Frijhoff (2002), Microstructures and lattice fabrics in the Hilti mantle section (Oman Ophiolite): Evidence for shear localization and melt weakening in the crust-mantle transition zone?, *J. Geophys. Res.*, *107*(B11), 2270, doi:10.1029/2001JB000458.

Drury, M. R., and F. J. Humphreys (1988), Microstructural shear criteria associated with grain boundary sliding during ductile deformation, *J. Struct. Geol.*, *10*, 83–89, doi:10.1016/0191-8141(88)90130-7.

Drury, M. R., and J. L. Urai (1990), Deformation-related recrystallisation processes, *Tectonophysics*, *172*, 235–253, doi:10.1016/0040-1951(90)90033-5.

Drury, M. R., H. G. Avé Lallemant, G. M. Pennock, and L. N. Palasse (2011), Crystal preferred orientation in peridotite ultramylonites deformed by grain size sensitive creep, Étang de Lers, Pyrenees, France, *J. Struct. Geol.*, *33*, 1776–1789, doi:10.1016/j.jsg.2011.10.002.

Durham, W. B., and G. Goetze (1977), Plastic flow of oriented single crystals of olivine: 1. Mechanical data, *J. Geophys. Res.*, *82*, 5737–5753, doi:10.1029/JB082i036p05737.

Evans, B., and C. Goetze (1979), The temperature variation of hardness of olivine and its implication for polycrystalline yield stress, *J. Geophys. Res.*, *84*, 5505–5524, doi:10.1029/JB084iB10p05505.

Ferraccioli, F., E. Bozzo, and D. Damaske (2002), Aeromagnetic signatures over western Marie Byrd Land provide insight into magmatic arc basement, mafic magmatism and structure of the eastern Ross Sea rift flank, *Tectonophysics*, *347*, 139–165, doi:10.1016/S0040-1951(01)00242-6.

Finn, C. A., R. D. Müller, and K. S. Panter (2005), A Cenozoic diffuse alkaline magmatic province (DAMP) in the southwest Pacific without rift or plume origin, *Geochem. Geophys. Geosyst.*, *6*, Q02005, doi:10.1029/2004GC000723.

Fossen, H., and B. Tikoff (1998), Extended models of transpression and transtension, and application to tectonic settings, in *Continental Traspressional and Transtensional Tectonics*, *Geol. Soc. Spec. Publ.*, 135, 15–33, doi:10.1144/GSL.SP.1998.135.01.02.

Gaffney, A. M., and C. S. Siddoway (2007), Heterogeneous sources for Pleistocene lavas of Marie Byrd Land, Antarctica: New data from the SW Pacific diffuse alkaline magmatic province, *U.S. Geol. Surv. Open-File Rep. 07-1047,* Extended Abstract 063.

Giorgis, S., and B. Tikoff (2004), Constraints on kinematics and strain from feldspar porphyroclast populations, in *Flow Processes in Faults and Shear Zones*, edited by G. I. Alsop et al., *Geol. Soc. Spec. Publ.*, 265–285, doi:10.1144/GSL.SP.2004.224.01.17.

Goetze, C. (1978), The mechanisms of creep in olivine, *Philos. Trans. R. Soc. London A*, *288*, 99–119.

Hansen, L. N., M. E. Zimmerman, and D. L. Kohlstedt (2011), Grain boundary sliding in San Carlos olivine: Flow law parameters and crystallographic-preferred orientation, *J. Geophys. Res.*, *116*, B08201, doi:10.1029/2011JB008220.

Hansen, L. N., M. E. Zimmerman, and D. L. Kohlstedt (2014), Protracted fabric evolution in olivine: Implications for the relationship among strain, crystallographic fabric, and seismic anisotropy, *Earth Planet. Sci. Lett.*, *387*, 157–168, doi:10.1016/j.epsl.2013.11.009.

Helmstaedt, H., O. L. Anderson, and A. T. Gavasci (1972), Petrofabric studies of eclogite, spinel-websterite, and spinel-lherzolite xenoliths from kimberlite-bearing breccia pipes in southeastern Utah and northeastern Arizona, *J. Geophys. Res.*, *77*, 4350–4365, doi:10.1029/JB077i023p04350.

Herwegh, M., and M. Handy (1998), The origin of shape preferred orientation in mylonite: Inferences from in-situ experiments on polycrystalline norcamphor, *J. Struct. Geol.*, *20*, 681–694, doi:10.1016/S0191-8141(98)00011-X.

Hidas, K., G. Falusa, C. Szabó, P. J. Szabó, I. Kovács, and T. Földes (2007), Geodynamic implications of flattened tabular equigranular textured peridotites from the Bakony-Balaton Highland Volcanic Field (Western Hungary), *J. Geodyn.*, *43*, 484–503, doi:10.1016/j.jog.2006.10.007.

Higgie, K., and A. Tommasi (2012), Feedbacks between deformation and melt distribution in the crust-mantle transition zone of the Oman ophiolite, *Earth Planet. Sci. Lett.*, *359–360*, 61–72, doi:10.1016/j.epsl.2012.10.003.

Hirschmann, M. M., T. J. Tenner, C. Aubaud, and A. C. Withers (2009) Dehydration melting of nominally anhydrous mantle: The primacy of partitioning, *Phys. Earth Planet. Inter.*, *176*, 54–68, doi:10.1016/j.pepi.2009.04.001.

Hirth, G., and D. Kohlstedt (2003), Rheology of the upper mantle and the mantle wedge: A view from the experimentalists, in *The Subduction Factory*, *Geophys. Monogr.*, vol. 138, edited by J. Eiler, pp. 83–105 , AGU, Washington, D. C.

Holtzman, B. K., D. L. Kohlstedt, M. E. Zimmerman, F. Heidelbach, T. Hiraga, and J. Hustoft (2003), Melt segregation and strain partitioning: Implications for seismic anisotropy and mantle flow, *Science*, *301*, 1227–1230, doi:10.1126/science.1087132.

Hossack, J. (1968), Pebble deformation and thrusting in the Bygdin Area (Norway), *Tectonophysics*, *5*, 315–339, doi:10.1016/0040-1951(68)90035-8.

Ildefonse, B., L. Arbaret, and H. Diot (1997), Rigid particles in simple shear flow: Is their preferred orientation periodic or steady state?, in *Granites: From Segregation of Melt to Emplacement Fabrics*, edited by J. L. Bouchez, D. H. W. Hutton, and W. E. Stephens, pp. 177–185, Kluwer Acad., Dordrecht, Netherlands.

Jelínek, V. (1981), Characterization of the magnetic fabrics of rocks, *Tectonophysics*, *79*, T63–T67, doi:10.1016/0040-1951(81)90110-4.

Jung, H., and S. Karato (2001), Water-induced fabric transitions in olivine, *Science*, *293*, 1460–1463, doi:10.1126/science.1062235.

Jung, H., W. Mo, and H. W. Green (2009), Upper mantle seismic anisotropy resulting from pressure-induced slip transition in olivine, *Nat. Geosci.*, *2*, 73–77, doi:10.1038/NGEO389.

Kaminski, E., and N. M. Ribe (2001), A kinematic model for recrystallization and texture development in olivine polycrystals, *Earth Planet. Sci. Lett.*, *189*, 253–267, doi:10.1016/S0012-821X(01)00356-9.

Karato, S., H. Jung, I. Katayama, and P. A. Skemer (2008), Geodynamic significance of seismic anisotropy of the upper mantle: New insights from laboratory studies, *Annu. Rev. Earth Planet. Sci.*, *36*, 59–95, doi:10.1146/annurev.earth.36.031207.124120.

Karato, S.-I., M. Toriumi, and T. Fuji (1980), Dynamic recrystallization of olivine single crystals during high-temperature creep, *Geophys. Res. Lett.*, *7*, 649–652, doi:10.1029/GL007i009p00649.

Katayama, I., and J. Korenaga (2011), Is the African cratonic lithosphere wet or dry?, in *Volcanism and Evolution of the African Lithosphere*, edited by L. Beccaluva, G. Bianchini, and M. Wilson, *Geol. Soc. Am. Spec. Pap.*, *478*, 249–256, doi:10.1130/2011.2478(13).

Katayama, I., H. Jung, and S. I. Karato (2004), New type of olivine fabric from deformation experiments at modest water content and low stress, *Geology*, *32*, 1045–1048, doi:10.1130/G20805.1.

Ketcham, R. A. (2005a), Computational methods for quantitative analysis of three-dimensional features in geological specimens, *Geosphere*, *1*, 32–41, doi:10.1130/GES00001.1.

Ketcham, R. A. (2005b), Three-dimensional grain fabric measurements using high-resolution X-ray computed tomography, *J. Struct. Geol.*, *27*, 1217–1228, doi:10.1016/j.jsg.2005.02.006.

Ketcham, R. A., and T. Ryan (2004), Quantification and visualization of anisotropy in trabecular bone, *J. Microsc.*, *213*, 158–171, doi:10.1111/j.1365-2818.2004.01277.x.

Kruckenberg, S. C., E. C. Ferré, C. Teyssier, O. Vanderhaeghe, D. L. Whitney, N. C. A. Seaton, and J. A. Skord (2010), Viscoplastic flow in migmatites deduced from fabric anisotropy: An example from the Naxos dome, Greece, *J. Geophys. Res.*, *115*, B09401, doi:10.1029/2009JB007012.

Launeau, P., and P. -Y. F. Robin (1996), Fabric analysis using the intercept method, *Tectonophysics*, *267*, 91–119, doi:10.1016/S0040-1951(96)00091-1.

Law, R. D., R. J. Knipe, and H. Dayan (1984), Strain path partitioning within thrust sheets: Microstructural and petrofabric evidence from the Moine Thrust zone at Loch Eriboll, NW Scotland, *J. Struct. Geol.*, *6*, 477–497, doi:10.1016/0191-8141(84)90060-9.

Lee, J., and H. Jung (2015), Lattice-preferred orientation of olivine found in diamond-bearing garnet peridotites in Finsch, South Africa and implications for seismic anisotropy, *J. Struct. Geol.*, *70*, 12–22, doi:10.1016/j.jsg.2014.10.015.

Lister, G. S., and B. E. Hobbs (1980), The simulation of fabric development during plastic deformation and its application to quartzite: The influence of deformation history, *J. Struct. Geol.*, *2*, 355–371, doi:10.1016/0191-8141(80)90023-1.

Llana-Fúnez, S., and E. H. Rutter (2014), Effect of strain geometry on the petrophysical properties of plastically deformed aggregates: Experiments on Solnhofen limestone, in *Deformation Structures and Processes Within the Continental Crust*, edited by S. Llana-Fúnez, A. Marcos, and F. Bastida, *Geol. Soc. London Spec. Publ.*, pp. 167–187, doi:10.1144/SP394.12.

Lloyd, A., D. A. Wiens, A. Nyblade, S. Anandakrishnan, R. C. Aster, A. D. Huerta, T. J. Wilson, I. W. D. Dalziel, P. J. Shore, and D. Zhao (2015), A seismic transect across West Antarctica: Evidence for mantle thermal anomalies beneath the Bentley Subglacial Trench and the Marie Byrd Land Dome, *J. Geophys. Res. Solid Earth*, *120*, 8439–8460, doi:10.1002/2015JB012455.

Lloyd, G. E., A. B. Farmer, and D. Mainprice (1997), Misorientation analysis and the formation and orientation of subgrain and grain boundaries, *Tectonophysics*, *279*, 55–78, doi:10.1016/S0040-1951(97)00115-7.

Lloyd, G. E., R. H. W. Butler, M. Casey, D. J. Tatham, and D. Mainprice (2011), Constraints on the seismic properties of the middle and lower continental crust, in *Deformation Mechanisms, Rheology and Tectonics: Microstructures, Mechanics and Anisotropy*, edited by D. J. Prior, E. H. Rutter, and D. J. Tatham, *Geol. Soc. London Spec. Publ.*, pp. 7–32, doi:10.1144/SP360.2.

Mainprice, D., R. Hielscher, and H. Schaeben (2011), Calculating anisotropic physical properties from texture data using the MTEX open-source package, in *Deformation Mechanisms, Rheology and Tectonics: Micro-structures, Mechanics and Anisotropy*, edited by D. J. Prior, E. H. Rutter, and D. J. Tatham, *Geol. Soc. London, Spec. Publ.*, *360*, 175–192, doi:10.1144/SP360.10.

Mainprice, D., F. Bachmann, R. Hielscher, and H. Schaeben (2014), Descriptive tools for the analysis of texture projects with large datasets using MTEX: Strength, symmetry and components, in *Rock Deformation From Field, Experiments and Theory: A Volume in Honour of Ernie Rutter*, edited by D. R. Faulkner, E. Mariani, and J. Mecklenburgh, *Geol. Soc. London, Spec. Publ.*, *409*, 223–249, doi:10.1144/SP409.8.

Mancktelow, N. S., L. Arbaret, and G. Pennacchioni (2002), Experimental observations on the effect of interface slip on rotation and stabilisation of rigid particles in simple shear and a comparison with natural mylonites, *J. Struct. Geol.*, *24*, 567–585, doi:10.1016/S0191-8141(01)00084-0.

McFadden, R. R., C. S. Siddoway, C. Teyssier, and C. M. Fanning (2010), Cretaceous oblique extensional deformation and magma accumulation in the Fosdick Mountains migmatite-cored gneiss dome, West Antarctica, *Tectonics*, *29*, TC4022, doi:10.1029/2009TC002492.

McKenzie, D. P. (1979), Finite deformation during fluid flow, *Geophys. J. R. Astron. Soc.*, *58*, 689–715, doi:10.1111/j.1365-246X.1979.tb04803.x.

Medaris, L. G., Jr., L. Ackerman, E. Jelínek, and T. Magna (2015), Depletion, cryptic metasomatism, and modal metasomatism of central European lithospheric mantle: Evidence from elemental and Li isotope compositions of spinel peridotite xenoliths, Kozákov volcano, Czech Republic, *Int. J. Earth Sci.*, *104*, 1925–1956, doi:10.1007/s00531-014-1065-y.

Miyazaki, T., K. Sueyoshi, and T. Hiraga (2013), Olivine crystals align during diffusion creep of Earth's upper mantle, *Nature*, *502*, 321–326, doi:10.1038/nature12570.

Mizukami, T., S. R. Wallis, and J. Yamamoto (2004), Natural examples of olivine lattice preferred orientation patterns with a flow-normal *a*-axis maximum, *Nature*, *427*, 432–436, doi:10.1038/nature02179.

Mosenfelder, J. D., and G. R. Rossman (2013), Analysis of hydrogen and fluorine in pyroxenes by SIMS and FTIR: Part 1. Orthopyroxene, *Am. Mineral.*, *98*, 1026–1041, doi:10.2138/am.2013.4413.

Nadai, A. (1963), *Theory of Flow and Fracture of Solids*, pp. 705, McGraw-Hill, New York.

Newman, J., W. M. Lamb, M. R. Drury, and R. L. M. Vissers (1999), Deformation processes in a peridotite shear zone: Reaction-softening by an H_2O-deficient, continuous net transfer reaction, *Tectonophysics*, *303*, 193–222, doi:10.1016/S0040-1951(98)00259-5.

Nicolas, A., F. Boudier, and A. M. Boullier (1973), Mechanisms of flow in naturally and experimentally deformed peridotites, *Am. J. Sci.*, *273*, 853–876, doi:10.2475/ajs.273.10.853.

Odgaard, A., J. Kabel, B. van Rietbergen, M. Dalstra, and R. Huiskes (1997), Fabric and elastic principal directions of cancellous bone are closely related, *J. Biomech.*, *30*, 487–495, doi:10.1016/S0021-9290(96)00177-7.

O'Neill, H. S. T. C. (1981), The transition between spinel lherzolite and garnet lherzolite, and its use as a geobarometer, *Contrib. Mineral. Petrol.*, *77*, 185–194, doi:10.1007/BF00636522.

Précigout, J., and B. S. G. Almqvist (2014), The Ronda peridotite (Spain): A natural template for seismic anisotropy in subduction wedges, *Geophys. Res. Lett.*, *41*, 8752–8758, doi:10.1002/2014GL062547.

Précigout, J., and G. Hirth (2014), B-type olivine fabric induced by grain boundary sliding, *Earth Planet. Sci. Lett.*, *395*, 231–240, doi:10.1016/j.epsl.2014.03.052.

Prior, D. J., et al. (1999), The application of electron backscatter diffraction and orientation contrast imaging in the SEM to textural problems in rocks, *Am. Mineral.*, *84*, 1741–1759.

Ranalli, G. (1984), Grain size distribution and flow stress in tectonites, *J. Struct. Geol.*, *6*, 443–447, doi:10.1016/0191-8141(84)90046-4.

Raterron, P., J. Girard, and J. Chen (2012), Activities of olivine slip systems in the upper mantle, *Phys. Earth Planet. Inter.*, *200*, 105–112, doi:10.1016/j.pepi.2012.04.006.

Ree, J. H. (1994), Grain boundary sliding and development of grain boundary openings in experimentally deformed octachloropropane, *J. Struct. Geol.*, *16*, 403–418, doi:10.1016/0191-8141(94)90044-2.

Ribe, N. M., and Y. Yu (1991), A theory for plastic deformation and textural evolution of olivine polycrystals, *J. Geophys. Res.*, *96*, 8325–8335, doi:10.1029/90JB02721.

Ritzwoller, M. H., N. M. Shapiro, A. L. Levshin, and G. M. Leahy (2001), Crustal and upper mantle structure beneath Antarctica and surrounding oceans, *J. Geophys. Res.*, *106*, 1–26, doi:10.1029/2001JB000179.

Saruwatari, K., S. Ji, C. Long, and M. H. Salisbury (2001), Seismic anisotropy of mantle xenoliths and constraints on upper mantle structure beneath the southern Canadian Cordillera, *Tectonophysics*, *339*, 403–426, doi:10.1016/S0040-1951(01)00136-6.

Schmid, S. M., and M. Casey (1986), Complete fabric analysis of some commonly observed quartz *c*-axis patterns, in *Mineral and Rock Deformation: Laboratory Studies*, *Geophys. Monogr. Ser.*, vol. 36, edited by B. E. Hobbs and H. C. Heard, pp. 263–286 , AGU, Washington, D. C.

Siddoway, C. S., L. C. Sass III, and R. Esser (2005), Kinematic history of Marie Byrd Land terrane, West Antarctica: Direct evidence from Cretaceous mafic dykes, in *Terrane Processes at the Margin of Gondwana*, edited by A. Vaughan, et al., *Geol. Soc. London, Spec. Publ.*, *246*, pp. 417–438, doi:10.1144/GSL.SP.2005.246.01.17

Sieminski, A., E. Debayle, and J. J. Leveque (2003), Seismic evidence for deep low-velocity anomalies in the transition zone beneath West Antarctica, *Earth Planet. Sci. Lett.*, *216*, 645–661, doi:10.1016/S0012-821X(03)00518-1.

Skemer, P., I. Katayama, Z. Jiang, and S. Karato (2005), The misorientation index: Development of a new method for calculating the strength of lattice-preferred orientation, *Tectonophysics*, *411*(1–4), 157–167, doi:10.1016/j.tecto.2005.08.023.

Sundberg, M., and R. F. Cooper (2008), Crystallographic preferred orientation produced by diffusional creep of harzburgite: Effects of chemical interactions among phases during plastic flow, *J. Geophys. Res.*, *113*, B12208, doi:10.1029/2008JB005618.

Tasaka, M., M. E. Zimmerman, and D. L. Kohlstedt (2016), Evolution of the rheological and microstructural properties of olivine aggregates during dislocation creep under hydrous conditions, *J. Geophys. Res. Solid Earth*, *121*, 92–113, doi:10.1002/2015JB012134.

Taylor, W. R. (1998), An experimental test of some geothermometer and geobarometer formulations for upper mantle peridotites with application to the thermobarometry of fertile lherzolite and garnet websterite, *Neues Jahrb. Geol. Palaeontol. Abh.*, *172*, 381–408, doi:10.1127/njma/172/1998/381.

ten Brink, U. T., R. I. Hackney, S. Bannister, T. A. Stern, and Y. Makovsky (1997), Uplift of the Transantarctic Mountains and the bedrock beneath the East Antarctic ice sheet, *J. Geophys. Res.*, *102*, 27,603–27,621, doi:10.1029/97JB02483.

Titus, S. J., S. M. Maes, B. Benford, E. C. Ferré, and B. Tikoff (2011), Fabric development in the mantle section of a paleotransform fault and its effect on ophiolite obduction, New Caledonia, *Lithosphere*, *3*, 221–244, doi:10.1130/L122.1.

Tommasi, A., B. Tikoff, and A. Vauchez (1999), Upper mantle tectonics: Three-dimensional deformation, olivine crystallographic fabrics and seismic properties, *Earth Planet. Sci. Lett.*, *168*, 173–186, doi:10.1016/S0012-821X(99)00046-1.

Tommasi, A., D. Mainprice, G. Canova, and Y. Chastel (2000), Viscoplastic self-consistent and equilibrium-based modeling of olivine lattice preferred orientations: Implications for the upper mantle seismic anisotropy, *J. Geophys. Res.*, *105*, 7893–7908, doi:10.1029/1999JB900411.

Ulrich, S., and D. Mainprice (2005), Does cation ordering in omphacite influence development of lattice-preferred orientation?, *J. Struct. Geol.*, *27*, 419–431, doi:10.1016/j.jsg.2004.11.003.

Underwood, E. (1970), *Quantitative Stereology*, Addison-Wesley, Reading, Mass.

Van der Wal, D., P. Chopra, M. Drury, and J. FitzGerald (1993), Relationships between dynamically recrystallized grain size and deformation conditions in experimentally deformed olivine rocks, *Geophys. Res. Lett.*, *20*, 1479–1482, doi:10.1029/93GL01382.

Vauchez, A., F. Dineur, and R. Rudnick (2005), Microstructure, texture and seismic anisotropy of the lithospheric mantle above a mantle plume: Insights from the Labait volcano xenoliths (Tanzania), *Earth Planet. Sci. Lett.*, *232*, 295–314, doi:10.1016/j.epsl.2005.01.024.

Vollmer, F. W. (1990), An application of eigenvalue methods to structural domain analysis, *Geol. Soc. Am. Bull.*, *102*, 786–791, doi:10.1130/0016-7606(1990)102<0786:AAOEMT>2.3.CO;2.

Warren, J., and G. Hirth (2006), Grain size sensitive deformation mechanisms in naturally deformed peridotites, *Earth Planet. Sci. Lett.*, *248*, 438–450, doi:10.1016/j.epsl.2006.06.006.

Warren, J. M., and E. H. Hauri (2014), Pyroxenes as tracers of mantle water variations, *J. Geophys. Res. Solid Earth*, *119*, 1851–1881, doi:10.1002/2013JB010328.

Warren, J. M., G. Hirth, and P. B. Kelemen (2008), Evolution of olivine lattice preferred orientation during simple shear in the mantle, *Earth Planet. Sci. Lett.*, *272*(3–4), 501–512, doi:10.1016/j.epsl.2008.03.063.

Webber, C., J. Newman, C. W. Holyoke III, T. Little, and B. Tikoff (2010), Fabric development in cm-scale shear zones in ultramafic rocks, Red Hills, New Zealand, *Tectonophysics*, *489*, 55–75, doi:10.1016/j.tecto.2010.04.001.

Wenk, H. R., K. Bennett, G. R. Canova, and A. Molinari (1991), Modeling plastic-deformation of peridotite with the self-consistent theory, *J. Geophys. Res.*, *96*, 8337–8349, doi:10.1029/91JB00117.

Winberry, J. P., and S. Anandakrishnan (2004), Crustal structure of the West Antarctic rift system and Marie Byrd Land hotspot, *Geology*, *32*, 977–980, doi:10.1130/G20768.1.

Withers, A. C., H. Bureau, C. Raepsaet, and M. M. Hirschmann (2012), Calibration of infrared spectroscopy by elastic recoil detection analysis of H in synthetic olivine, *Chem. Geol.*, *334*, 92–98, doi:10.1016/j.chemgeo.2012.10.002.

Xypolias, P., D. Spanos, V. Chatzaras, S. Kokkalas, and I. Koukouvelas (2010), Vorticity of flow in ductile thrust zones: Examples from the Attico-Cycladic Massif (Internal Hellenides, Greece), in *Continental Tectonics and Mountain Building*, edited by R. Law, et al., *Geol. Soc. London, Spec. Publ.*, pp. 687–714, doi:10.1144/SP335.28.

Xypolias, P., V. Chatzaras, R. Beane, and S. Papadopoulou (2013), Heterogeneous constrictional deformation in a ductile shear zone resulting from the transposition of a lineation-parallel fold, *J. Struct. Geol.*, *52*, 44–59, doi:10.1016/j.jsg.2013.05.001.

Zhang, S., S. -I. Karato, J. Fitz Gerald, U. H. Faul, and Y. Zhou (2000), Simple shear deformation of olivine aggregates, *Tectonophysics*, *316*, 133–152, doi:10.1016/S0040-1951(99)00229-2.

Journal of Geophysical Research: Solid Earth

Supporting Information for

Effect of strain-induced fabric geometry on olivine crystallographic texture evolution

Vasileios Chatzaras[1], Seth C. Kruckenberg[1], Shaina M. Cohen[1], L. Gordon Medaris Jr.[2], Anthony C. Withers[3], Brian Bagley[4]

[1]Department of Earth and Environmental Sciences, Boston College, Chestnut Hill, MA 02467, USA
[2]Department of Geoscience, University of Wisconsin-Madison, Madison, WI 53706, USA
[3]Department of Earth Sciences and the Centre for Planetary Science and Exploration, University of Western Ontario, 1151 Richmond Street, London, Ontario N6A 5B7, Canada
[4]Department of Earth Sciences, University of Minnesota - Twin Cities, 310 Pillsbury Dr. SE, Minneapolis, MN 55455, USA

Contents of this file

Additional Supporting Information (Files uploaded separately)

Introduction

This supporting document contains a detailed record of data produced in the course of this work, and adds to the data presented in the manuscript. The supporting information provide the opportunity to the reader to explore the depth of the analysis performed on the FTIR, XRCT, and EPMA data, presented in the manuscript.

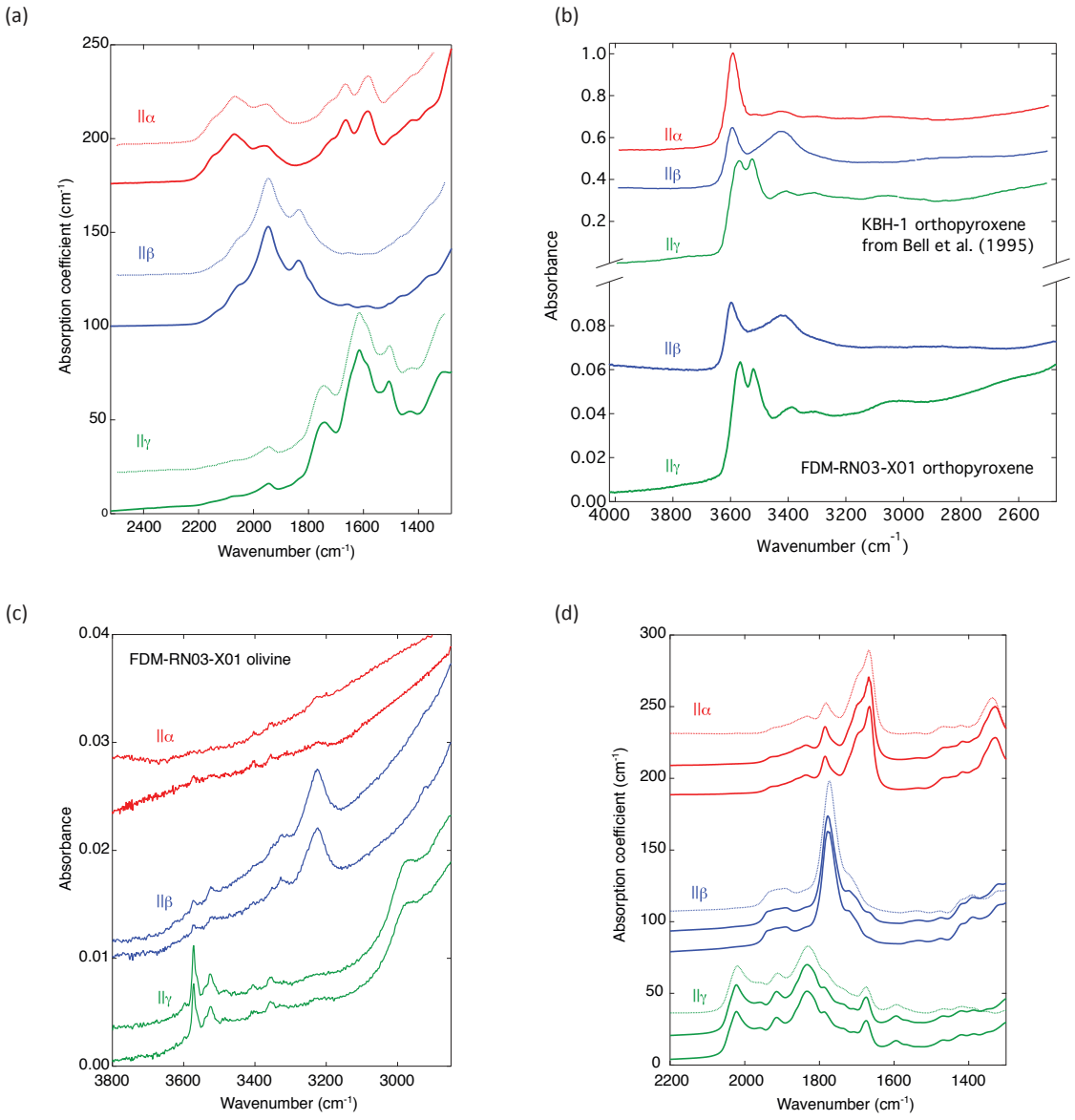

Figure S1. (a) Comparison of the Si-O overtone bands used to orient FDM-RN03-X01 orthopyroxene (solid curves) and the equivalent polarized principal spectra for KBH-1 from *Mosenfelder and Rossman* [2013; dotted curves]. (b) Polarized principal spectra from FDM-RN03-X01 orthopyroxene (lower panel). Sample thickness is 0.185mm (||β and ||γ) and 0.240mm (||α) . Polarized spectra in the upper panel are from sample KBH-1 of *Bell et al.* [1995], from which the molar absorption coefficient was derived. Spectra have been offset for clarity. (c) Representative polarized principal spectra from FDM-RN03-X01 olivine. Sample thickness is 0.305 mm (upper ||β and ||γ), 0.285 mm (lower ||β and ||γ), 0.350 mm (upper ||α) and 0.478 (lower ||α). Spectra have been offset for clarity. (d) Principal polarized spectra used to orient the olivine samples in Figure S1c (solid curves), compared with the principal polarized spectra for sample GRR997 of *Asimow et al.* [2006; dotted curves]. Spectra are normalized to 1 cm thickness. Spectra collected in this study are shown without baseline subtraction, and are offset for clarity.

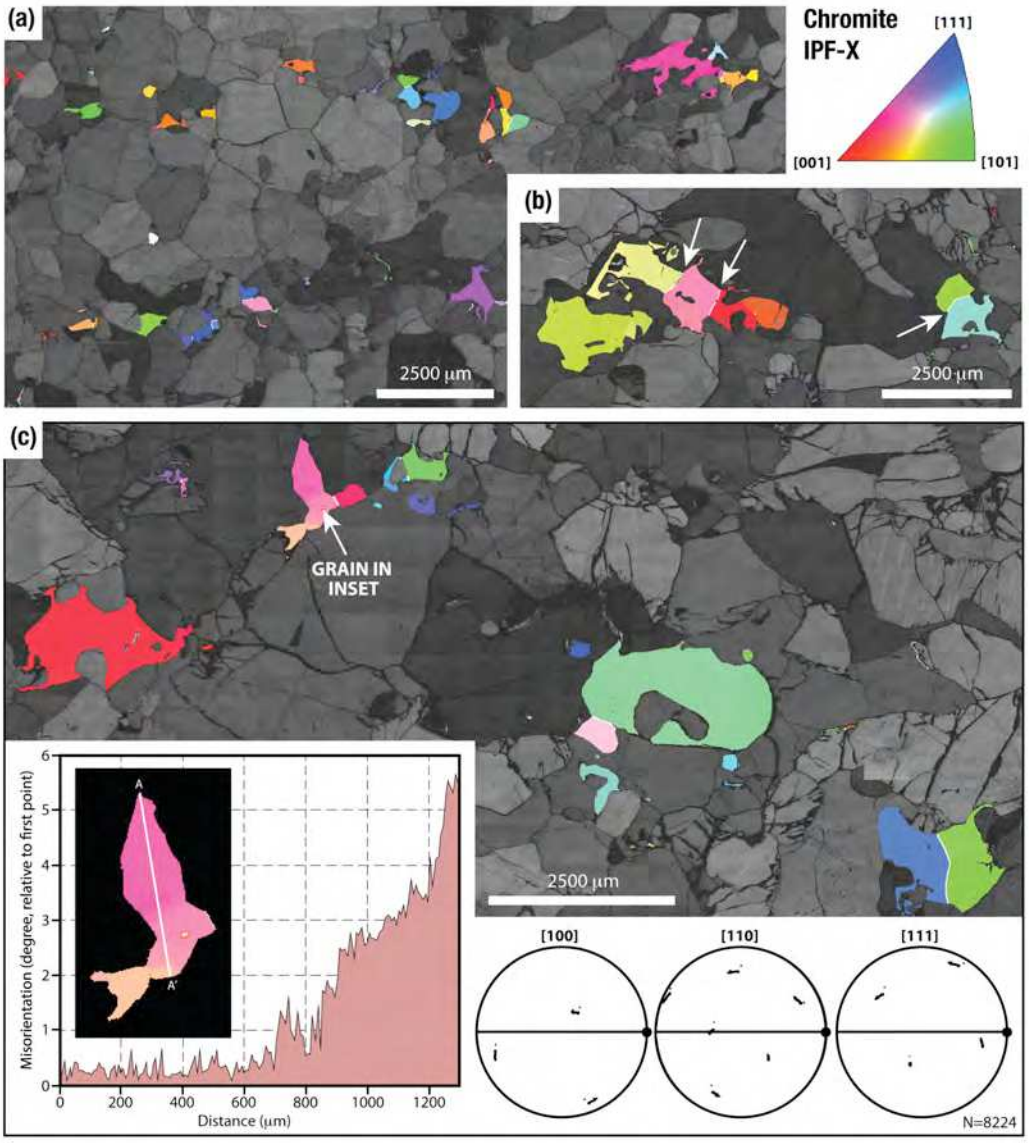

Figure S2. Representative EBSD maps of crystallographic preferred orientations in spinel (chromite). The orientations of spinel crystal axes are colored relative to Φ_1 axis of the spinel fabric ellipsoid (IPF-X coloring); all other phases are shown in gray (based on EBSD band contrast) for clarity. (a) Sample FDM-AVBB07 showing spinel grains with random distribution of crystallographic axes orientations. Spinel grains have minimal internal deformation, as indicated by homogeneous internal microstructure, characteristic of spinel crystallographic patterns in the xenolith suite analyzed. (b) FDM-DB03-X02: White arrows highlight examples of adjacent spinel grains, calculated with 10° misorientation boundaries (white lines), which otherwise lack evidence of significant internal deformation or recrystallization. (c) Spinel grains within sample FDM-DB01-X01 predominately show homogeneous intragrain and random intergrain crystallographic orientations. Limited intracrystalline deformation is observed in some spinel grains, as denoted by misorientations less than 10° (see inset) and minimal dispersion of crystallographic axes orientations in corresponding pole figures (lower-hemisphere, equal area projection).

References

Asimow, P. D., L. C. Stein, J. L. Mosenfelder, and G. R. Rossman (2006), Quantitative polarized FTIR analysis of trace OH in populations of randomly oriented mineral grains, *Am. Mineral., 91*, 278–284, doi: 10.2138/am.2006.1937.

Bell, D.R., P. D. Ihinger, and G. R. Rossman (1995), Quantitative analysis of trace OH in garnet and pyroxenes, *Am. Mineral*, 80, 465–474.

Mosenfelder, J.D., and G. R. Rossman (2013) Analysis of hydrogen and fluorine in pyroxenes by SIMS and FTIR. Part 1. Orthopyroxene, *Am. Mineral.,98*,1026–1041, doi: 10.2138/am.2013.4413.

Volcanic center	Latitude (S)	Longitude (W)
Fosdick Mountains		
Mt. Avers	76.481°	145.396°
Bird Bluff	76.504°	144.598°
Demas Bluff	76.568°	144.853°
Marujupu	76.508°	145.670°
Recess Nunatak	76.519°	144.507°
Usas Escarpment		
Mt. Aldaz	76.051°	124.417°
Executive Committee Range		
Mt. Cumming	76.667°	125.820°

Table S1. Geographic coordinates of the volcanic centers from which xenoliths were sampled.

Voltage	150-200 kV
Current	150-700 µA
Frame rate	1.3-9.2 fps
Source to detector distance	794-997 mm
Source to sample distance	126-643 mm
Number of projections	1080
Frame averaging	3-4
Voxel size (isotropic)	9.74-48.4 µm

Table S2. Parameters of X-ray computed tomography scans.

Table S3. Mineral compositions for the Marie Byrd Land spinel peridotite xenoliths

Sample	T (°C) calculated at an assumed pressure of 15 kbar					Ol-Spl	P (kbar)	$Depth_{max}$ (km)	H (km)
	2-Px BM[a]	2-Px BK[b]	2-Px T[c]	2-Px Avg	1 std dev	BBG[d]		O[e]	
Fosdick Mountains									
FDM-AV01-X01	937	978	902	939	38	---	16	57	50
FDM-BB01-X01	931	968	937	945	20	---	17	56	51
FDM-BB02-X01	1052	1088	1019	1053	34	---	20	56	60
FDM-BB03-X01	855	886	826	856	30	---	15	74	45
FDM-DB01-X01	1023	1065	983	1024	41	---	19	57	58
FDM-DB02-X01	1178	1200	1169	1183	16	---	23	71	71
FDM-DB02-X02	970	985	978	978	7	---	18	94	54
FDM-DB02-X03	987	1034	976	999	31	---	18	58	55
FDM-DB02-X04	927	980	892	933	44	---	16	60	50
FDM-DB02-X06	1205	1203	1186	1198	11	---	23	---	72
FDM-DB02-X08	801	814	792	803	11	---	13	78	41
FDM-DB02-X10	1014	1060	987	1020	37	---	19	59	57
FDM-DB02-X11	1032	1076	1009	1039	34	---	19	66	59
FDM-DB02-X12	1033	1074	1001	1036	37	---	19	59	59
FDM-DB02-X13	906	957	870	911	44	---	16	53	49
FDM-DB03-X01	855	886	826	856	30	---	14	74	44
FDM-DB03-X02	851	913	820	861	47	---	14	53	44
FDM-DB03-X03	975	1022	948	982	37	---	18	55	54
FDM-DB03-X04	995	1015	995	1002	11	---	18	80	56
FDM-DB04-X01	993	1033	945	991	44	---	18	57	55
FDM-DB04-X02	980	1026	947	984	40	---	18	56	54
FDM-DB04-X03	1171	1174	1152	1165	12	---	23	92	69
FDM-DB04-X04	963	980	962	968	10	---	17	81	53
FDM-MJ01-X02	966	1019	937	974	41	---	17	55	53
FDM-MJ01-X03	924	979	882	929	49	---	16	55	50
FDM-MJ01-X05	1010	1054	976	1014	39	---	19	58	57
FDM-MJ01-X06	1076	1099	1033	1070	34	---	20	58	61
FDM-RN01-X01	953	995	934	961	31	---	17	70	52
FDM-RN02-X01	818	875	791	828	43	---	14	50	42
FDM-RN03-X01	941	989	899	943	45	---	17	68	51
FDM-RN04-X01	806	860	771	812	45	---	14	49	42
FDM-AVBB01	930	984	898	937	44	---	16	51	50
FDM-AVBB02	781	814	743	779	36	---	13	52	39
FDM-AVBB04	817	861	788	822	37	---	14	49	42
FDM-AVBB05	810	855	777	814	39	---	14	51	42
FDM-AVBB06	930	980	910	940	36	---	16	52	50
FDM-AVBB07	801	850	764	805	43	---	13	51	41
FDM-AVBB08	831	873	791	832	41	---	14	51	43
USAS Escarpment									
AD6021-X02	1081	1116	1056	1084	30	---	21	61	63
Executive Committee Range									
KSP89-181-X01	---	---	---	---	---	862	14	93	42
KSP89-181-X01	---	---	---	---	---	995	17	105	52

[a]*Bertrand and Mercier* [1985]; [b]*Brey and Köhler* [1990]; [c]*Taylor* [1998]; [d]*Ballhaus et al.* [1991], T from Fe-Mg exchange in Ol-Spl; [e]*O'Neil* [1981]; H, estimated extraction depth

Table S4. Temperature, pressure, and extraction depth estimates for the Marie Byrd Land spinel peridotite xenoliths

Movie S1. Tomographic visualization of the three-dimensional shape preferred orientation of the spinel grains in the xenolith shown in Figure 3a and 3b of the manuscript. Red objects represent the spinel grains.

VOLCANIC CENTER	*Mt. Avers*	*Bird Bluff*	*Bird Bluff*	*Bird Bluff*	*Demas Bluff*	*Demas Bluff*	*Demas Bluff*	*Demas Bluff*	*Demas Bluff*	*Demas Bluff*
SAMPLE	**FDM-AV01-X01**	**FDM-BB01-X01**	**FDM-BB02-X01**	**FDM-BB03-X01**	**FDM-DB01-X01**	**FDM-DB02-X01**	**FDM-DB02-X02**	**FDM-DB02-X03**	**FDM-DB02-X04**	**FDM-DB02-X06**
T°C @ 15 kbar	*939*	*945*	*1053*	*856*	*1024*	*1183*	*978*	*999*	*933*	*1198*
OLIVINE										
wt. %										
SiO2	40.79	40.51	40.25	41.08	40.62	40.75	41.11	40.79	40.81	39.41
FeO	9.65	11.34	11.36	8.59	10.26	9.19	8.26	9.47	9.60	15.64
MnO	0.13	0.08	0.07	0.12	0.07	0.12	0.11	0.15	0.14	0.18
MgO	49.08	47.51	47.41	49.82	48.32	49.20	50.08	49.01	48.94	43.99
NiO	0.35	0.38	0.39	0.36	0.36	0.38	0.36	0.36	0.37	0.24
CaO	0.04	0.03	0.05	0.001	0.02	0.09	0.04	0.04	0.06	0.04
Sum	100.04	99.84	99.53	99.97	99.66	99.74	99.95	99.82	99.90	99.49
Si	1.000	1.002	1.000	1.002	1.002	1.000	1.002	1.001	1.001	0.999
Fe	0.198	0.235	0.236	0.175	0.212	0.189	0.168	0.194	0.197	0.331
Mn	0.003	0.002	0.001	0.002	0.001	0.002	0.002	0.003	0.003	0.004
Mg	1.793	1.752	1.755	1.812	1.776	1.801	1.819	1.793	1.790	1.662
Ni	0.007	0.008	0.008	0.007	0.007	0.008	0.007	0.007	0.007	0.005
Ca	0.001	0.001	0.001	0.000	0.001	0.002	0.001	0.001	0.001	0.001
Sum	3.001	2.999	3.002	2.998	2.999	3.002	2.999	3.000	3.000	3.002
Mg#	90.1	88.2	88.2	91.2	89.4	90.5	91.5	90.2	90.1	83.4
ORTHOPYROXENE										
wt. %										
SiO2	54.49	54.69	54.34	55.12	54.39	53.49	56.18	54.10	54.27	52.43
TiO2	0.10	0.10	0.13	0.02	0.14	0.12	0.02	0.12	0.11	0.31
Al2O3	4.22	3.91	4.57	3.10	4.70	5.84	1.86	5.18	4.19	6.10
Cr2O3	0.41	0.32	0.26	0.59	0.33	0.63	0.52	0.46	0.47	0.04
FeO	6.62	7.39	6.99	5.63	6.49	5.80	5.24	6.25	6.26	9.82
MnO	0.16	0.16	0.16	0.13	0.14	0.12	0.14	0.13	0.14	0.17
MgO	33.05	32.89	32.60	34.43	32.94	32.29	35.12	33.17	33.35	29.05
CaO	0.44	0.41	0.58	0.40	0.54	1.37	0.45	0.50	0.51	1.63
Na2O	0.03	0.02	0.11	0.03	0.09	0.14	0.02	0.08	0.09	0.19
Sum	99.50	99.89	99.74	99.43	99.77	99.78	99.55	99.99	99.38	99.74
Si	1.895	1.901	1.889	1.911	1.886	1.856	1.941	1.871	1.889	1.853
Ti	0.003	0.002	0.003	0.000	0.004	0.003	0.001	0.003	0.003	0.008
Al	0.173	0.160	0.187	0.127	0.192	0.239	0.076	0.211	0.172	0.254
Cr	0.011	0.009	0.007	0.016	0.009	0.017	0.014	0.013	0.013	0.001
Fe	0.192	0.215	0.203	0.163	0.188	0.168	0.151	0.181	0.182	0.290
Mn	0.005	0.005	0.005	0.004	0.004	0.004	0.004	0.004	0.004	0.005
Mg	1.714	1.704	1.690	1.780	1.703	1.670	1.809	1.710	1.731	1.531
Ca	0.016	0.015	0.022	0.015	0.020	0.051	0.017	0.019	0.019	0.062
Na	0.002	0.001	0.007	0.002	0.006	0.009	0.001	0.005	0.006	0.013
Sum	4.011	4.013	4.014	4.018	4.012	4.017	4.014	4.017	4.019	4.017
Ca	0.8	0.8	1.1	0.8	1.0	2.7	0.8	1.0	1.0	3.3
Mg	89.1	88.1	88.3	90.9	89.1	88.4	91.5	89.6	89.6	81.3
Fe	10.0	11.1	10.6	8.3	9.8	8.9	7.7	9.5	9.4	15.4
Mg #	89.9	88.8	89.3	91.6	90.1	90.8	92.3	90.4	90.5	84.1
CLINOPYROXENE										
wt. %										
SiO2	51.71	52.46	52.17	53.70	52.22	51.22	54.18	52.43	51.85	50.66
TiO2	0.62	0.47	0.64	0.13	0.65	0.27	0.03	0.52	0.57	0.78
Al2O3	7.64	5.76	7.33	4.74	7.71	6.90	1.82	6.91	6.75	7.76
Cr2O3	1.10	0.80	0.65	1.48	0.78	1.05	0.78	0.84	1.23	0.06
FeO	2.32	2.58	2.90	1.96	2.66	3.32	1.76	2.66	2.59	6.34
MnO	0.08	0.10	0.12	0.08	0.07	0.10	0.05	0.10	0.08	0.15
MgO	14.19	15.20	15.03	15.39	14.71	17.20	18.09	15.17	14.79	16.63
CaO	19.71	20.74	18.66	20.88	18.76	18.25	22.44	19.74	19.70	16.41
Na2O	1.96	1.30	1.89	1.82	2.12	1.17	0.30	1.77	2.04	1.30
Sum	99.33	99.41	99.39	100.20	99.68	99.48	99.47	100.14	99.60	100.09
Si	1.876	1.906	1.888	1.935	1.883	1.857	1.966	1.888	1.882	1.84
Ti	0.017	0.013	0.017	0.004	0.018	0.007	0.001	0.014	0.016	0.02
Al	0.327	0.247	0.313	0.201	0.328	0.295	0.078	0.293	0.289	0.33
Cr	0.032	0.023	0.019	0.042	0.022	0.030	0.022	0.024	0.035	0.00
Fe	0.071	0.078	0.088	0.059	0.080	0.101	0.053	0.080	0.079	0.19
Mn	0.002	0.003	0.004	0.002	0.002	0.003	0.002	0.003	0.002	0.00
Mg	0.768	0.823	0.811	0.827	0.791	0.930	0.978	0.814	0.800	0.90
Ca	0.766	0.807	0.724	0.806	0.725	0.709	0.872	0.761	0.766	0.64
Na	0.138	0.092	0.133	0.127	0.148	0.082	0.021	0.123	0.144	0.09
Sum	3.996	3.992	3.995	4.004	3.998	4.014	3.994	4.001	4.012	4.019
Ca	47.8	47.2	44.6	47.6	45.4	40.8	45.8	46.0	46.6	36.9
Mg	47.8	48.2	50.0	48.9	49.6	53.4	51.4	49.2	48.6	52.0
Fe	4.4	4.6	5.4	3.5	5.0	5.8	2.8	4.8	4.8	11.1
Mg #	91.6	91.3	90.2	93.3	90.8	90.2	94.8	91.0	91.0	82.4
SPINEL										
wt. %										
TiO2	0.07	0.04	0.11	0.02	0.11	0.17	0.04	0.11	0.15	- - -
Al2O3	56.06	55.71	59.42	39.21	59.56	52.47	26.49	57.56	52.68	- - -
Cr2O3	11.99	11.24	7.57	28.64	7.94	14.59	42.97	9.76	14.88	- - -
V2O3	0.05	0.07	0.05	0.09	0.04	0.04	0.19	0.04	0.06	- - -
FeO	10.73	12.06	10.57	13.46	9.87	10.32	14.05	10.52	11.31	- - -
MnO	0.10	0.06	0.04	0.14	0.04	0.09	0.19	0.08	0.12	- - -
MgO	19.87	19.67	21.34	16.44	21.85	20.83	15.02	20.95	19.66	- - -
CaO	0.00	0.00	0.00	0.00	0.00	0.00	0.00	0.00	0.00	- - -
ZnO	0.15	0.16	0.12	0.25	0.08	0.07	0.12	0.08	0.13	- - -
NiO	0.34	0.35	0.41	0.18	0.38	0.34	0.11	0.35	0.34	- - -
Sum	99.35	99.34	99.65	98.43	99.88	98.91	99.17	99.45	99.32	- - -
Ti	0.001	0.001	0.002	0.000	0.002	0.003	0.001	0.002	0.003	- - -
Al	1.733	1.730	1.803	1.324	1.798	1.644	0.942	1.762	1.652	- - -
Cr	0.249	0.234	0.154	0.649	0.161	0.307	1.025	0.200	0.313	- - -
V	0.001	0.001	0.001	0.002	0.001	0.001	0.005	0.001	0.001	- - -
Fe	0.235	0.266	0.228	0.322	0.212	0.229	0.354	0.228	0.252	- - -
Mn	0.002	0.001	0.001	0.003	0.001	0.002	0.005	0.002	0.003	- - -
Mg	0.777	0.773	0.819	0.702	0.834	0.826	0.676	0.811	0.780	- - -
Ca	0.000	0.000	0.000	0.000	0.000	0.000	0.000	0.000	0.000	- - -
Zn	0.003	0.003	0.002	0.005	0.002	0.001	0.003	0.002	0.003	- - -
Ni	0.007	0.007	0.008	0.004	0.008	0.007	0.003	0.007	0.007	- - -
Sum	3.008	3.016	3.019	3.012	3.018	3.021	3.013	3.016	3.014	- - -
Fe2+	0.215	0.222	0.178	0.290	0.163	0.174	0.320	0.186	0.215	- - -
Fe3+	0.020	0.044	0.050	0.033	0.048	0.055	0.035	0.043	0.037	- - -
XMg	0.783	0.777	0.822	0.708	0.836	0.826	0.679	0.814	0.784	- - -
XCr	0.125	0.119	0.079	0.329	0.082	0.157	0.521	0.102	0.159	- - -
YCr	0.124	0.117	0.077	0.324	0.080	0.153	0.512	0.100	0.156	- - -
YAl	0.866	0.862	0.898	0.660	0.896	0.820	0.471	0.879	0.825	- - -
YFe3+	0.010	0.022	0.025	0.016	0.024	0.028	0.017	0.021	0.018	- - -
Spl	0.685	0.684	0.757	0.475	0.768	0.696	0.325	0.731	0.659	- - -
Hc	0.190	0.197	0.164	0.196	0.150	0.147	0.154	0.167	0.182	- - -
MgChr	0.098	0.093	0.065	0.233	0.069	0.130	0.354	0.083	0.125	- - -
Chr	0.027	0.027	0.014	0.096	0.013	0.027	0.167	0.019	0.034	- - -
Sum	1.000	1.000	1.000	1.000	1.000	1.000	1.000	1.000	1.000	- - -
ρ	3.84	3.84	3.77	4.07	3.76	3.83	4.25	3.79	3.87	- - -

Demas Bluff	*Demas Bluff*	*Demas Bluff*	*Demas Bluff*	*Demas Bluff*	*Demas Bluff*	*Demas Bluff*	*Demas Bluff*	*Demas Bluff*	*Demas Bluff*	*Demas Bluff*
FDM-DB02-X08	**FDM-DB02-X10**	**FDM-DB02-X11**	**FDM-DB02-X12**	**FDM-DB02-X13**	**FDM-DB03-X01**	**FDM-DB03-X02**	**FDM-DB03-X03**	**FDM-DB03-X04**	**FDM-DB04-X01**	**FDM-DB04-X02**
803	*1020*	*1039*	*1036*	*911*	*856*	*861*	*982*	*1002*	*991*	*984*
41.11	40.72	41.01	40.82	40.59	41.08	40.63	40.93	40.54	40.71	40.46
8.04	9.82	9.16	9.67	10.18	8.59	10.17	10.02	8.03	8.63	9.89
0.11	0.13	0.14	0.14	0.12	0.12	0.14	0.15	0.13	0.14	0.14
50.49	48.67	49.46	48.80	48.13	49.82	48.47	48.77	50.31	49.75	48.87
0.39	0.37	0.40	0.36	0.36	0.36	0.37	0.37	0.40	0.40	0.40
0.04	0.03	0.07	0.03	0.00	0.00	0.04	0.05	0.035	0.03	0.035
100.19	99.73	100.23	99.82	99.39	99.97	99.82	100.28	99.44	99.66	99.79
0.999	1.002	1.001	1.00	1.003	1.002	1.001	1.002	0.993	0.998	0.996
0.163	0.202	0.187	0.20	0.210	0.175	0.209	0.205	0.165	0.177	0.204
0.002	0.003	0.003	0.00	0.003	0.002	0.003	0.003	0.003	0.003	0.003
1.829	1.785	1.800	1.79	1.773	1.812	1.779	1.780	1.838	1.817	1.793
0.008	0.007	0.008	0.01	0.007	0.007	0.007	0.007	0.008	0.008	0.008
0.001	0.001	0.0019	0.00	0.000	0.000	0.001	0.001	0.001	0.001	0.001
3.002	2.999	3.001	2.998	2.997	2.998	3.001	2.999	3.008	3.003	3.005
91.8	89.8	90.6	90.0	89.4	91.2	89.5	89.7	91.8	91.1	89.8
56.27	53.66	54.79	54.43	54.37	55.12	54.37	54.28	55.80	54.99	54.17
0.01	0.15	0.08	0.13	0.16	0.02	0.14	0.14	0.02	0.12	0.11
2.45	5.08	4.10	4.83	4.48	3.10	4.42	4.90	2.69	3.41	4.74
0.09	0.49	0.46	0.40	0.31	0.59	0.05	0.35	0.51	0.58	0.31
5.20	6.44	5.84	6.32	6.58	5.63	6.58	6.56	5.14	5.66	6.37
0.13	0.14	0.12	0.14	0.16	0.13	0.15	0.14	0.11	0.13	0.16
35.08	32.74	33.90	33.17	33.09	34.43	33.11	33.49	34.86	33.92	32.98
0.53	0.52	0.59	0.54	0.43	0.40	0.53	0.46	0.45	0.46	0.55
0.02	0.07	0.10	0.09	0.05	0.03	0.08	0.07	0.03	0.08	0.09
99.79	99.30	99.98	100.05	99.64	99.43	99.43	100.37	99.61	99.35	99.45
1.936	1.871	1.892	1.881	1.888	1.911	1.892	1.872	1.926	1.909	1.884
0.000	0.004	0.002	0.003	0.004	0.000	0.004	0.004	0.001	0.003	0.003
0.099	0.209	0.167	0.197	0.183	0.127	0.181	0.199	0.109	0.139	0.194
0.003	0.013	0.012	0.011	0.009	0.016	0.001	0.009	0.014	0.016	0.008
0.150	0.188	0.169	0.183	0.191	0.163	0.191	0.189	0.148	0.164	0.185
0.004	0.004	0.004	0.004	0.005	0.004	0.004	0.004	0.003	0.004	0.005
1.800	1.702	1.745	1.709	1.713	1.780	1.717	1.723	1.793	1.755	1.710
0.019	0.019	0.022	0.020	0.016	0.015	0.020	0.017	0.017	0.017	0.020
0.001	0.005	0.007	0.006	0.003	0.002	0.006	0.004	0.002	0.005	0.006
4.013	4.016	4.020	4.014	4.013	4.018	4.016	4.022	4.013	4.013	4.015
1.0	1.0	1.1	1.0	0.8	0.8	1.0	0.9	0.9	0.9	1.1
91.4	89.1	90.2	89.4	89.2	90.9	89.0	89.3	91.6	90.6	89.3
7.6	9.8	8.7	9.6	10.0	8.3	9.9	9.8	7.6	8.5	9.7
92.3	90.1	91.2	90.3	90.0	91.6	90.0	90.1	92.4	91.4	90.2
53.99	51.79	52.37	52.51	51.63	53.70	51.69	52.15	53.85	52.78	52.10
0.04	0.60	0.34	0.55	0.79	0.13	0.66	0.63	0.05	0.50	0.62
2.72	7.00	6.41	7.15	7.84	4.74	7.54	7.52	3.45	5.84	7.64
0.20	0.90	1.21	0.88	0.79	1.48	0.14	0.80	1.14	1.64	0.79
1.79	2.83	2.63	2.71	2.53	1.96	2.81	2.60	1.79	2.27	2.54
0.06	0.09	0.08	0.08	0.08	0.08	0.09	0.10	0.07	0.08	0.07
17.37	15.09	15.56	15.23	14.22	15.39	14.51	14.66	17.07	15.08	14.44
23.28	18.91	19.41	18.96	19.89	20.88	20.25	19.46	21.54	19.21	19.16
0.65	1.98	1.65	1.98	2.04	1.82	2.05	1.97	0.73	2.04	2.10
100.11	99.20	99.67	100.06	99.82	100.20	99.75	99.89	99.70	99.44	99.46
1.950	1.883	1.894	1.889	1.867	1.935	1.873	1.881	1.946	1.912	1.885
0.001	0.016	0.009	0.015	0.022	0.004	0.018	0.017	0.001	0.014	0.017
0.116	0.300	0.273	0.303	0.334	0.201	0.322	0.320	0.147	0.249	0.326
0.006	0.026	0.035	0.025	0.022	0.042	0.004	0.023	0.033	0.047	0.023
0.054	0.086	0.080	0.082	0.076	0.059	0.085	0.079	0.054	0.069	0.077
0.002	0.003	0.002	0.002	0.003	0.002	0.003	0.003	0.002	0.002	0.002
0.935	0.818	0.839	0.816	0.767	0.827	0.783	0.788	0.920	0.815	0.779
0.901	0.737	0.752	0.731	0.770	0.806	0.786	0.752	0.834	0.746	0.743
0.046	0.140	0.116	0.138	0.143	0.127	0.144	0.138	0.051	0.144	0.147
4.011	4.008	4.001	4.002	4.005	4.004	4.018	4.000	3.988	3.998	3.998
47.7	44.9	45.0	44.9	47.7	47.6	47.5	46.5	46.1	45.8	46.5
49.5	49.9	50.2	50.1	47.5	48.9	47.3	48.7	50.9	50.0	48.7
2.9	5.2	4.8	5.0	4.7	3.5	5.2	4.9	3.0	4.2	4.8
94.5	90.5	91.3	90.9	90.9	93.3	90.2	90.9	94.4	92.2	91.0
0.05	0.12	0.12	0.11	0.07	0.02	0.12	0.08	0.04	0.10	0.10
36.78	56.97	51.49	57.47	58.34	39.21	58.26	59.09	38.59	59.31	59.31
32.43	10.75	15.71	10.25	8.48	28.64	8.45	8.67	30.91	8.43	8.43
0.07	0.08	0.06	0.06	0.05	0.09	0.05	0.05	0.09	0.05	0.05
11.82	10.66	11.24	10.54	10.19	13.46	10.89	10.43	11.75	10.76	10.76
0.15	0.09	0.12	0.09	0.06	0.14	0.10	0.10	0.15	0.08	0.08
18.04	20.71	20.04	20.91	20.23	16.44	21.51	20.78	17.98	20.92	20.92
0.00	0.00	0.00	0.00	0.00	0.00	0.00	0.00	0.00	0.00	0.00
0.11	0.07	0.10	0.10	0.12	0.25	0.13	0.14	0.14	0.13	0.13
0.17	0.39	0.36	0.37	0.38	0.18	0.38	0.41	0.20	0.42	0.42
99.61	99.81	99.24	99.88	97.92	98.43	99.89	99.75	99.84	100.18	100.18
0.001	0.002	0.002	0.002	0.001	0.0005	0.002	0.001	0.001	0.002	0.002
1.232	1.745	1.622	1.755	1.804	1.3238	1.773	1.796	1.281	1.795	1.795
0.729	0.221	0.332	0.210	0.176	0.6488	0.172	0.177	0.688	0.171	0.171
0.002	0.002	0.001	0.001	0.001	0.0020	0.001	0.001	0.002	0.001	0.001
0.281	0.232	0.251	0.228	0.223	0.3224	0.235	0.225	0.277	0.231	0.231
0.003	0.002	0.003	0.002	0.001	0.0033	0.002	0.002	0.004	0.002	0.002
0.764	0.802	0.799	0.808	0.791	0.7019	0.828	0.799	0.755	0.801	0.801
0.000	0.000	0.000	0.000	0.000	0.0000	0.000	0.000	0.000	0.000	0.000
0.002	0.001	0.002	0.002	0.002	0.0053	0.003	0.003	0.003	0.002	0.002
0.004	0.008	0.008	0.008	0.008	0.0042	0.008	0.008	0.005	0.009	0.009
3.018	3.014	3.020	3.015	3.008	3.012	3.024	3.012	3.014	3.014	3.014
0.233	0.194	0.198	0.188	0.201	0.290	0.170	0.193	0.240	0.193	0.193
0.048	0.038	0.053	0.040	0.022	0.033	0.065	0.032	0.037	0.038	0.038
0.766	0.805	0.801	0.811	0.797	0.708	0.830	0.805	0.759	0.806	0.806
0.372	0.112	0.170	0.107	0.089	0.329	0.089	0.090	0.350	0.087	0.087
0.363	0.110	0.165	0.105	0.088	0.324	0.086	0.088	0.343	0.085	0.085
0.613	0.871	0.808	0.875	0.901	0.660	0.882	0.896	0.638	0.896	0.896
0.024	0.019	0.026	0.020	0.011	0.016	0.032	0.016	0.018	0.019	0.019
0.481	0.715	0.665	0.724	0.726	0.475	0.756	0.733	0.494	0.736	0.736
0.147	0.173	0.165	0.169	0.185	0.196	0.155	0.177	0.157	0.177	0.177
0.285	0.090	0.136	0.087	0.071	0.233	0.074	0.072	0.265	0.070	0.070
0.087	0.022	0.034	0.020	0.018	0.096	0.015	0.017	0.084	0.017	0.017
1.000	1.000	1.000	1.000	1.000	1.000	1.000	1.000	1.000	1.000	1.000
4.06	3.81	3.86	3.80	3.80	4.07	3.77	3.79	4.05	3.79	3.79

Demas Bluff	*Demas Bluff*	*Marujupu*	*Marujupu*	*Marujupu*	*Marujupu*	*Recess Nunatak*	*Recess Nunatak*	*Recess Nunatak*	*Recess Nunatak*	*Mt. Avers - Bird Bluff*
FDM-DB04-X03	**FDM-DB04-X04**	**FDM-MJ01-X02**	**FDM-MJ01-X03**	**FDM-MJ01-X05**	**FDM-MJ01-X06**	**FDM-RN01-X01**	**FDM-RN02-X01**	**FDM-RN03-X01**	**FDM-RN04-X01**	**FDM-AVBB01**
1165	*968*	*974*	*929*	*1014*	*1070*	*961*	*828*	*943*	*812*	*763*
40.87	41.12	40.55	40.63	40.75	40.55	41.04	40.47	40.95	40.54	40.61
7.90	7.74	10.61	9.91	9.90	11.20	8.16	10.78	8.77	10.54	10.09
0.11	0.11	0.15	0.13	0.15	0.16	0.15	0.13	0.13	0.13	0.14
50.39	50.44	48.06	48.67	48.77	47.72	50.13	48.03	49.50	48.43	48.62
0.41	0.38	0.36	0.36	0.35	0.38	0.37	0.38	0.34	0.39	0.37
0.035	0.03	0.03	0.03	0.03	0.04	0.06	0.04	0.076	0.03	0.06
99.71	99.82	99.76	99.71	99.95	100.03	99.89	99.84	99.77	100.08	99.89
0.998	1.001	1.001	1.000	1.001	1.001	1.001	0.999	1.002	0.998	0.999
0.161	0.157	0.219	0.204	0.203	0.231	0.166	0.223	0.180	0.217	0.208
0.002	0.002	0.003	0.003	0.003	0.003	0.003	0.003	0.003	0.003	0.003
1.834	1.831	1.769	1.786	1.785	1.756	1.822	1.768	1.806	1.777	1.784
0.008	0.007	0.007	0.007	0.007	0.007	0.007	0.008	0.007	0.008	0.007
0.001	0.001	0.001	0.001	0.001	0.001	0.002	0.001	0.002	0.001	0.001
3.003	3.000	3.000	3.001	3.000	3.000	3.001	3.002	3.000	3.003	3.002
91.9	92.1	89.0	89.8	89.8	88.4	91.6	88.8	91.0	89.1	89.6
55.97	55.78	53.81	54.04	54.27	53.59	55.33	54.33	54.83	54.15	54.26
0.01	0.02	0.09	0.11	0.13	0.10	0.06	0.12	0.13	0.12	0.11
2.59	2.75	4.42	4.63	4.44	5.12	3.25	4.78	3.83	4.86	4.58
0.63	0.63	0.32	0.39	0.36	0.45	0.47	0.03	0.60	0.03	0.28
5.14	5.07	6.78	6.61	6.34	7.33	5.44	7.14	5.72	6.93	6.48
0.14	0.14	0.15	0.16	0.17	0.17	0.14	0.16	0.12	0.15	0.14
34.80	34.85	33.05	33.14	33.24	32.55	34.24	32.90	33.44	32.98	32.92
0.46	0.40	0.38	0.43	0.43	0.32	0.48	0.49	0.67	0.40	0.62
0.02	0.01	0.03	0.06	0.10	0.06	0.02	0.04	0.15	0.05	0.20
99.75	99.65	99.03	99.54	99.48	99.66	99.43	99.99	99.48	99.68	99.59
1.929	1.924	1.883	1.880	1.887	1.868	1.916	1.884	1.902	1.882	1.886
0.000	0.001	0.002	0.003	0.003	0.002	0.002	0.003	0.003	0.003	0.003
0.105	0.112	0.182	0.190	0.182	0.210	0.133	0.195	0.157	0.199	0.188
0.017	0.017	0.009	0.011	0.010	0.012	0.013	0.001	0.016	0.001	0.008
0.148	0.146	0.198	0.192	0.184	0.214	0.158	0.207	0.166	0.201	0.188
0.004	0.004	0.004	0.005	0.005	0.005	0.004	0.005	0.004	0.004	0.004
1.788	1.792	1.724	1.719	1.723	1.692	1.767	1.701	1.730	1.708	1.706
0.017	0.015	0.014	0.016	0.016	0.012	0.018	0.018	0.025	0.015	0.023
0.001	0.001	0.002	0.004	0.007	0.004	0.001	0.002	0.010	0.003	0.014
4.010	4.011	4.020	4.019	4.017	4.020	4.011	4.016	4.013	4.017	4.020
0.9	0.8	0.7	0.8	0.8	0.6	0.9	0.9	1.3	0.8	1.2
91.5	91.7	89.0	89.2	89.6	88.2	91.0	88.3	90.1	88.8	89.0
7.6	7.5	10.2	10.0	9.6	11.1	8.1	10.8	8.6	10.5	9.8
92.3	92.5	89.7	89.9	90.3	88.8	91.8	89.1	91.2	89.5	90.1
54.38	53.78	51.61	51.56	52.13	50.81	52.66	51.90	52.34	51.69	51.97
0.01	0.08	0.61	0.68	0.55	0.83	0.24	0.65	0.48	0.64	0.58
2.42	2.93	7.91	7.94	7.14	7.81	5.24	8.14	6.18	8.23	7.25
0.88	1.07	0.98	1.02	0.87	1.07	1.43	0.12	1.47	0.11	0.69
2.09	1.68	2.71	2.59	2.63	2.82	2.19	2.74	2.38	2.67	2.77
0.08	0.08	0.08	0.09	0.09	0.07	0.10	0.10	0.07	0.09	0.08
19.57	17.22	13.99	13.83	14.88	15.24	15.40	14.02	15.05	14.06	15.06
19.93	21.79	19.11	19.06	18.99	18.45	20.31	20.44	19.62	20.49	19.83
0.44	0.74	2.06	2.35	1.99	1.78	1.52	2.12	2.10	2.14	2.06
99.79	99.37	99.05	99.13	99.26	98.88	99.10	100.24	99.70	100.13	100.31
1.956	1.952	1.877	1.875	1.890	1.852	1.918	1.870	1.896	1.865	1.872
0.000	0.002	0.017	0.019	0.015	0.023	0.007	0.018	0.013	0.017	0.016
0.103	0.125	0.339	0.340	0.305	0.335	0.225	0.346	0.264	0.350	0.308
0.025	0.031	0.028	0.029	0.025	0.031	0.041	0.003	0.042	0.003	0.020
0.063	0.051	0.083	0.079	0.080	0.086	0.067	0.083	0.072	0.081	0.084
0.002	0.002	0.002	0.003	0.003	0.002	0.003	0.003	0.002	0.003	0.003
1.049	0.932	0.759	0.750	0.804	0.828	0.836	0.753	0.813	0.756	0.809
0.768	0.847	0.745	0.743	0.738	0.721	0.793	0.789	0.761	0.792	0.766
0.030	0.052	0.145	0.166	0.140	0.126	0.107	0.148	0.148	0.150	0.144
3.996	3.994	3.995	4.004	4.000	4.005	3.996	4.012	4.012	4.016	4.020
40.8	46.3	47.0	47.3	45.5	44.1	46.8	48.6	46.2	48.6	46.2
55.8	50.9	47.8	47.7	49.6	50.6	49.3	46.4	49.4	46.4	48.8
3.3	2.8	5.2	5.0	4.9	5.3	3.9	5.1	4.4	5.0	5.0
94.3	94.8	90.2	90.5	91.0	90.6	92.6	90.1	91.9	90.4	90.6
0.02	0.06	0.05	0.05	0.07	0.03	0.09	0.04	0.02	0.04	0.08
34.34	36.60	58.31	57.93	57.30	57.92	45.39	60.98	47.00	61.40	59.11
35.17	32.41	9.56	9.67	10.58	9.37	22.80	6.43	21.64	6.09	8.26
0.11	0.09	0.05	0.05	0.05	0.04	0.09	0.04	0.09	0.05	0.05
12.40	11.83	10.96	11.42	10.61	12.17	11.55	10.78	10.95	10.47	10.49
0.15	0.17	0.08	0.12	0.09	0.10	0.13	0.08	0.12	0.09	0.09
17.14	17.13	20.12	20.41	20.72	19.57	18.74	21.38	18.87	21.62	20.81
0.00	0.00	0.00	0.00	0.00	0.00	0.00	0.00	0.00	0.00	0.00
0.11	0.11	0.20	0.17	0.08	0.21	0.14	0.13	0.13	0.13	0.15
0.17	0.18	0.38	0.33	0.34	0.38	0.25	0.41	0.27	0.39	0.41
99.59	98.58	99.71	100.13	99.82	99.77	99.16	100.27	99.10	100.27	99.45
0.000	0.001	0.001	0.001	0.001	0.001	0.002	0.001	0.000	0.001	0.002
1.166	1.240	1.782	1.768	1.752	1.779	1.471	1.832	1.511	1.839	1.800
0.801	0.737	0.196	0.198	0.217	0.193	0.495	0.130	0.467	0.122	0.169
0.002	0.002	0.001	0.001	0.001	0.001	0.002	0.001	0.002	0.001	0.001
0.299	0.284	0.238	0.247	0.230	0.265	0.265	0.230	0.250	0.223	0.227
0.004	0.004	0.002	0.003	0.002	0.002	0.003	0.002	0.003	0.002	0.002
0.736	0.734	0.778	0.788	0.801	0.760	0.768	0.812	0.767	0.819	0.802
0.000	0.000	0.000	0.000	0.000	0.000	0.000	0.000	0.000	0.000	0.000
0.002	0.002	0.004	0.003	0.001	0.004	0.003	0.002	0.003	0.002	0.003
0.004	0.004	0.008	0.007	0.007	0.008	0.006	0.008	0.006	0.008	0.008
3.015	3.009	3.009	3.016	3.013	3.013	3.014	3.018	3.009	3.018	3.013
0.259	0.260	0.213	0.206	0.194	0.231	0.227	0.182	0.225	0.175	0.191
0.040	0.025	0.025	0.042	0.036	0.035	0.038	0.048	0.025	0.047	0.036
0.740	0.739	0.785	0.793	0.805	0.767	0.771	0.817	0.773	0.824	0.808
0.407	0.373	0.099	0.101	0.110	0.098	0.252	0.066	0.236	0.062	0.086
0.399	0.368	0.098	0.099	0.108	0.096	0.247	0.065	0.233	0.061	0.084
0.581	0.620	0.890	0.881	0.874	0.887	0.734	0.912	0.755	0.915	0.898
0.020	0.012	0.012	0.021	0.018	0.017	0.019	0.024	0.012	0.024	0.018
0.438	0.463	0.707	0.713	0.716	0.692	0.577	0.763	0.591	0.772	0.738
0.154	0.164	0.193	0.186	0.174	0.210	0.171	0.171	0.173	0.165	0.176
0.301	0.275	0.078	0.080	0.089	0.075	0.194	0.054	0.182	0.051	0.069
0.106	0.097	0.021	0.021	0.021	0.023	0.058	0.012	0.053	0.011	0.016
1.000	1.000	1.000	1.000	1.000	1.000	1.000	1.000	1.000	1.000	1.000
4.11	4.08	3.82	3.81	3.81	3.83	3.96	3.76	3.94	3.75	3.79

Mt. Avers - Bird Bluff	*Mt. Avers - Bird Bluff*	*Mt. Avers - Bird Bluff*	*Mt. Avers - Bird Bluff*	*Mt. Avers - Bird Bluff*	*Mt. Avers - Bird Bluff*	*Mt. Aldaz*	*Mt. Cumming*	*Mt. Cumming*
FDM-AVBB02	**FDM-AVBB04**	**FDM-AVBB05**	**FDM-AVBB06**	**FDM-AVBB07**	**FDM-AVBB08**	**AD6021-X02**	**KSP89-181-X01** low-Cr Spl	**KSP89-181-X01** hghi-Cr Spl
779	*822*	*814*	*940*	*805*	*832*	*1084*	*838*	*984*
40.42	40.16	40.29	40.45	40.37	40.78	40.45	40.70	40.70
9.54	10.21	9.59	10.84	10.24	9.71	9.92	10.24	10.24
0.14	0.14	0.13	0.15	0.13	0.13	0.05	0.16	0.16
49.28	48.58	49.08	47.84	48.51	48.79	48.66	48.40	48.40
0.42	0.43	0.40	0.39	0.40	0.41	0.37	0.29	0.29
0.07	0.072	0.072	0.053	0.075	0.054	0.04	0.05	0.05
99.88	99.60	99.56	99.72	99.73	99.87	99.49	99.84	99.84
0.993	0.993	0.994	1.000	0.997	1.002	0.998	1.002	1.002
0.20	0.211	0.198	0.224	0.211	0.199	0.205	0.211	0.211
0.00	0.003	0.003	0.003	0.003	0.003	0.001	0.003	0.003
1.81	1.791	1.804	1.764	1.785	1.787	1.790	1.776	1.776
0.01	0.008	0.008	0.008	0.008	0.008	0.007	0.006	0.006
0.002	0.002	0.002	0.001	0.002	0.001	0.001	0.001	0.001
3.008	3.009	3.008	3.001	3.005	3.000	3.003	2.999	2.999
90.2	89.4	90.1	88.7	89.4	90.0	89.7	89.4	89.4
54.34	53.77	53.98	53.45	54.33	54.15	54.41	- - -	- - -
0.10	0.11	0.12	0.11	0.09	0.12	0.12	- - -	- - -
4.75	5.09	4.95	5.04	4.28	4.88	4.78	- - -	- - -
0.40	0.27	0.32	0.33	0.29	0.38	0.35	- - -	- - -
6.43	6.84	6.43	7.23	6.91	6.46	6.12	- - -	- - -
0.14	0.16	0.15	0.17	0.15	0.13	0.13	- - -	- - -
33.25	32.72	32.96	32.37	32.98	33.14	32.96	- - -	- - -
0.53	0.50	0.48	0.57	0.45	0.45	0.74	- - -	- - -
0.05	0.03	0.04	0.05	0.03	0.03	0.10	- - -	- - -
100.00	99.48	99.44	99.31	99.53	99.73	99.71	- - -	- - -
1.880	1.873	1.878	1.870	1.892	1.878	1.886	- - -	- - -
0.003	0.003	0.003	0.003	0.002	0.003	0.003	- - -	- - -
0.194	0.209	0.203	0.208	0.176	0.200	0.195	- - -	- - -
0.011	0.008	0.009	0.009	0.008	0.010	0.010	- - -	- - -
0.186	0.199	0.187	0.212	0.201	0.187	0.177	- - -	- - -
0.004	0.005	0.005	0.005	0.004	0.004	0.004	- - -	- - -
1.715	1.699	1.709	1.689	1.712	1.713	1.703	- - -	- - -
0.020	0.018	0.018	0.021	0.017	0.017	0.027	- - -	- - -
0.004	0.002	0.003	0.003	0.002	0.002	0.007	- - -	- - -
4.017	4.017	4.014	4.020	4.015	4.015	4.012	- - -	- - -
1.0	1.0	0.9	1.1	0.9	0.9	1.4	- - -	- - -
89.3	88.6	89.3	87.9	88.7	89.4	89.3	- - -	- - -
9.7	10.4	9.8	11.0	10.4	9.8	9.3	- - -	- - -
90.2	89.5	90.1	88.9	89.5	90.1	90.6	- - -	- - -
52.02	51.77	51.42	51.82	51.74	51.69	52.44	- - -	- - -
0.56	0.52	0.63	0.55	0.58	0.56	0.51	- - -	- - -
7.42	8.08	8.07	7.84	7.72	8.03	6.89	- - -	- - -
0.86	0.60	0.72	0.74	0.78	0.82	0.73	- - -	- - -
2.21	2.44	2.36	2.79	2.58	2.31	2.81	- - -	- - -
0.08	0.09	0.07	0.08	0.08	0.09	0.08	- - -	- - -
14.51	14.25	14.20	14.42	14.16	14.42	15.78	- - -	- - -
21.37	20.84	20.91	19.70	20.75	20.79	18.92	- - -	- - -
1.86	1.98	1.92	2.04	2.03	2.00	1.64	- - -	- - -
100.87	100.56	100.30	99.98	100.43	100.71	99.81	- - -	- - -
1.866	1.861	1.854	1.871	1.865	1.856	1.890	- - -	- - -
0.015	0.014	0.017	0.015	0.016	0.015	0.014	- - -	- - -
0.314	0.342	0.343	0.334	0.328	0.340	0.293	- - -	- - -
0.024	0.017	0.021	0.021	0.022	0.023	0.021	- - -	- - -
0.066	0.073	0.071	0.084	0.078	0.069	0.085	- - -	- - -
0.002	0.003	0.002	0.002	0.003	0.003	0.003	- - -	- - -
0.776	0.764	0.763	0.776	0.761	0.772	0.847	- - -	- - -
0.821	0.803	0.808	0.762	0.801	0.800	0.731	- - -	- - -
0.129	0.138	0.134	0.143	0.142	0.139	0.114	- - -	- - -
4.014	4.014	4.014	4.008	4.015	4.017	3.997	- - -	- - -
49.4	49.0	49.2	47.0	48.9	48.7	43.9	- - -	- - -
46.6	46.6	46.5	47.8	46.4	47.0	51.0	- - -	- - -
4.0	4.5	4.3	5.2	4.7	4.2	5.1	- - -	- - -
92.1	91.2	91.5	90.2	90.7	91.8	90.9	- - -	- - -
0.03	0.03	0.03	0.04	0.05	0.03	0.13	0.4	0.44
58.37	61.38	59.35	59.76	58.13	59.43	57.92	23	16.87
9.25	6.03	8.17	7.68	8.90	8.08	9.26	36.17	42.92
0.04	0.04	0.07	0.05	0.05	0.04	0.05	0.21	0.22
10.53	10.51	10.43	11.53	11.21	10.40	9.87	25.74	24.22
0.10	0.09	0.10	0.11	0.11	0.10	0.03	0.24	0.28
20.15	20.50	20.36	19.82	19.87	20.34	21.87	12.12	12.32
0.00	0.00	0.00	0.00	0.00	0.00	0.00	0.00	0.00
0.18	0.14	0.18	0.16	0.14	0.16	0.09	0.22	0.06
0.41	0.48	0.37	0.38	0.39	0.43	0.39	0.18	0.14
99.04	99.20	99.06	99.54	98.86	99.01	99.61	98.28	97.47
0.001	0.001	0.001	0.001	0.001	0.001	0.002	0.010	0.011
1.791	1.859	1.813	1.822	1.791	1.816	1.763	0.871	0.659
0.190	0.122	0.167	0.157	0.184	0.166	0.189	0.919	1.125
0.001	0.001	0.001	0.001	0.001	0.001	0.001	0.005	0.006
0.229	0.226	0.226	0.250	0.245	0.225	0.213	0.692	0.671
0.002	0.002	0.002	0.002	0.002	0.002	0.001	0.007	0.008
0.782	0.785	0.787	0.765	0.775	0.786	0.842	0.580	0.609
0.000	0.000	0.000	0.000	0.000	0.000	0.000	0.000	0.000
0.003	0.003	0.003	0.003	0.003	0.003	0.002	0.005	0.001
0.009	0.010	0.008	0.008	0.008	0.009	0.008	0.005	0.004
3.008	3.008	3.008	3.009	3.011	3.008	3.021	3.093	3.094
0.207	0.204	0.203	0.226	0.217	0.203	0.157	0.444	0.420
0.022	0.022	0.023	0.024	0.029	0.022	0.056	0.248	0.251
0.791	0.794	0.795	0.772	0.781	0.795	0.843	0.567	0.592
0.096	0.062	0.085	0.079	0.093	0.084	0.097	0.513	0.631
0.095	0.061	0.084	0.078	0.092	0.083	0.094	0.451	0.553
0.894	0.928	0.905	0.910	0.894	0.906	0.878	0.427	0.324
0.011	0.011	0.011	0.012	0.014	0.011	0.028	0.122	0.123
0.715	0.745	0.727	0.711	0.709	0.728	0.761	0.276	0.219
0.189	0.193	0.188	0.210	0.198	0.188	0.142	0.211	0.151
0.076	0.049	0.067	0.061	0.073	0.066	0.082	0.291	0.373
0.020	0.013	0.017	0.018	0.020	0.017	0.015	0.222	0.258
1.000	1.000	1.000	1.000	1.000	1.000	1.000	1.000	1.000
3.81	3.78	3.80	3.81	3.81	3.79	3.77	4.33	4.40